Ore Geology Reviews 116 (2020) 103145

Contents lists available at ScienceDirect

Ore Geology Reviews

journal homepage: www.elsevier.com/locate/oregeorev

Trace metal distributions in sulfide scales of the seawater-dominated Reykjanes geothermal system: Constraints on sub-seafloor hydrothermal mineralizing processes and metal fluxes

Hannah L.J. Grant[a,*], Mark D. Hannington[a,b], Vigdís Hardardóttir[c], Sebastian H. Fuchs[a,1], Dirk Schumann[d]

[a] GEOMAR, Helmholtz Center for Ocean Research Kiel, Wischhofstrasse 1-3, D-24148 Kiel, Germany
[b] Department of Earth and Environmental Sciences, University of Ottawa, 25 Templeton St., Advanced Research Complex, Ottawa K1N 6N5, Canada
[c] Iceland GeoSurvey, Grensásvegur 9, Reykjavík 109, Iceland
[d] Fibics Incorporated, 1431 Merivale Road #100, Ottawa, ON K2E 0B9, Canada

ARTICLE INFO

Keywords:
Trace metals
Seafloor massive sulfides
Reykjanes geothermal system
Hydrothermal fluid
Boiling

ABSTRACT

Mineral precipitation in the seawater-dominated Reykjanes geothermal system on the Mid-Atlantic Ridge, Iceland is caused by abrupt, artificially induced, pressure and temperature changes as deep high-temperature liquids are drawn from reservoir rocks up through the geothermal wells. Sulfide scales within these wells represent a complete profile of mineral precipitation through a seafloor hydrothermal system, from the deep reservoir to the low-temperature silica-rich surface discharge. Mineral scales have formed under a range of conditions from high pressures and temperatures at depth (> 2 km) to boiling conditions in the upflow zone and at the surface. Consistent trace element enrichments, similar to those in black smoker chimneys, are documented: Cu, Zn, Cd, Co, Te, V, Ni, Mo, W, Sn, Fe and S are enriched at higher pressures and temperatures in the deepest scales, Zn and Cu, Bi, Pb, Ag, As, Sb, Ga, Hg, Tl, U, and Th are enriched at lower temperatures and pressures nearer to the surface. A number of elements (e.g., Co, Se, Cd, Zn, Cu, and Au) are deposited in both high- and low-pressure scales, but are hosted by distinctly different minerals. Other trace elements, such as Pb, Ag, and Ga, are strongly partitioned into low-temperature minerals, such as galena (Pb, Ag) and clays (Ga). Boiling and destabilization of metal-bearing aqueous complexes are the dominant control on the deposition of most metals (particularly Au). Other metals (e.g., Cu and Se) may also have been transported in the vapor phase. Very large enrichments of Au, Ag and Pb in the scales (e.g., 948 ppm Au, 23,200 ppm Ag, and 18.8 wt.% Pb) versus average concentrations in black smoker chimneys likely reflect that some elements are preferentially deposited in boiling systems. A mass accumulation of 5.7 t/yr of massive sulfide was calculated for one high-temperature production well, equating to metal fluxes of 1.7 t/yr Zn, 0.3 t/yr Cu, 23 kg/yr Pb, 4.1 kg/yr Ag, and 0.5 kg/yr Au. At least three quarters of the major and trace element load is precipitated within the well before reaching the surface. We suggest that a similar proportion of metals may be deposited below the seafloor in submarine hydrothermal systems where significant boiling has occurred. Mass accumulation estimations over the lifetime of the Reykjanes system may indicate significant enrichment of Zn, Pb, Au, and Ag relative to both modern and ancient mafic-dominated seafloor massive sulfide deposits, and highlights the potential for metal enrichment and accumulation in the deep parts of geothermal systems.

1. Introduction

Recent years have seen a rapid growth in demand for specific elements and metals that are commonly present in only trace quantities in mined ores and recovered only as by-products of other metals. Some of these metals are found in ancient volcanogenic massive sulfide (VMS) deposits that are mined mostly for Cu, Zn and Pb, and in similar modern seafloor massive sulfide (SMS) deposits that might be mined in the future (Petersen et al., 2016). However, the abundance, distribution, and economic potential of many trace and rare metals in submarine

* Corresponding author at: The British Geological Survey, The Lyell Centre, Research Avenue S, Edinburgh EH14 4AP, United Kingdom.
E-mail address: hgrant@bgs.ac.uk (H.L.J. Grant).
[1] Now at: Federal Institute for Geoscience and Natural Resources (BGR), Stilleweg 2, D-30655 Hannover, Germany.

https://doi.org/10.1016/j.oregeorev.2019.103145
Received 10 May 2019; Received in revised form 13 September 2019; Accepted 27 September 2019
Available online 28 September 2019

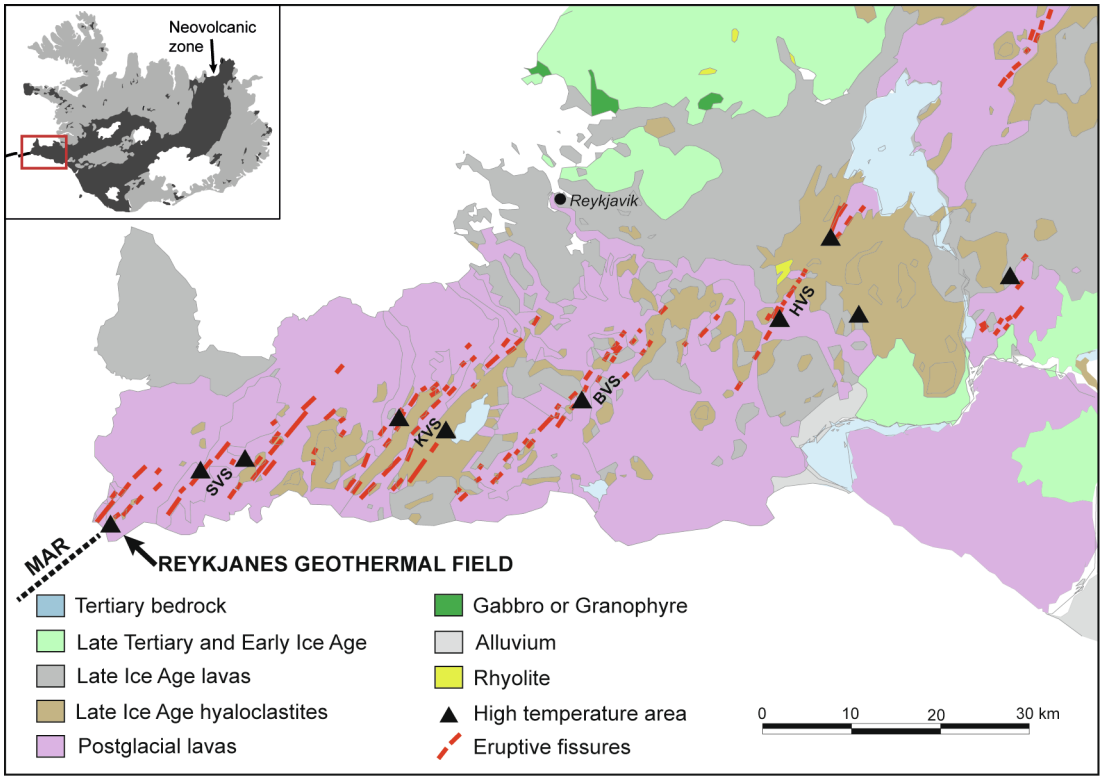

Fig. 1. Geological map of the Reykjanes Peninsula and Reykjanes geothermal field in the Icelandic neovolcanic zone (inset). Dotted black line to the southwest indicates approximate location of the sub-aerial Mid-Atlantic Ridge (MAR). Abbreviations of high-temperature geothermal fields: SVS = Svartsengi Volcanic System, KVS = Krisuvik Volcanic System, BVS = Brennisteinsfjöll Volcanic System, HVS = Hengill Volcanic System. Geological map modified after Hardardóttir et al. (2013) and Saemundsson and Jóhannesson (2004).

hydrothermal systems is poorly understood due to the inherent difficulties of directly sampling active, deep high-temperature upflow.

During convective hydrothermal circulation, reactions between heated seawater and volcanic rocks occur first at low temperatures as cold seawater is drawn into the oceanic crust in the down-flowing limb ('recharge' zone) of the hydrothermal convection cell, then at much higher temperatures in the deepest parts of the circulation system, reaching 400 °C in a high-temperature "reaction zone" at ~2 km depth (Mottl, 1983; Alt, 1995: Hannington et al., 2005; Hannington, 2014). Metals and reduced sulfur leached from the host rock reach maximum concentrations in the reaction zone where they become major constituents of end-member hydrothermal fluids. This superheated, metal-enriched fluid rises through vertically extensive fracture networks to be discharged at the seafloor. The compositions of the venting fluids have been extensively studied (e.g., Von Damm et al., 1985a, 1985b; Von Damm, 1990; Butterfield et al., 1994; Edmond et al., 1995; Edmonds et al., 1996; Gamo et al., 1996; Metz and Trefry, 2000; Douville et al., 1999; Gallant and Von Damm, 2006; Schmidt et al., 2007; Koschinsky et al., 2008; James et al., 2014), but little is known about the fate of metals in the deep sub-seafloor as the fluids escape the reaction zone and rise to the surface. Except in a few cases where the underlying stockwork zones have been drilled (e.g., TAG, Middle Valley, PACMANUS), subseafloor geochemical profiles of the altered and mineralized crust of actively-forming massive sulfide deposits have been difficult to study. As a result, a number of questions remain about the transfer of metals from the deeper parts of the hydrothermal system to the seafloor.

Numerous authors have attempted to reconstruct deep hydrothermal upflow zones from studies of alteration in ophiolite sections and in lower oceanic crust exposed by faults (e.g., MARK, ODP Hole 504B, ODP Hole 1256D, Pito Deep, Hess Deep: Parmentier and Spooner, 1978; Oudin and Constantinou, 1984; Alt et al., 1986; Francheteau et al., 1990; Gillis and Thompson, 1993; MacLeod et al., 1996; Gillis et al., 2001; Coogan et al., 2007; Heft et al., 2008; Alt et al., 2010; Adamies, 2010; Barker et al., 2010; Jowitt et al., 2012; Patten et al., 2016, 2017). However, the conditions under which the stockwork mineralization formed cannot always be clearly determined, especially in fossil hydrothermal systems.

Mineral scales from actively discharging geothermal systems offer the unique opportunity to relate details of mineral precipitation to the pressure and temperature conditions in the upflow zone, in some cases including actual samples of the mineralizing fluids (e.g., Hardardóttir et al., 2009, 2010; Simmons et al., 2016). In this study, we examine the trace metal distribution in high-temperature mineral scales from downhole pipes and surface pipes in the seawater-dominated, basalt-hosted Reykjanes geothermal system on Iceland. These scales represent a nearly complete profile of sub-seafloor mineralization from 2.7 km below surface to the silica-rich sinters deposited at low temperatures on the surface. Previous studies have focused on sulfide scaling in surface pipes (e.g., Hardardóttir et al., 2010) and, where drill cuttings have been sampled, on the mineralogy and geochemistry of the altered wall rocks (Marks et al., 2010, 2015; Seward et al., 2011; Seward, 2014; Fowler et al., 2015; Fowler and Zierenberg, 2016; Libbey and Williams-Jones, 2016a, 2016b, 2016c).

We present the first comprehensive analysis of mineral precipitates within actively discharging wells from the bottom to the top of the hydrothermal system at well-constrained pressures and temperatures. We examine the trace metals in scales precipitated from the deep, pre-boiled reservoir liquids at ~2 km depth and boiling hydrothermal fluids through the entire upflow zone and in the surface pipes to the point of discharge. These results provide a unique picture of the behavior of the metal load in fluids traversing the whole of the hydrothermal system.

2. The Reykjanes geothermal system

2.1. Geology

The Reykjanes Peninsula is located on the southwestern tip of Iceland and is the subaerial continuation of the offshore slow-spreading Reykjanes Ridge (~1.8 cm/yr; Fridleifsson et al., 2011). The exposed basement volcanic rocks are younger than 700 ka and a significant proportion of the peninsula is covered by post-glacial Holocene (< 13 ka), highly permeable, mafic shield or fissure-fed lavas (Peate et al., 2009). The young lavas were erupted from five en-echelon NE-SW trending volcanic systems (Fig. 1), from west to east: Reykjanes, Svartsengi, Krisuvik, Brennisteinsfjöll, and Hengill, along a 65 km segment of the peninsula (Jakobsson et al., 1978). The last phase of volcanism on the peninsula, between c. 940 and c. 1340 AD, consisted of basaltic fissure-fed flows. Magmatic activity is now concentrated in submerged ridge segments offshore (Peate et al., 2009).

The Reykjanes geothermal system is hosted within the young and highly permeable basaltic formations. Evidence from the chronology of recent eruptions in the area, which cover altered volcanic units, indicates that the geothermal system has been active at least since the last glacial maximum, 18,000–20,000 yr ago (Hardardóttir, 2011). The lowest stratigraphic units below 1 km are pillow basalts considered to have erupted in deep water (Franzson et al., 2002; Fridleifsson et al., 2011). Successive units are stacked to shallower depths where the eruptive style changed to a more explosive mode. The upper 1 km is dominated by subaerial to marine Pleistocene hyaloclastite, breccia, dense phreatic tuffs and marine sediments acting as a semi-impermeable cap on the hydrologic system (Fridleifsson et al., 2011). Reworked sediments containing shallow water fossils indicate a coastal environment, and the most recent formations include sub-glacial hyaloclastite and subaerial lavas. The stratigraphic succession is intruded by dykes, which increase in abundance at depth (Sigurdsson, 2010). A low resistivity anomaly 10 km below the surface expression of the geothermal system has been interpreted as either a dense sheeted- dyke complex or a large cooling gabbroic intrusion, and likely represents the heat engine of the shallower hydrothermal system (Fridleifsson et al., 2011). Frequent, but generally small earthquakes maintain good permeability for hydrothermal upflow (Fridleifsson et al., 2011). The primary high-temperature upflow exploited by wells RN-10, RN-12, RN-21, RN-27 is controlled by the intersection of a NE-SW trending zone of normal faults and eruptive fissures, N-S trending fractures, and a NW-SE transform fault (Fig. 2) (Franzson et al., 2002). The surface thermal manifestation covers ~1 km^2, but a low resistivity zone at 800 m depth has an area of 11 km^2 and likely represents the full areal extent of the hydrothermal upflow (Sigurdsson, 2010).

2.2. Geothermal reservoir

The Reykjanes geothermal system is the only seawater-dominated, basalt-hosted geothermal energy production site in the world. Thirty-seven geothermal wells have been drilled into the field to a maximum depth of 3028 m (Oskarsson et al., 2015), drawing on a high-temperature reservoir fluid of modified seawater (Arnorsson, 1978; Sveinbjornsdottir et al., 1986), which is directly analogous to vent fluid in modern black smoker systems (Hardardóttir et al., 2009). The surface infrastructure lies less than 40 m above sea level and is surrounded by the Atlantic Ocean on three sides (Fig. 2). Based on liquids sampled at the surface and corrected for vapor loss, and the compositions of deep liquid sampled downhole (Hardardóttir et al., 2009; Hannington et al., 2016), a fluid of essentially constant composition is considered to be feeding all of the wells at Reykjanes. The chloride concentration (~3.2 wt.%) is essentially that of seawater (Hardardóttir et al., 2009); other dissolved components such as K^+, Ca^{2+}, SiO_2, CO_2 and H_2S are enriched due to the reaction of heated seawater with the surrounding basalt (Arnorsson, 1978). SO_4^{2-} and Mg are depleted relative to seawater. A pH (at 25 °C) of ~5.3 was calculated for the Reykjanes reservoir fluid by Hannington et al. (2016; see Supp. Info.), and is a unit or more higher compared to typical black smoker MOR vent fluids with a pH at 25 °C of 3–4. Kadko et al. (2007) estimated that the crustal residence time of circulating hydrothermal fluids sampled from well RN-12 is less than 5 years, comparable to hydrothermal fluid residence times obtained from submarine hydrothermal systems (e.g., Kadko and Butterfield, 1998). Surface meteoric waters locally penetrate the upper 30 m of the hydrothermal upflow. However, $^{87}Sr/^{86}Sr$ values shift significantly towards seawater values with increasing depth, confirming deep penetration of seawater into the Reykjanes system (Marks et al., 2010). There is no strong evidence for direct magmatic input in the hydrothermal fluids (Sveinbjornsdottir et al., 1986; Pope et al., 2009). Sulfur isotope values of sulfide mineral scales in surface pipes range from 2.3‰ to 4.2‰, similar to black smoker sulfide deposits (Springsklee, 2016).

At the time of sampling in this study, the reservoir fluid was boiling in every well from the surface to maximum depths of ~1400 m, below which the system is liquid-dominated (one-phase) to a minimum depth of 2.5 km. The highest temperature directly recorded during production is 320 °C in the 2054 m deep well RN-10 (Franzson et al., 2002). At this temperature, the depth level of first boiling for seawater is ~1400 m depth below the water table (Arnorsson et al., 2007). In the RN-10 upflow zone, fluid below about 1400 m depth will be liquid only, above this depth it will be two-phase (Pope et al., 2009). In the two-phase zone, temperatures are determined by hydrostatic head and follow the boiling curve (e.g. Franzson et al., 2002). The temperature at well depths of 1–2.5 km is between 280° and 300 °C; however, temperatures up to 350 °C have been recorded in the inclined wells RN-17B and RN-30 at depths of 3077 m and 2869 m (Fridleifsson et al., 2011; Sigurdsson, 2012; Fridriksson et al., 2015). Inflow feed zones (aquifers) occur at various depths from 800 to 1200 m and 1900 to 2300 m, the latter below the boiling zone (Sigurdsson, 2010). Since the introduction of a 100 MW_e power plant in 2007, intense drawdown of fluid has resulted in reservoir pressures dropping by as much as 40 bars, and depth of boiling for some wells (e.g., RN-12, 19, and 21) has deepened (Hannington et al., 2016). A steam cap is also forming in the central part of the field (Sigurdsson, 2010).

Drill cuttings of altered rocks from the wells show a zoned hydrothermal system at depth (Marks et al., 2010, 2015; Libbey and Williams-Jones, 2016a–2016c). Temperatures < 200 °C are indicated by smectite-zeolite facies alteration down to 500 m depth; temperatures > 200–250 °C are indicated by epidote-zeolite facies alteration to ~1.2 km. Below 1.2 km, epidote-actinolite is dominant, indicating temperatures of 250–350 °C, and below ~2.4–3.0 km amphibolite facies alteration indicates temperatures of > 350 °C (Franzson et al., 2002; Marks et al., 2010). However, at very shallow depths, high-temperature alteration phases are not consistent with current temperatures and are interpreted to reflect a higher pressure and temperatures during Pleistocene glaciation (Marks et al., 2010, 2015). The extent and mineralogy of the alteration generally have many similarities to alteration beneath actively-forming SMS deposits (e.g., Fowler et al., 2015).

2.3. Production

Producing wells supply a two-phase fluid directly to the separator station, which has two steam separators, and then to two 50 MW_e turbines in the power station (Fig. 3). Wells are classified according to the pressure of fluids emerging at the wellhead, which generally reflects proximity to the primary upflow (Table 1), where one bar is equal to 0.1 megapascals. High-pressure wells have wellhead fluid pressures of between 32 and 50 bar, medium-pressure wells between 28 and 32 bar, and low-pressure wells 25–28 bar.

The two-phase fluid that emerges at the surface wellhead (Fig. 4) continues to boil in the surface pipes and as it passes through several control points (an orifice plate, OP, and fluid flow control valve, FFCV).

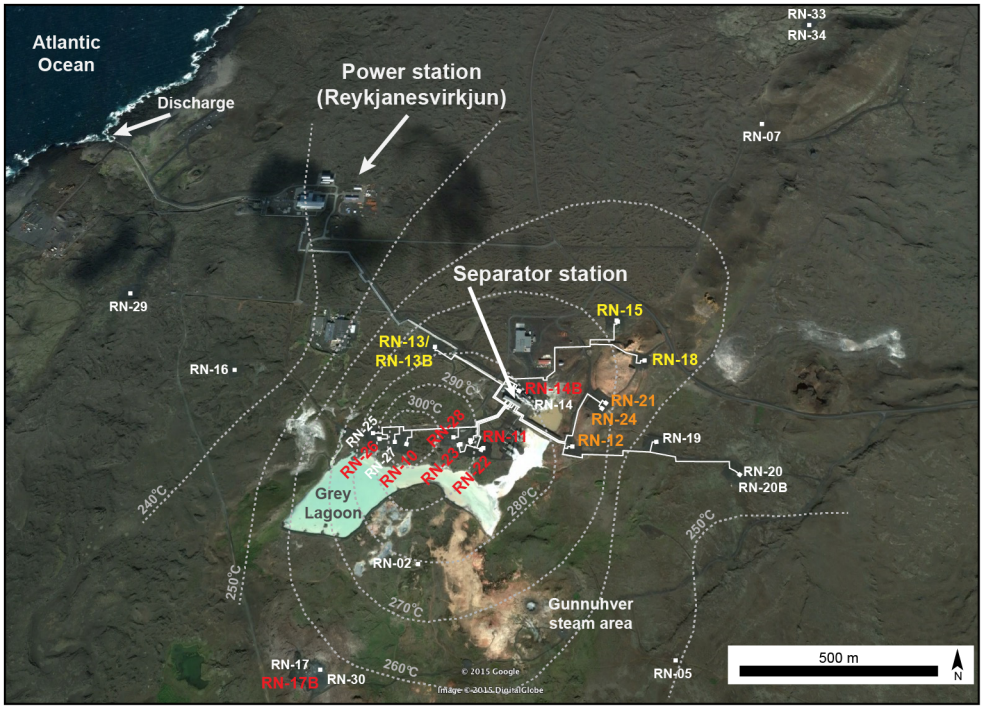

Fig. 2. The Reykjanes geothermal field, Reykjanes Peninsula, Iceland. High-pressure sampled wells are denoted in red, medium-pressure in orange, and low-pressure wells in yellow. White lines show current pipelines; white well numbers were not sampled in this project. Dashed grey lines show approximate isotherms of wells at 2.2 km depth (modified from Marks et al., 2015). Base map from Google Earth (2015). (For interpretation of the references to color in this figure legend, the reader is referred to the web version of this article.)

These control points are hereafter referred to as the OP and FFCV. The OP and FFCV serve as throttle points for well management, to maintain two-phase flow to the separator station at a constant pressure of ~22 bar, and also to help minimize silica supersaturation and precipitation in the surface pipes (Hardardóttir et al., 2010). Abrupt changes in pressure (and temperature) occur at the OP and FFCV, and so significant scaling can occur at these locations. A small amount of brine from the separator station is either sent to the venthouse to control separator pressure or discharged into the Grey Lagoon and, once cooled, released into the ocean. The steam phase, which is sent to the power station, and then out to a condenser and cooling tower, is mixed with brine and re-injected in distal recharge wells to partially mitigate the drawdown of liquid from the system (Sigurdsson, 2010).

The deepest exploration well drilled to date is RN-17 where the bottom hole temperature at 3082 m depth is between 320° and 380 °C (Marks et al., 2015). In 2017, the Iceland Deep Drilling Project (IDDP-2) utilized the existing Reykjanes well RN-15 to drill to 4659 m depth. The project aimed to find supercritical fluids below the current production zone of the Reykjanes geothermal field. IDDP-2 successfully measured temperatures of 426 °C and fluid pressures of 340 bars (34 Mpa) corresponding to supercritical conditions within permeable layers at the bottom of the well (Fridleifsson et al., 2017).

2.4. Scaling in the Reykjanes system

As the reservoir liquid is drawn up well pipes for extraction, artificially induced pressure and temperature changes cause boiling and precipitation of sulfides directly from the fluid as millimeter (mm) to centimeter (cm) thick scales in both downhole and surface pipes. Previous work at Reykjanes has shown that the mineralogy of the scales is directly comparable to black smokers at active seafloor hydrothermal vents but with spectacular enrichment of some elements, such as gold (Hardardóttir et al., 2009, 2010, 2013; Hannington et al., 2016). As noted above, the geometry and the conditions of the deep reservoir zone are well known from downhole measurements and from studies of the host rocks and alteration, but a complete study of the mineral scales, including in the deep subsurface, has never been carried out.

Sulfide and silica-rich deposits in the geothermal wells are especially abundant where large pressure changes occur (e.g., throttling of fluids at control points) and can severely limit the fluid flow and energy

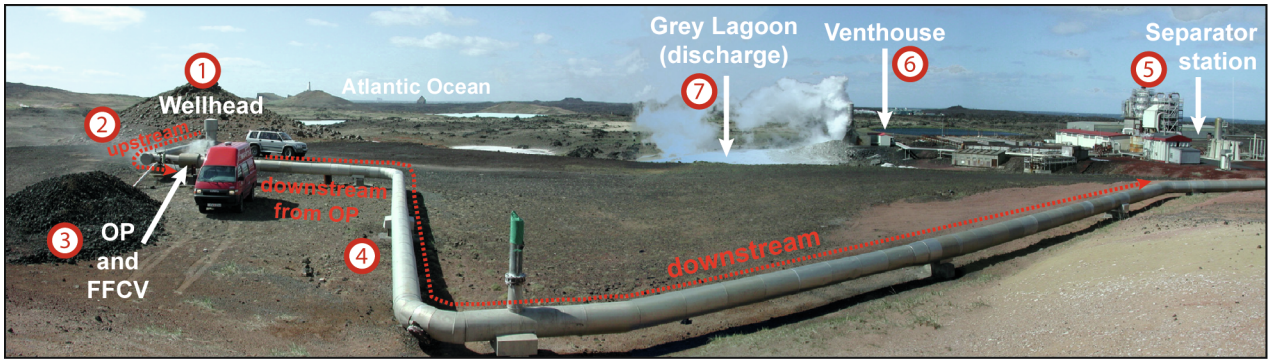

Fig. 3. Panorama of the Reykjanes geothermal site showing locations of surface sampling: 1) Surface wellhead, 2) upstream of wellhead, 3) first orifice plate and fluid control valve (OP and FFCV), 4) downstream of OP and FFCV, 5) separator station, 6) venthouse, and 7) Grey Lagoon discharge pond. Image used with permission of V. Hardardóttir.

Table 1
Physical parameters for sampled wells from the Reykjanes geothermal field.

Well	Year drilled	Max. T (°C)	Depth (m)	Reservoir T (°C) (2006–2007)	Avg. P (bar) at wellhead (2006)	T decrease from wellhead high to downstream OP1 (°C)
High-pressure						
RN-10	1999	319	1900	310	25	226–220
RN-11	2002	296	2172	295	42	255–220
RN-14B	2007	290	2426	300	40	252–220
RN-17B	2008	345	3082	na	na	na
RN-22	2006	305	1105	300/290	35	244–220
RN-23	2006	314	1847	300	45	259–220
RN-26	2007	na	1503	na	na	na
RN-28	2008	na	1119	na	na	na
Medium-pressure						
RN-12	2002	314	2495	295	37	247–220
RN-21	2005	285	1593	285	32	239–220
RN-24	2006	286	1269	280	30	236–220
Low-pressure						
RN-13	2004	295	2475	295	22	na
RN-13B	2007	295	2530	295	na	na
RN-15	2004	284	2154	284	22	226–220
RN-18	2004	292	1386	285	22	220–220
RN-19	2005	302	2226	275	22	230–220

Summary of the physical characteristics of sampled wells in the Reykjanes geothermal field (Fig. 2 for well locations). Where temperature (T) or pressure (P) parameters are not available (e.g. data not reported or a non-producing or collapsed well, this is indicated by 'na'. Data are from Hardardóttir et al. (2009), Hardardóttir et al. (2010), Sigurdsson (2012), and Libbey and Williams-Jones (2016b).

production (Hardardóttir et al., 2010). Artificially-induced pressure changes, including 'flashing', during well management cause sulfides to precipitate on the inside of downhole pipes throughout the entire system. Exsolution of gases during boiling (especially H_2S, H_2, and CO_2) destabilizes metal complexes and promotes sulfide deposition, removing a large proportion of the metal load in the hydrothermal fluid (Drummond and Ohmoto, 1985). Even in deep wells that extend far below the bottom of the boiling zone, minor sulfide scaling is also present near the bottoms of the wells (e.g., RN-10 in Fig. 4).

Mineral precipitation in the deep wells in the Reykjanes geothermal system is thought to be similar to that in the upflow zones and stockworks of boiling seafloor hydrothermal systems, with the two-phase, boiled fluid emerging at the wellhead being depleted in metals due to sub-surface precipitation. The sub-surface scaling is analogous to stockwork mineralization; scaling in the surface pipes through to low-temperature discharge in the Grey Lagoon represents lower-temperature deposition similar to what may occur near the seafloor. Unboiled reservoir liquids in the Reykjanes system correspond to the deep high-temperature fluids in seafloor hydrothermal systems (e.g., Hardardóttir et al., 2009; Hannington et al., 2016).

Mineral scales in shallow downhole pipes and in upstream surface pipes before the first orifice plate (OP) most closely resemble the mineral assemblages in high-temperature sulfide chimneys of seafloor hydrothermal systems (Hardardóttir et al., 2010). Between the wellhead and the first orifice plate ('upstream' from the FFCV: Fig. 5a), the two-phase fluid pressure is always above ~22 bar, which maintains high-temperatures in the surface pipes (e.g., from 220° to 259 °C: Table 1). Precipitation of high-temperature sulfides (i.e., Cu- and Cu-Fe-sulfides) occurs on the walls of the upstream pipes (Fig. 5a) and on the 'upstream' side of the orifice plate (Fig. 5b). Precipitation of Cu- and Cu-Fe-sulfides also occurs directly on the FFCV (Fig. 5c). Downstream from the FFCV, towards the separator station (Fig. 5d), sulfide precipitates are similar to lower-temperature seafloor massive sulfides (i.e., dominated by Pb- and Zn-sulfides). Closer to the separator station, scales are mainly amorphous silica with minor or trace sulfides. By the time the two-phase fluid reaches the separation station, virtually all metal has been deposited, and the solids precipitated from the brine released to the Grey Lagoon consist mostly of silica (Sternbergh, 2016). These precipitates are analogous to low-temperature silica-rich deposits formed by diffuse hydrothermal venting in active seafloor hydrothermal systems (e.g., Herzig et al., 1988).

The scaling in the surface pipes has been extensively studied by Hardardóttir (2011). In this paper, we focus on the downhole scales and especially the behavior of the trace metals from the top to the bottom of the geothermal system.

3. Methods

3.1. Sample collection

Mineral scales examined in this study were collected by V. Hardardóttir (Icelandic GeoSurvey, ISOR) during periodic well maintenance over an eleven-year period between 2003 and 2014 in cooperation with HS Orka HF, which operates the geothermal installation. Samples were collected from surface pipelines and the power station (Reykjanesvirkjun) when the pipes were opened for cleaning and during turbine maintenance breaks. Scales inside the pipes could be accessed and the orifice plates and fluid flow control values could be removed. A total of 87 samples were collected between the different wellheads and the Grey Lagoon. Scales were photographed and described before removal, with the flow direction noted (Table 2).

Downhole scales were collected during periodic well workovers, either by rotary cleaning (e.g., RN-10) or by removal of the downhole liner following quenching of the well (e.g., RN-22). In 2009, nine samples were collected from well RN-22 between 141 and 669 m depth during an attempt to remove sulfide scales from the casing and liner. In 2013, well RN-22 was quenched by injecting cold water, and the complete liner removed from the well. This provided a unique opportunity to sample scales from the liner to a depth of more than 1.6 km. The majority of scales, however, became dislodged during liner removal and fell to the bottom of the well. However, 8 samples were taken from scales still fixed to the liner wall from 1051 m to 1088 m and 1636 m to 1646 m (Hardardóttir, 2014). In 2014, 24 samples were collected between surface and 1832 m depth from well RN-10 during reaming of the well while in discharge (hot well). This required a special gland to seal around the drill pipes and divert the flow from the rig. A tricone drill bit removed the scaling from the interior of the pipes, and scales were transported to surface by two phase flow (steam and water) as fragmented chips. Scale cuttings in the fluids were collected at specified intervals using a wire sieve at surface. The depths from which the scales were dislodged and transported to the surface were recorded based on the depth of the drill bit. In 2011, a stainless steel apparatus for a fluid inclusion study was suspended by a wireline at 2700 m depth in well RN-17B for three weeks at reservoir conditions of ~170 bar and 330 °C (Seward et al., 2011; Hardardóttir et al., 2013). Sulfides that precipitated in holes in the outer housing of the apparatus were collected for analysis when it was returned to the surface (Hardardóttir, 2014).

3.2. Bulk geochemical analyses

Eighty samples of sulfide-bearing scales from representative locations throughout the Reykjanes geothermal system were prepared for bulk geochemical analysis. To check for steel fragments from the well liner, a strong magnet was passed through samples to remove the magnetic component. This was examined under a binocular microscope and any remnant steel liner fragments removed before returning the magnetic mineral component back to the bulk sample. No bulk jaw mill crushing was required. Samples were pulverized in a 250-ml capacity agate mill with 5 x10 mm agate balls (Fritsch Pulverisette 5). Each

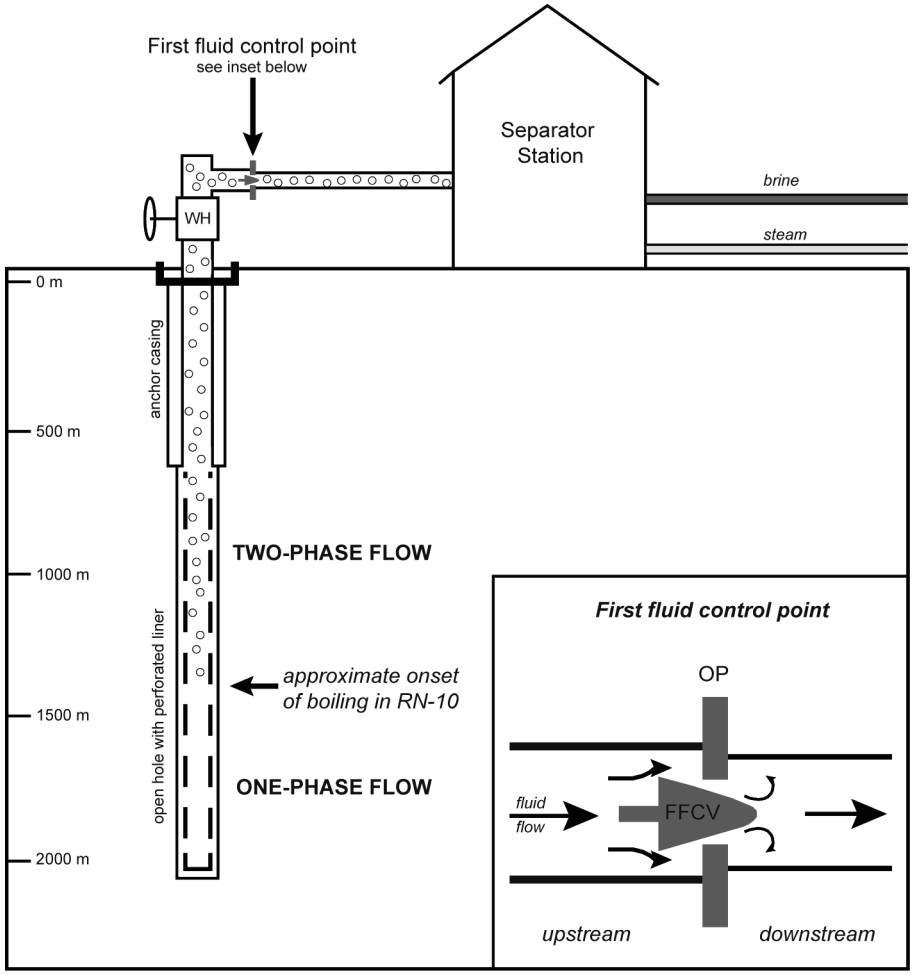

Fig. 4. Schematic model (not to scale) of well RN-10 in the Reykjanes geothermal system showing the well infrastructure and approximate location of initial boiling of rising seawater-dominated liquid (modified from Hardardóttir et al., 2010). Above the boiling level, fluid flow consists of vapor and liquid. The inset shows the first surface control point after the wellhead (i.e., Fig. 3), which consists of the cone-shaped fluid flow control valve (FFCV) and the orifice plate (OP). The upstream and downstream locations and the direction of fluid flow are indicated (arrows).

sample (15–25 g) was pulverized in 5-minute cycles, repeated as necessary up to 5 cycles to achieve a fineness of less than approximately 105 μm (150 mesh). Between samples the mill was cleaned with quartz sand (0.1–0.3 mm coarseness) in at least three 5-minute cycles each.

Samples were analyzed for major elements by ICP-OES (Al, Ca, Fe, K, Mg, Na, Si, Ti, S) following a sodium peroxide fusion and total acid digestion at Activation Laboratories, Ancaster, Canada. Trace elements were analyzed by a combination of instrumental neutron activation analysis (INAA: As, Au, Br, Cr, Hf, Hg, Ir, Lu, Sb, Sc, Se) and by ICP-MS following sodium peroxide fusion and total digestion (B, Ba, Be, Bi, Cd, Ce, Co, Cs, Cu, Dy, Er, Eu, Ga, Gd, Ge, Hf, Ho, In, La, Li, Mn, Mo, Nb, Nd, Ni, Pb, Pr, Rb, Sm, Sn, Sr, Ta, Tb, Te, Th, Tl, Tm, U, V, W, Y, Yb, and Zn). Where samples contained high Cu (> 1 wt.%), Zn (> 1 wt.%), Pb (> 0.5 wt.%), Cd (> 0.5 wt.%), or Au (> 3 ppm), re-analysis was performed using a four-acid total digestion ICP-OES assay technique (Cu, Zn, Pb, Cd), and gravimetric fire assay (Au). Fluorine was determined in a subset of samples by an ion-selective electrode technique (ISE). The accuracy and precision of the bulk analyses were monitored by repeat analysis of the CCRMP certified reference material CZN-4 (n = 3) and duplicates (n = 10) inserted evenly throughout the batch.

The chemical data are summarized in Tables 3 and 4 and the complete data set is reported in Table A1. Data for an additional 35 surface scales, 5 samples from the Grey Lagoon and separator station, and 8 shallow downhole samples previously analyzed by ISOR (Hardardóttir et al., 2010; Hardardóttir, 2011, 2014) are also included. Data for the deep sulfide scales in RN-17B are from Hardardóttir et al. (2013).

3.3. Electron microprobe analysis

Polished thin sections of all scales were prepared for transmitted and reflected light microscopy and mineral analysis (summary in Table 5). The downhole samples from RN-10 consist of small chips, which were prepared as grain mounts embedded in epoxy and polished for reflected light microscopy.

Discrete mineral phases in the sampled scales were analyzed for Fe, Cu, Zn, Pb, Au, Ag, and S on a JEOL-8200 Superprobe equipped with five wavelength-dispersive spectrometers and one energy-dispersive detector at the GEOMAR Helmholtz Center for Ocean Research Kiel in Germany. Copper, Fe, and S were calibrated using a natural chalcopyrite standard, Zn by a synthetic sphalerite standard, Pb by a galena standard, and Au and Ag by an Au_{60}-Ag_{40} alloy. Magnetite (n = 8) was analyzed for Ti, Fe, Al, Cr, Si, Ni, Mg, Mn using an ilmenite standard for Ti, Fe, and Mn, a chromite standard for Al, Cr, and Mg, an anorthite standard for Si, and a synthetic NiO standard for Ni. Operating conditions were 15 kV accelerating voltage and 50nA current with a 50 s count time. The full data sets are presented in Table B1 (sulfides and Au-bearing phases) and Table C1 (non-sulfides).

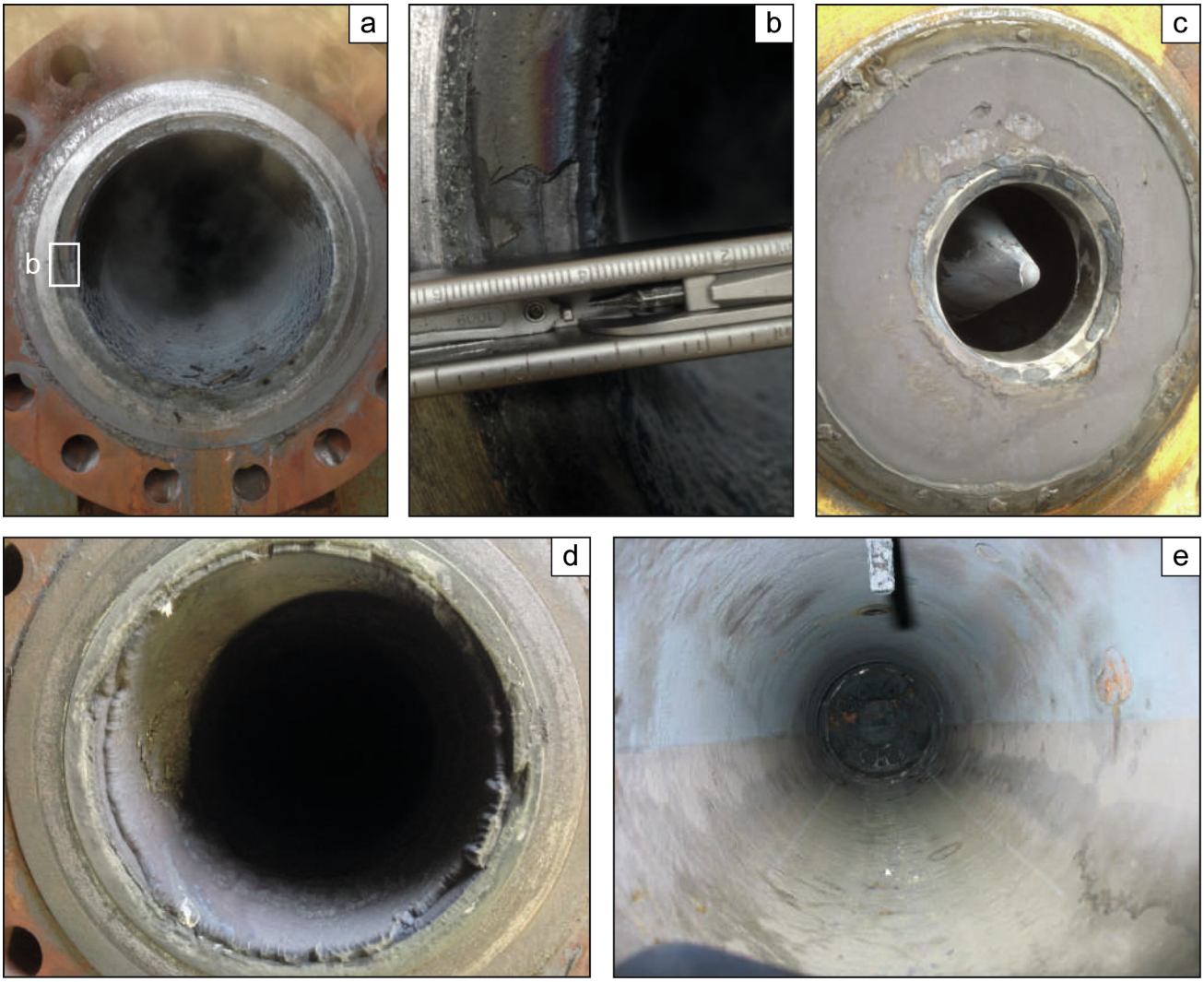

Fig. 5. Photographs of scales in surface geothermal well pipes. A) Looking upstream in high-pressure well RN-11 during the 2015 maintenance break. Blue Cu-(Fe)-sulfide scales < 0.5 cm in thickness are predominant in the base of the pipe. The white square indicates a close up in Fig. 5b. B) Close-up image of scale on the upstream side of the OP in high-pressure well RN-11 2015. The scale thickness is ~0.5 cm. C) Scales on the downstream side of the OP and FFCV in low-pressure well RN-13B during the 2015 maintenance break. Grey scales on the OP are dominantly sphalerite scales, and scales on the FFCV have a slight blue tint indicating more Cu-(Fe)-sulfides than on the OP. The scale thickness is < 0.5 cm. D) Looking downstream in high-pressure well RN-14 during the 2015 maintenance break. Blue Cu-(Fe)-sulfides are dominant. The scale thickness at the base of the pipe is approximately 2 cm. E) Looking upstream from the orifice plate towards the wellhead in high-pressure well RN-22 during the 2007 maintenance break. There is a thin coat of blue (Cu-Fe-sulfide) lining the pipe where steam would have been dominant, and gray where liquid was dominant (image from Hardardóttir, 2014). The scale thickness is < 0.1 cm. Images used with permission from V. Hardardóttir. (For interpretation of the references to color in this figure legend, the reader is referred to the web version of this article.)

3.4. X-Ray diffraction

X-ray diffraction (XRD) analysis was carried out on whole-rock powders of all downhole samples from RN-10 using a Philips X-Ray PW 1710 diffractomer and goniometer, equipped with a Co-tube and an automatic divergence slit and monochromator at GEOMAR Helmholtz Center for Ocean Research Kiel, Germany. Operating conditions were 40 kV and 35 mA, a 2-theta scanning angle of 4° to 75°, and a scan rate of 1 s per 0.02° step. The software package MacDiff (version 4.2.6) was used to manually identify mineral phases.

3.5. High-resolution scanning electron microscopy (HR-SEM)

High-resolution field-emission SEM imaging at Fibics Incorporated in Ottawa, Canada, was performed on downhole samples from well RN-10: two samples from the boiling zone at 1098 m and 1099 m, and one from below the boiling zone at 1832 m depth. The instrument used was a Zeiss Sigma HD variable-pressure field-emission scanning-electron microscope (SEM), which was operated with an accelerating voltage of 15 kV, a beam current of 7nA (120 mm aperture), and a working distance of 10 mm. Images were taken using the backscattered electron (BSE) detector.

4. Results

Downhole and surface scales were sampled from five different zones, each with well-defined conditions: I) below the boiling zone in wells RN-10, RN-22, and RN-17B (i.e., below ~1400 m in well RN-10, from 1636 m to 1646 m in RN-22, and at 2700 m in RN-17B); II) within the deep part of the boiling zone, from 1504 m to 1085 m in RN-10 and 1064 to 1088 m in RN-22; III) in the central part of the boiling zone from 904 m to the wellhead in RN-10, from 669 m to 141 m in RN-22, and then from the wellhead to the first orifice plate where pressure drops to ~22 bar in each of RN-10, 11, 12, 13B, 14, 14B, 15, 22, 23, 26, and 28; IV) in the surface boiling zone from the first OP and FFCV to ~40 m downstream in each of RN-10, 11, 12, 13, 13B, 14, 14B, 15, 18,

Table 2
Petrographic overview of representative scale samples.

Well	Sample ID	Location	Mineralogy																	
			ZnS	cpy	py	bn	dg	cv	gn	po	el	Ag	Ss	mt	amSi	rt	Feox	icbˆ	n.Auˆ	n.Agˆ	hmˆ	goˆ
Group I: below boiling zone																						
RN-17B	17RN-2011-2700	−2700 m DH	+	+	+				++	++					tr							
RN-10	RN10-2014-1832	−1832 m DH	++	++	tr	+		tr							++		tr		p?			
RN-10	RN10-2014-1828	−1828 m DH	++	++	tr	+		tr						tr	++		tr					
RN-10	RN10-2014-1800	−1800 m DH	+++	+++	tr	+	+	tr							++		tr					
RN-10	RN10-2014-1792A	−1792 m DH	++	+++	tr	+		tr							+++		tr					
RN-10	RN10-2014-1737	−1737 m DH	+++	+++	tr	+		tr						tr	++		tr					
RN-10	RN10-2014-1680	−1680 m DH	++	++	+									tr	++		+		p?			
RN-10	RN10-2014-1668	−1668 m DH	+++	++	r	+		tr						tr	++		+					
RN-22	RN22-2013-1646	−1646 m DH	++	+	tr									+			tr					
RN-22	RN22-2013-1642	−1642 m DH	++	+	tr									tr								
RN-22	RN22-2013-1638A	−1638 m DH	+	+	tr									tr								
RN-22	RN22-2013-1636	−1636 m DH	++	+	tr						tr			tr							p	p
RN-10	RN10-2014-1575	−1575 m DH	+++	++	tr	tr		r						tr	++		+					
Group II: deep boiling zone																						
RN-10	RN10-2014-1504	−1504 m DH	+++	++	+	+		r			1			+	++	tr	++					
RN-10	RN10-2014-1245	−1245 m DH	+++	++	++	+	+	tr			3			+	++	tr	+++					
RN-10	RN10-2014-1198	−1198 m DH	++	++	+	++	tr	+			2			ns	+++		+++					
RN-10	RN10-2014-1168	−1168 m DH	+++	+++	r	++		tr			3			++	+++	tr	++					
RN-10	RN10-2014-1148	−1148 m DH	+++	+++	tr	+	tr	tr			4			+++	+++	tr	+++					
RN-10	RN10-2014-1136	−1136 m DH	+++	+++	tr	++	+	+			3			++	+++	tr	++		p?			
RN-10	RN10-2014-1120	−1120 m DH	+++	++	tr	+	++	r			4			+++	+++	+	++					
RN-10	RN10-2014-1099	−1099 m DH	+++	+++	++	++	tr	tr			5			++	+++	tr	+++	p				
RN-10	RN10-2014-1098A	−1098 m DH	+++	+++	+	++	+	+			5			++	++	tr	+					
RN-10	RN10-2014-1097A	−1097 m DH	++	+++	+	+	+	tr			5			++	++	tr	++		p			
RN-10	RN10-2014-1095A	−1095 m DH	+++	+++	tr	++	+	tr			3			++	+++	tr	++					
RN-10	RN10-2014-1085	−1085 m DH	+++	++	r	+	tr	tr			3			+	++	tr	+	p	p			
RN-22	RN22-2013-1088	−1088 m DH	+		+																	
RN-22	RN22-2013-1064A	−1064 m DH	+		++																	
RN-22	RN22-2013-1051	−1051 m DH	++	tr	+																	
Group III: central boiling zone																						
RN-10	RN10-2014-904	−904 m DH	+++	++	tr	+	+	tr			3			+	++	tr						
RN-10	RN10-2014-870	−870 m DH	+++	++	tr	+	+	tr			3			+	++	tr	+		p			
RN-10	RN10-2014-835	−835 m DH	++	++		+		tr			1			tr	+++		+		p			
RN-22	22RN669	−669 m DH	+++	++						tr	1	r		tr	+							
RN-10	RN10-2014-660	−660 m DH	+++	++	+	+	+	tr			4			++	++	tr	+					
RN-22	22RN618	−618 m DH	++	+	tr					tr	r	+			+							
RN-22	22RN570	−570 m DH	+++	+								r			tr							
RN-22	22RN449	−449 m DH	+++	+	tr	tr						tr			tr							
RN-22	22RN350Fe*	−350 m DH	++	+		+								tr	+							
RN-22	22RN270Fe*	−270 m DH	++	++	tr	++	r?	tr			r	tr		tr	+							
RN-22	22RN160Fe*	−160 m DH	++	+	+	+		tr			2	tr		++	+							

(*continued on next page*)

Table 2 (*continued*)

Well	Sample ID	Location	Mineralogy																	
			ZnS	cpy	py	bn	dg	cv	gn	po	el	Ag	Ss	mt	amSi	rt	Feox	icb^	n.Au^	n.Ag^	hm^	go^
RN-22	22RN150	−150 m DH	+ +	+ +	tr	+	tr	tr			1	tr		+	+		tr					p
RN-22	22RN141	−141 m DH	+ + +	+ +	tr	+	tr			tr[2]	1	tr		+	+		tr					p
RN-11	11RN5T_02G	WH	+ + +	+ +		+																
RN-12	RN12-2014-1	WH	+ +	+ +		tr	tr		+		1?											
RN-10	RN10-2014-1	WH	+ + +	+	tr	tr	tr															
RN-23	23RN3D-07	upstream	+ + +	+		+	+				2		tr									
RN-14	14RN1-07	upstream	+ + +	tr		tr							+		+ +							
RN-11	11RN1-07	upstream	+ + +	+ +	tr	+	tr						tr		+ +							
RN-22	22RN5-07	upstream	+ + +	+ +		tr	tr		tr				tr									
Group IV: upper boiling zone																						
RN-21	21RN-2-07	dnstr on OP1	+ + +	+		+ +	+	+	+			tr			+							
RN-26	RN26-2014-3	dnstr on OP1	+ + +	+		+ +			tr				tr									
RN-11	11RN-3-07	dnstr on OP1	+ + +	tr		+ +		tr	+		2				+							
RN-11	11RNE1-2-07	on FFCV1	+ + +	+		+ +		+	+		1	?	tr		+							
RN-26	RN26-2014-4	on FFCV1	+ + +	+		+		tr					tr									
RN-13	13RN-4	dnstr FFCV1	+ + +	+		+		r?	+													
RN-15	15RN-6	dnstr FFCV1	+ +	+		+		tr	tr				tr		+ + +							
RN-11	11RN-4-07	dnstr OP1	+ + +	tr		+ +	tr		+		1				+							
RN-14	14RN-2-07	dnstr OP1	+ + +	tr		+ +		tr	+				+		tr							
RN-14B	14BRN1-2009	dnstr OP1	+ +	tr		tr			tr				tr		+ + +							
RN-18	18RNE2 2007	dnstr OP1	+ +			+ +		tr	+				tr		+							
RN-22	22RN16-07	dnstr OP1	+ + +	+		+ +	tr	tr	+				tr									
RN-23	23RN- 2009	dnstr OP1	+ + +	tr		+			tr				tr?									
RN-23	23RN-1A/1B 2006	dnstr OP1	+ + +	tr		+ +	tr	+	tr		tr											
RN-23	23RN4-2007	dnstr OP1	+ + +	tr		+		tr							tr							
RN-23	23RN5-2007	dnstr OP1	+ + +	tr		+	tr		tr													
RN-28	RN28-2014-2	dnstr OP1	+ + +	+		+ +			+													
RN-23	23RNEO-2007	dnstr OP1	+ + +	+	tr	tr	tr		tr		2				tr							
RN-23	23RN6-2007	32 m dnstr OP1	+ + +			+ +	tr															
Group V: Separator station and Grey Lagoon																						
-	RNSS-2014-2	SS	+												+ + +		tr					

Semi-quantatative petrographic summary of scaling from the Reykjanes geothermal field. Groups are described in Section 4.1. Abundance of electrum (el) is described using a scale of 1 (low) to 5 (most abundant) to provide a more detailed overview of the presence (or absence) of electrum in scales. Subscript denotes additional observations of Hardardottir (2011). Subscript denotes supplemental mineralogical data derived from XRD analyses. Abundances: + + + = abundant, + + = medium abundance, + = minor, tr = trace, r = rare, p = present in XRD analyses but quantity unknown. Abbreviations: ZnS = sphalerite/wurtzite, cpy = chalcopyrite, py = pyrite, bn = bornite, dg = digenite, cv = covellite, gn = galena, po = pyrrhotite, el = electrum, Ag = native silver directly observed during petrography, Ss = potential sulfosalt phases, mt = magnetite, amSi = amorphous silica, rt = rutile, Feox = Fe-oxides, icb = isocubanite, n.Au = native Au (from XRD), n.Ag = native Ag (from XRD), hm = hematite, go = goethite. Location abbreviations (see Fig. 4): DH = downhole, WH = wellhead, upstr = upstream, dnstr = downstream, OP = orifice plate, FFCV = fluid flow control valve, SS = separator station.

Table 3
Averages of bulk raw geochemical data for Reykjanes scales by scale group and well pressure.

Group		P	N	SiO_2 wt.%	Al_2O_3 wt.%	CaO wt.%	Na_2O wt.%	K_2O wt.%	MgO wt.%	TiO_2 wt.%	P_2O_5 wt.%	C Total wt.%	LOI wt.%	Cu wt.%	Zn wt.%	Pb wt.%	Fe wt.%	S wt.%	Au ppm
5	***All***	***–***	***7***	***65.5***	***0.96***	***0.79***	***2.07***	***0.49***	***1.98***	***–***	***–***	***0.03***	***19.3***	***0.69***	***3.67***	***0.29***	***3.16***	***2.13***	***23.7***
4	***All***	***all***	***61***	***9.27***	***0.42***	***0.28***	***0.27***	***0.17***	***0.40***	***0.01***	***–***	***0.08***	***13.7***	***15.4***	***28.5***	***6.63***	***6.59***	***21.9***	***221.4***
	By well pressure	HP	*38*	10.9	0.39	0.30	0.33	0.14	0.27	–	–	0.05	16.3	11.7	31.3	3.60	6.34	21.9	117.9
		MP	*17*	7.69	0.47	0.34	0.27	0.11	0.52	0.002	–	0.09	13.0	20.9	18.1	13.6	8.26	19.8	358.0
		LP	*6*	31.1	1.47	0.45	0.50	0.42	0.78	–	–	0.13	10.3	12.7	15.8	7.87	5.29	15.1	178.3
3	***All***	***all***	***32***	***7.98***	***1.24***	***0.62***	***0.30***	***0.16***	***1.52***	***0.13***	***–***	***0.05***	***15.4***	***5.04***	***39.4***	***2.16***	***8.83***	***23.8***	***188.5***
	By well pressure	HP	*19*	6.12	1.15	0.76	0.19	0.11	1.12	0.13	–	0.05	15.8	5.78	43.5	1.85	7.41	25.0	228.4
		MP	*11*	16.4	1.38	0.44	0.47	–	1.84	–	–	–	–	3.40	35.0	1.53	10.6	22.5	135.5
		LP	*2*	13.0	1.31	0.36	0.20	0.34	3.55	–	–	0.07	13.3	7.05	24.0	8.28	12.3	19.9	100.8
2	***All***	***all***	***15***	***16.3***	***3.60***	***2.30***	***0.74***	***0.12***	***3.02***	***0.20***	***–***	***–***	***–***	***4.37***	***17.1***	***0.01***	***23.9***	***13.8***	***83.7***
	By well pressure	HP	*12*	17.6	4.04	2.80	0.91	0.12	3.05	0.24	–	–	–	5.43	20.8	0.004	16.7	15.9	83.9
		MP	*3*	10.9	1.85	0.32	0.04	–	2.90	0.03	–	–	–	0.15	2.15	0.02	52.8	5.5	82.7
1	***All***	***all***	***14***	***17.9***	***4.08***	***2.51***	***0.79***	***0.13***	***4.33***	***0.28***	***0.07***	***–***	***11.3***	***1.37***	***27.2***	***0.03***	***12.8***	***17.0***	***65.5***
	By well pressure	HP	*9*	14.8	2.67	1.43	0.69	0.13	4.12	0.09	0.07	–	11.3	1.34	34.3	0.001	10.4	20.6	6.05
		MP	*5*	23.5	6.61	4.46	0.98	0.12	4.73	0.62	–	–	–	1.42	14.4	0.06	17.3	10.6	172.5

Group		P	N	Ag ppm	As ppm	Sb ppm	Tl ppm	Hg ppm	Cd ppm	In ppm	Bi ppm	Ge ppm	Ga ppm	Mo ppm	Mn ppm	V ppm	Sn ppm	W ppm	Ni ppm	Cr ppm	Co ppm	Te ppm	Se ppm
5	***All***	***–***	***7***	***58.2***	***6.52***	***1.73***	***0.10***	***–***	***271.0***	***–***	***2.00***	***–***	***27.8***	***7.00***	***1347***	***15.2***	***–***	***8.00***	***–***	***62.0***	***8.77***	***67.0***	***57.0***
4	***All***	***all***	***61***	***6612***	***253.7***	***17.3***	***0.27***	***18.9***	***1853***	***0.55***	***3.69***	***1.00***	***3.65***	***11.2***	***2355***	***35.9***	***10.6***	***2.52***	***17.5***	***101.0***	***59.7***	***30.2***	***526.9***
	By well	HP	*38*	2943	308.4	18.1	0.43	10.8	2994	0.06	0.80	1.00	3.33	13.6	2620	41.7	3.95	1.50	13.3	176.3	78.0	17.7	409.9
	pressure	MP	*17*	10008	185.2	19.3	0.20	46.0	140.5	–	1.10	–	2.60	4.00	5135	21.5	–	–	–	43.0	1.55	49.0	867.0
		LP	*6*	10676	39.5	24.7	0.17	14.0	108.0	0.04	0.40	–	13.3	9.00	2376	61.6	1.00	1.10	30.0	123.0	19.0	–	350.6
3	***All***	***all***	***32***	***1921***	***279.4***	***26.5***	***0.30***	***14.1***	***4578***	***–***	***10.4***	***5.97***	***9.23***	***19.4***	***1539***	***208.0***	***7.20***	***4.86***	***47.9***	***114.8***	***151.2***	***22.7***	***725.0***
	By well	HP	*19*	2838	342.0	37.9	0.15	–	5384	–	12.9	15.0	7.94	23.1	956.6	105.2	8.55	4.02	56.7	125.8	159.1	25.8	575.6
	pressure	MP	*11*	545.5	18.3	3.98	0.35	14.1	3992	–		1.45	11.2	12.8	2304	413.0	6.24	6.46	41.1	101.6	162.2	21.2	1018
		LP	*2*	766.0	50.9	2.30	–	–	149.0	–	0.40	–	10.7	3.00	2858	109.0	1.00	1.10	20.0	–	15.4	–	532.5
2	***All***	***all***	***15***	***144.8***	***24.0***	***2.71***	***–***	***–***	***1602***	***–***	***–***	***3.50***	***12.9***	***62.8***	***2587***	***98.1***	***17.4***	***19.0****	***231.3***	***280.5***	***170.1***	***13.8***	***204.0***
	By well	HP	*12*	150.7	12.6	1.44	–	–	1558	–	–	–	11.3	51.3	1528	88.9	5.30	16.1*	100.8	175.9	194.1	13.8	213.8
	pressure	MP	*3*	75.0	61.8	7.37	–	–	1779	–	–	3.50	19.1	109.0	6823	153.0	65.9	24.6	753.3	698.7	74.1	–	86.0
1	***All***	***all***	***14***	***87.2***	***22.1***	***1.84***	***0.20***	***–***	***4424***	***–***	***1.11***	***0.50***	***12.0***	***38.5***	***1378***	***191.1***	***20.3***	***7.05***	***186.9***	***434.5***	***391.9***	***60.5***	***562.8***
	By well	HP	*9*	52.1	32.9	1.20	0.20	–	3747	–	1.11	0.50	7.73	17.4	1157	103.7	11.6	7.64	72.9	754.0	535.1	60.5	680.2
	pressure	MP	*5*	122.3	19.4	2.00	–	–	5642	–	–	–	19.6	59.6	1774	348.6	23.7	5.98	392.0	370.6	134.1	–	351.6

Group		P	N	Ir ppb	Ru ppb	Rh ppb	Pd ppb	Re ppm	Ba ppm	Rb ppm	Sr ppm	Cs ppm	Li ppm	Be ppm	B ppm	Br ppm	F ppm	U ppm	Th ppm	Sc ppm	Y ppm
5	***All***	***–***	***7***	***–***	***–***	***–***	***–***	***–***	***37.4***	***13.5***	***27.4***	***0.75***	***11.0***	***6.00***	***30.0***	***159.2***	***–***	***–***	***0.10***	***1.05***	***–***
4	***All***	***all***	***61***	***53.4***	***–***	***–***	***8.90***	***–***	***18.1***	***4.42***	***16.5***	***0.74***	***6.80***	***5.29***	***40.0***	***16.2***	***–***	***0.31***	***0.56***	***2.77***	***0.42***
	By well pressure	HP	*38*	0.06	–	–	11.9	–	11.6	2.78	20.9	0.23	6.50	6.50	40.0	15.8	–	0.22	0.22	1.97	0.70
		MP	*17*	–	–	–	–	–	13.3	3.35	14.0	–	–	–	–	–	–	–	–	1.35	–
		LP	*6*	0.04	–	–	5.85	–	57.3	19.9	18.8	1.50	–	1.50	–	2.80	–	0.40	0.55	–	0.30
3	***All***	***all***	***32***	***–***	***–***	***–***	***–***	***–***	***13.9***	***2.74***	***16.2***	***0.43***	***9.33***	***13.5***	***34.0***	***9.76***	***–***	***0.20***	***0.23***	***2.98***	***1.00***
	By well pressure	HP	*19*	–	–	–	–	–	11.0	3.59	17.2	0.70	22.0	22.0	100.0	13.2	–	0.25	0.23	3.84	1.50
		MP	*11*	–	–	–	–	–	16.3	1.84	14.7	0.30	6.80	5.00	17.5	8.40	–	–	–	2.00	0.40
		LP	*2*	–	–	–	–	–	16.0	5.00	16.0	–	–	–	–	–	–	0.10	0.20	0.40	0.30
2	***All***	***all***	***15***	***–***	***–***	***–***	***–***	***–***	***14.7***	***3.57***	***38.7***	***0.10***	***–***	***–***	***40.0***	***14.3***	***–***	***0.20***	***–***	***6.96***	***3.37***
	By well pressure	HP	*12*	–	–	–	–	–	14.7	3.57	43.2	0.10	–	–	40.0	14.3	–	–	–	7.99	4.11
		MP	*3*	–	–	–	–	–	–	–	20.7	–	–	–	–	–	–	0.20	–	0.75	0.40
1	***All***	***all***	***14***	***–***	***–***	***–***	***–***	***0.04***	***20.4***	***2.39***	***59.3***	***0.75***	***7.10***	***2.43***	***–***	***9.85***	***–***	***0.17***	***0.30***	***6.80***	***5.24***
	By well pressure	HP	*9*	–	–	–	–	0.04	12.8	2.89	33.4	0.75	14.3	0.30	–	10.6	–	0.18	–	2.13	1.51
		MP	*5*	–	–	–	–	–	34.2	1.50	106.0	–	3.50	3.50	–	4.50	–	0.16	0.30	15.2	12.0

Group		P	N	Zr ppm	Nb ppm	Ta ppm	Hf ppm	La ppm	Ce ppm	Pr ppm	Nd ppm	Sm ppm	Eu ppm	Gd ppm	Tb ppm	Dy ppm	Ho ppm	Er ppm	Tm ppm	Yb ppm	Lu ppm
5	***All***	***–***	***7***	***8.50***	***1.00***	***–***	***–***	***1.55***	***0.70***	***–***	***0.20***	***–***	***–***	***–***	***–***	***0.10***	***–***	***–***	***–***	***–***	***–***
4	***All***	***all***	***61***	***9.10***	***3.00***	***0.68***	***13.5***	***1.41***	***1.53***	***0.29***	***1.72***	***0.35***	***0.30***	***0.28***	***–***	***0.45***	***–***	***0.17***	***–***	***1.10***	***0.11***
	By well pressure	HP	*38*	8.43	–	1.25	10.3	2.08	1.44	0.32	2.59	0.84	0.65	0.32	–	0.56	–	0.20	–	1.10	0.10
		MP	*17*	–	–	–	–	0.50	–	–	–	0.15	–	–	–	–	–	–	–	–	–
		LP	*6*	17.0	–	0.50	10.2	0.65	1.03	0.30	0.58	0.10	0.08	0.20	–	0.20	–	–	–	–	–
3	***All***	***all***	***32***	***13.3***	***1.00***	***0.10***	***8.34***	***0.73***	***1.48***	***0.22***	***0.43***	***0.23***	***0.17***	***0.31***	***0.10***	***0.53***	***–***	***0.38***	***–***	***0.66***	***0.20***
	By well pressure	HP	*19*	16.5	1.00	0.10	12.6	0.70	1.48	0.22	0.40	0.27	0.17	0.38	0.10	0.53	–	0.38	–	0.66	0.20
		MP	*11*	–	–	–	3.00	–	–	–	–	0.10	–	0.10	–	–	–	–	–	–	–
		LP	*2*	7.00	–	0.10	5.10	1.00	1.50	0.19	0.60	–	–	0.10	–	–	–	–	–	–	–

(*continued on next page*)

Table 3 (*continued*)

Group		P	N	Zr ppm	Nb ppm	Ta ppm	Hf ppm	La ppm	Ce ppm	Pr ppm	Nd ppm	Sm ppm	Eu ppm	Gd ppm	Tb ppm	Dy ppm	Ho ppm	Er ppm	Tm ppm	Yb ppm	Lu ppm
2	***All***	***all***	***15***	***–***	***3.91****	***0.35****	***13.3***	***–***	***3.49***	***0.46***	***0.73***	***0.41***	***0.24***	***0.65***	***0.18***	***0.82***	***0.25***	***0.52***	***0.10***	***0.43***	***0.12***
	By well pressure	HP	*12*	–	3.91*	0.35*	–	–	3.49	0.46	0.78	0.41	0.24	0.65	0.18	0.82	0.25	0.52	0.10	0.43	0.13
		MP	*3*	–	–	–	13.3	–	–	–	0.50	–	–	–	–	–	–	–	–	–	0.09
1	***All***	***all***	***14***	***7.00***	***5.70***	***0.85***	***10.0***	***1.96***	***4.73***	***0.68***	***3.70***	***1.58***	***0.57***	***1.07***	***0.45***	***1.36***	***0.65***	***0.87***	***0.25***	***0.67***	***0.09***
	By well pressure	HP	*9*	7.00	1.40	1.20	10.0	0.85	1.77	0.20	1.10	0.20	0.08	0.29	–	0.38	–	0.23	–	0.17	–
		MP	*5*	–	6.78	0.50	10.0	3.74	10.1	1.34	7.34	1.86	0.76	2.32	0.45	2.34	0.65	1.64	0.25	1.28	0.09

Average values of raw geochemical data for scaling from the Reykjanes geothermal system by scale group (see text Section 4.1) and well pressure. Abbreviations for pressure (P) of wells: HP = high–pressure, MP = medium–pressure, LP = low–pressure. N = number of samples, na = not analyzed, and '–' = not above detection.

Table 4
Raw bulk geochemistry of Reykjanes scale samples by specific locality and well pressure.

Group	Location	P	N	SiO_2 wt.%	Al_2O_3 wt.%	CaO wt.%	Na_2O wt.%	K_2O wt.%	MgO wt.%	TiO_2 wt.%	P_2O_5 wt.%	C Total wt.%	LOI wt.%	Cu wt.%	Zn wt.%	Pb wt.%	Fe wt.%	S wt.%	Au ppm
5	Grey Lagoon	**–**	*4*	63.9	0.23	0.78	2.74	0.55	0.18	–	–	0.02	28.0	0.14	0.28	0.14	0.21	0.12	0.26
	Venthouse	**–**	*1*	92.2	0.11	0.33	0.47	0.16	–	–	–	–	6.38	0.07	–	–	0.20	0.05	0.16
	Separator station	**–**	*2*	55.1	2.84	1.05	1.54	0.56	3.78	–	–	0.04	6.03	1.85	5.37	0.36	9.08	4.17	70.6
4	32 m downstream	HP	*1*	2.82	0.57	0.26	0.33	0.21	0.30	–	–	0.02	14.2	13.8	44.9	0.64	5.11	29.8	82.4
	Downstream after OP1	HP	*19*	7.17	0.82	0.36	0.16	0.13	1.35	0.11	–	0.05	15.8	7.43	39.5	3.88	7.20	24.3	293.2
		MP	*4*	7.69	0.47	0.34	0.27	0.11	0.52	0.002	–	0.09	13.0	20.9	18.1	13.6	8.26	19.8	358.0
		LP	*5*	31.1	1.47	0.45	0.50	0.42	0.78	–	–	0.13	10.3	12.7	15.8	7.87	5.29	15.1	178.3
	Right after OP1	HP	*2*	35.9	0.35	0.28	0.28	0.12	0.30	–	–	–	–	9.58	14.5	5.16	6.17	13.1	125.5
	Downstream on FFCV1	HP	*6*	3.46	0.27	0.15	0.08	0.12	0.33	–	–	0.04	15.0	15.2	39.0	1.34	7.56	26.1	267.7
		MP	*10*	4.32	0.29	0.17	0.10	0.04	0.53	0.002	–	–	12.1	20.0	21.3	14.9	8.41	21.8	416.1
		LP	*1*	2.06	0.11	0.07	0.09	–	0.47	–	–	0.17	11.0	31.2	16.3	14.4	5.79	23.2	163.0
	Downstream on OP1	HP	*9*	5.95	0.23	0.39	0.33	0.09	0.31	0.03	–	0.05	15.4	14.9	37.3	1.38	4.83	24.3	195.6
		MP	*3*	4.98	0.34	0.21	0.21	0.04	0.39	–	–	0.09	12.9	21.9	21.5	13.4	6.09	21.3	259.7
		LP	*na*	na	na	na	na	na	na	na	na	na	na	na	na	na	na	na	na
3	Upstream on OP1	HP	*6*	2.13	0.29	0.12	0.03	0.09	0.25	0.03	–	0.04	16.7	4.24	55.9	0.13	2.97	29.9	271.2
		MP	*na*	na	na	na	na	na	na	na	na	na	na	na	na	na	na	na	na
		LP	*1*	3.21	0.42	0.14	0.01	–	0.35	–	–	–	–	2.10	41.0	9.54	9.16	25.1	65.5
	Upstream on FFCV1	HP	*2*	4.83	0.36	0.16	0.14	0.08	0.70	–	–	0.06	14.89	4.23	52.8	0.28	5.20	25.5	411.0
		MP	*1*	14.2	1.00	0.48	0.04	–	1.69	–	–	–	–	7.00	15.4	11.0	13.4	16.2	439.0
		LP	*na*	na	na	na	na	na	na	na	na	na	na	na	na	na	na	na	na
	Upstream	HP	*5*	7.46	1.41	0.57	0.13	–	1.68	0.18				10.9	32.1	6.06	8.51	23.1	256.2
		MP	*na*	na	na	na	na	na	na	na	na	na	na	na	na	na	na	na	na
		LP	*1*	22.8	2.20	0.59	0.39	0.34	6.76	–	–	–	–	12.0	6.94	7.02	15.5	14.6	136.0
	Wellhead	HP	*2*	12.0	1.01	0.35	0.21	0.20	2.35	–	–	–	13.1	3.15	39.7	0.05	9.62	18.7	134.0
		MP	*1*	23.7	1.64	0.83	0.58	–	3.80	–	–	–	–	6.37	7.27	5.75	16.2	11.4	250.0
	Downhole to 904 m	HP	*4*	8.11	2.60	2.15	0.41	–	1.33	0.13	–	–	–	3.81	36.6	0.01	12.7	22.7	85.6
	Downhole to 904 m	MP	*9*	11.3	1.39	0.40	0.50	–	1.64	–	–	–	–	2.67	40.3	0.01	9.72	24.5	89.0
2	RN–10	HP	*12*	17.6	4.04	2.80	0.91	0.12	3.05	0.24	–	–	–	5.43	20.8	0.004	16.7	15.9	83.9
	RN–22	MP	*3*	10.9	1.85	0.32	0.04	–	2.90	0.03	–	–	–	0.15	2.15	0.02	52.8	5.5	82.7
1	RN10	HP	*8*	13.4	2.73	1.20	0.70	0.12	3.58	0.09	–	–	–	1.50	38.2	0.001	8.10	21.8	1.69
	RN17B	HP	*1*	26.6	2.26	3.30	0.64	0.16	8.39	0.08	0.07	–	11.3	0.08	3.14	–	28.7	10.5	40.9
	RN–22	MP	*5*	23.5	6.61	4.46	0.98	0.12	4.73	0.62	–	–	–	1.42	14.4	0.06	17.3	10.6	172.5

Group	Location	P	N	Ag ppm	As ppm	Sb ppm	Tl ppm	Hg ppm	Cd ppm	In ppm	Bi ppm	Ge ppm	Ga ppm	Mo ppm	Mn ppm	V ppm	Sn ppm	W ppm	Ni ppm
5	Grey Lagoon	**–**	*4*	56.1	8.00	1.40	–	–	–	–	–	–	23.2	–	241.8	11.0	–	–	–
	Venthouse	**–**	*1*	10.0	1.00	3.10	–	–	–	–	–	–	63.0	–	542.2	–	–	8.00	–
	Separator station	**–**	*2*	84.5	7.60	1.00	0.10	–	271.0	–	2.0	–	12.6	7.0	3960	21.5	–	–	–
4	32 m downstream	HP	*1*	1290	25.4	–	–	–	5220	0.06	0.7	–	1.0	2.0	426.0	119.0	–	–	–
	Downstream after OP1	HP	*19*	3223	434.4	35.6	–	–	5117	–	11.4	–	7.1	13.8	1957	103.0	10.1	2.68	50
		MP	*4*	10008	185.2	19.3	0.20	46	140.5	–	1.1	–	2.6	4.0	5135	21.5	–	–	–
		LP	*5*	10676	39.5	24.7	0.17	14	108.0	0.04	0.4	–	13.3	9.0	2376	61.6	1.00	1.10	30
	Right after OP1	HP	*2*	3045	176.5	39.6	0.70	–	92.0	–	–	–	12.1	2.5	2175	48.0	–	–	10
	Downstream on FFCV1	HP	*6*	5575	161.7	11.9	–	–	1586	1.05	11.2	–	2.0	5.5	988.8	26.3	22.1	11.1	10
		MP	*10*	12083	90.3	9.10	0.15	18.4	207.8	–	0.7	–	2.7	2.0	2532	11.0	–	3.00	35
		LP	*1*	23200	–	–	–	–	160.0	–	0.4	–	2.0	–	1007	20.0	–	–	–
	Downstream on OP1	HP	*9*	3877	504.9	17.0	–	–	3219	–	16.8	–	1.8	11.4	1151	25.1	–	1.25	15.7
		MP	*3*	9940	132.1	30.7	–	32	203.0	–	0.4	–	1.6	–	3055	33.3	–	–	–
		LP	*na*	na	na	na	na	na	na	na	na	na	na	na	na	na	na	na	na

(*continued on next page*)

Table 4 (*continued*)

Group	Location	P	N	Ag ppm	As ppm	Sb ppm	Tl ppm	Hg ppm	Cd ppm	In ppm	Bi ppm	Ge ppm	Ga ppm	Mo ppm	Mn ppm	V ppm	Sn ppm	W ppm	Ni ppm
3	Upstream on OP1	HP	*6*	5734	1299.3	118.5	–	–	10078	–	14.0	–	5.7	28.8	840.0	78.3	8.17	2.40	–
		MP	*na*	na	na	na	na	na	na	na	na	na	na	na	na	na	na	na	na
		LP	*1*	272.0	50.9	2.30	–	–	158.0	–	–	–	7.4	2.0	1310	17.0	–	1.10	20
	Upstream on FFCV1	HP	*2*	282.5	24.4		–	–	6950	–	9.4	–	15.0	5.0	880.3	19.0	30.3	–	30
		MP	*1*	3580		5.20	–	–	32.0	–	–	–	6.2	–	8550	–	–	–	–
		LP	*na*	na	na	na	na	na	na	na	na	na	na	na	na	na	na	na	na
	Upstream	HP	*5*	3049	24.6	4.68	–	–	3398	–	–	–	5.4	6.5	768.8	242.0	7.30	3.30	80
		MP	*na*	na	na	na	na	na	na	na	na	na	na	na	na	na	na	na	na
		LP	*1*	1260	–	–	–	–	140.0	–	0.4	–	14.0	4.0	4407	201.0	1.00	–	–
	Wellhead	HP	*2*	1397	53.0	0.80	0.10	–	1001	–	–	15.0	8.2	10.0	985.4	101.0	3.00	–	14
		MP	*1*	632.0	–	1.10	–	–	22.0	–	–	–	10.2	–	9850	8.00	–	–	–
	Downhole to 904 m	HP	*4*	231.3	10.2	1.95	0.20	–	2233	–	–	–	10.8	43.8	1390	53.8	5.43	7.80	67.5
	Downhole to 904 m	MP	*9*	198.7	18.3	4.80	0.35	14.1	4873	–	–	1.5	11.9	12.8	771.4	458.0	6.24	6.46	41.1
2	RN–10	HP	*12*	150.7	12.6	1.44	–	–	1558	–	–	–	11.3	51.3	1528	88.9	5.30	19.0*	100.8
	RN–22	MP	*3*	75.0	61.8	7.37	–	–	1779	–	–	3.5	19.1	109.0	6823	153.0	65.9	24.6	753.3
1	RN10	HP	*8*	66.0	–	–	–	–	4128	–	2.00	–	6.96	4.25	771.5	106.4	10.2	7.63	25.0
	RN17B	HP	*1*	24.4	32.9	1.20	0.20	–	699.0	–	0.21	0.5	13.9	69.9	4244	82.0	13.0	7.80	456.0
	RN–22	MP	*5*	122.3	19.4	2.00	–	–	5642	–	–	–	19.6	59.6	1774	348.6	23.7	5.98	392.0

Group	Location	P	N	Cr ppm	Co ppm	Te ppm	Se ppm	Ir ppb	Ru ppb	Rh ppb	Pd ppb	Re ppm	Ba ppm	Rb ppm	Sr ppm	Cs ppm	Li ppm	Be ppm	B ppm	Br ppm
5	Grey Lagoon	–	*4*	47.0	2.00	–	20.0	–	–	–	–	–	26.0	11.5	28.0	0.2	–	–	30	212.0
	Venthouse	–	*1*	–	–	–	–	–	–	–	–	–	8.0	6.00	4.0	–	–	1.0	–	–
	Separator station	–	*2*	69.5	12.2	67.0	75.5	–	–	–	–	–	75.0	20.1	38.0	1.3	11.0	11.0	–	53.5
4	32 m downstream	HP	*1*	–	129.0	–	497.0	0.06	–	–	11.9	–	15.0	6.00	7.0	–	–	–	–	–
	Downstream after OP1	HP	*19*	77.0	142.3	35.7	698.3	–	–	–	–	–	12.6	2.64	14.9	–	13.5	13.5	100	3.70
		MP	*4*	43.0	1.55	49.0	867.0	–	–	–	–	–	13.3	3.35	14.0	–	–	–	–	–
		LP	*5*	123.0	19.0	–	350.6	0.04	–	–	5.85	–	57.3	19.9	18.8	1.5	–	1.5		2.80
	Right after OP1	HP	*2*	–	2.75	9.0	238.5	–	–	–	–	–	8.0	4.10	16.0	0.1	–		40	23.4
	Downstream on FFCV1	HP	*6*	–	47.0	14.8	434.5	–	–	–	–	–	54.7	2.00	19.0	–	–	–	–	–
		MP	*10*	37.7	27.2	69.7	864.5	–	–	–	–	–	4.0	–	9.7	–	–	–	–	–
		LP	*1*	–	–	–	587.0	160.0	–	–	–	–	–	–	2.0	–	–	–	–	–
	Downstream on OP1	HP	*9*	–	86.1	–	447.1	–	–	–	–	–	15.0	1.63	14.0	–	7.0	7.0	–	21.7
		MP	*3*	–	2.00	–	515.7	–	–	–	–	–	7.0	0.50	8.0	–	–	–	–	–
		LP	*na*	na	na	na	na	na	na	na	na	na	na	na	na	na	na	na	na	na
3	Upstream on OP1	HP	*6*	–	302.7	35.5	669.7	–	–	–	–	–	12.0	–	8.5	–	–	–	–	–
		MP	*na*	na	na	na	na	na	na	na	na	na	na	na	na	na	na	na	na	na
		LP	*1*	–	27.8	–	619.0	–	–	–	–	–	–	–	9.0	–	–	–	–	–
	Upstream on FFCV1	HP	*2*	–	108.5	26.0	802.5	–	–	–	–	–	15.0	–	11.0	–	–	–	–	–
		MP	*1*	–	0.60	63.0	526.0	–	–	–	–	–	7.0	–	19.0	–	–	–	–	–
		LP	*na*	na	na	na	na	na	na	na	na	na	na	na	na	na	na	na	na	na
	Upstream	HP	*5*	77.0	76.5	16.0	832.2	–	–	–	–	–	10.7	1.45	19.2	–	22.0	22.0	100	–
		MP	*na*	na	na	na	na	na	na	na	na	na	na	na	na	na	na	na	na	na
		LP	*1*	–	3.00	–	446.0	–	–	–	–	–	16.0	5.00	23.0	–	–	–	–	–
	Wellhead	HP	*2*	–	47.9	–	216.5	–	–	–	–	–	12.0	8.70	14.5	0.7	–	–	–	–
		MP	*1*	–	0.50	58.0	374.0	–	–	–	–	–	13.0	3.30	26.0	–	5.0	5.00	–	3.70
	Downhole to 904 m	HP	*4*	150.3	128.0	–	180.0	–	–	–	–	–	9.75	2.10	27.8	–	–	–	–	13.2
	Downhole to 904 m	MP	*9*	101.6	198.1	11.4	1144	–	–	–	–	–	17.7	1.68	13.0	0.3	7.3	–	18	9.58
2	RN–10	HP	*12*	175.9	194.1	13.8	213.8	–	–	–	–	–	14.7	3.57	43.2	0.1	–	–	40	14.3
	RN–22	MP	*3*	698.7	74.1	–	86.0	–	–	–	–	–	–	–	20.7	–	–	–	–	–
1	RN10	HP	*8*	–	575.3	68.0	763.0	–	–	–	–	–	9.13	2.70	29.8	0.7	–	–	–	9.82
	RN17B	HP	*1*	754.0	214.0	0.4	17.8	–	–	–	–	0.04	42.0	4.40	62.6	0.8	14.3	0.3	–	15.4
	RN–22	MP	*5*	370.6	134.1	–	351.6	–	–	–	–	–	34.2	1.50	106.0	–	3.5	3.5	–	4.50

Group	Location	P	N	F ppm	U ppm	Th ppm	Sc ppm	Y ppm	Zr ppm	Nb ppm	Ta ppm	Hf ppm	La ppm	Ce ppm	Pr ppm	Nd ppm	Sm ppm	Eu ppm	Gd ppm
5	Grey Lagoon	–	*4*	–	–		1.13	–	8.50	–	–	–	2.35	0.80	–	0.20	–	–	–
	Venthouse	–	*1*	–	–	–	–	–	–	1.0	–	–	–	–	–	–	–	–	–
	Separator station	–	*2*	–	–	0.10	0.80	–	–	–	–	–	0.75	0.60	–	0.20	–	–	–
4	32 m downstream	HP	*1*	–	–	0.10	–	–	–	–	–	–	0.30	1.00	0.09	0.40	–	–	0.1
	Downstream after OP1	HP	*19*	–	0.20	0.23	3.44	0.8	13.3	–	0.1	10.1	0.70	1.24	0.18	0.43	0.30	0.14	0.3
		MP	*4*	–	–	–	1.35	–	–	–	–	–	0.50	–	–	–	0.15	–	–
		LP	*5*	–	0.40	0.55	–	0.3	17.0	–	0.5	10.2	0.65	1.03	0.30	0.58	0.10	0.08	0.2
	Right after OP1	HP	*2*	–	–	–	0.30	–	–	–	–	–	–	–	–	–	–	–	–
	Downstream on FFCV1	HP	*6*	–	0.28	0.38	5.87	0.1	5.0	3.0	0.2	5.2	1.52	2.40	0.28	1.65	0.25	0.07	0.2
		MP	*10*	–	1.00	–	3.52	–	–	–	–	–	2.40	2.50	–	–	0.20	–	–
		LP	*1*	–	–	–	–	–	–	–	–	–	–	–	–	–	–	–	–
	Downstream on OP1	HP	*9*	–	0.36	3.50	2.00	0.2	–	–	–	22.5	0.80	1.05	0.08	0.55	0.16	–	–
		MP	*3*	–	0.30	–	0.40	0.2	10.0	–	–	–	0.20	0.30	–	0.20	–	–	–
		LP	*na*	–	na	na	na	na	na	na	na	na	na	na	na	na	na	na	na

(*continued on next page*)

Table 4 (*continued*)

Group	Location	P	N	F ppm	U ppm	Th ppm	Sc ppm	Y ppm	Zr ppm	Nb ppm	Ta ppm	Hf ppm	La ppm	Ce ppm	Pr ppm	Nd ppm	Sm ppm	Eu ppm	Gd ppm
3	Upstream on OP1	HP	*6*		0.25	0.40	2.80	0.4	16.5	–	0.1	0.5	0.57	1.05	0.19	0.45	–	0.07	0.1
		MP	*na*	–	na	na	na	na	na	na	na	na	na	na	na	na	na	na	na
		LP	*1*	–	0.10	–	–	0.3	–	–	–	10.0	–	–	–	–	–	–	–
	Upstream on FFCV1	HP	*2*	–	–	0.20	1.20	–	–	–	–	10.0	1.05	1.00	0.06	0.20	–	–	–
		MP	*1*	–	–	–	2.20	–	–	–	–	–	–	–	–	–	–	–	–
		LP	*na*	–	na	na	na	na	na	na	na	na	na	na	na	na	na	na	na
	Upstream	HP	*5*	–	0.25	0.10	5.60	1.1	–	–	–	20.0	0.55	2.00	0.40	0.50	0.30	0.20	0.7
		MP	*na*	–	na	na	na	na	na	na	na	na	na	na	na	na	na	na	na
		LP	*1*	–	0.10	0.20	0.40	–	7.0	–	0.1	0.2	1.00	1.50	0.19	0.60	–	–	0.1
	Wellhead	HP	*2*	–	–	–	0.60	0.1	–	1.0	–	–	0.70	0.50	0.12	0.30	–	–	–
		MP	*1*	–	–	–	4.80	–	–	–	–	–	–	–	–	–	–	–	–
	Downhole to 904 m	HP	*4*	–	–	–	4.50	2.63	–	–	–	–	–	2.33	0.27	–	0.25	0.20	0.38
	Downhole to 904 m	MP	*9*	–	–	–	1.40	0.40	–	–	–	3.0	–	–	–	–	0.10	–	0.10
2	RN–10	HP	*12*	–	–	–	7.99	4.11	–	3.91*	0.35*	–	–	3.49	0.46	0.78	0.41	0.24	0.65
	RN–22	MP	*3*	–	0.20	–	0.75	0.40	–	–	–	13.3	–	–	–	0.50	–	–	–
1	RN10	HP	*8*	–	0.18	–	2.13	1.50	–	–	1.20	12.5	0.89	1.81	0.20	1.17	–	0.10	0.30
	RN17B	HP	*1*	–	–	–	2.20	1.60	7.00	1.40	–	0.2	0.60	1.40	0.20	0.70	0.20	0.06	0.20
	RN–22	MP	*5*	–	0.16	0.30	15.2	12.0	–	6.78	0.50	10.0	3.74	10.1	1.34	7.34	1.86	0.76	2.32

Group	Location	P	N	Tb ppm	Dy ppm	Ho ppm	Er ppm	Tm ppm	Yb ppm	Lu ppm
5	Grey Lagoon	–	*4*	–	0.1	–	–	–	–	–
	Venthouse	–	*1*	–	–	–	–	–	–	–
	Separator station	–	*2*	–	–	–	–	–	–	–
4	32 m downstream	HP	*1*	–	0.1	–	–	–	–	–
	Downstream after OP1	HP	*19*	0.10	0.5	–	0.5	–	1.25	0.18
		MP	*4*	–	–	–	–	–	–	–
		LP	*5*	–	0.2	–	–	–	–	–
	Right after OP1	HP	*2*	–	–	–	–	–	–	–
	Downstream on FFCV1	HP	*6*	–	0.2	–	0.1	–	–	–
		MP	*10*	–	–	–	–	–	–	–
		LP	*1*	–	–	–	–	–	–	–
	Downstream on OP1	HP	*9*	–	–	–	–	–	–	0.13
		MP	*3*	–	–	–	–	–	–	–
		LP	*na*	na	na	na	na	na	na	na
3	Upstream on OP1	HP	*6*	–	0.2	–	–	–	2.10	0.20
		MP	*na*	na	na	na	na	na	na	na
		LP	*1*	–	–	–	–	–	–	–
	Upstream on FFCV1	HP	*2*	–	–	–	–	–	–	–
		MP	*1*	–	–	–	–	–	–	–
		LP	*na*	na	na	na	na	na	na	na
	Upstream	HP	*5*	0.10	0.7	–	0.5	–	0.40	–
		MP	*na*	na	na	na	na	na	na	na
		LP	*1*	–	–	–	–	–	–	–
	Wellhead	HP	*2*	–	–	–	–	–	–	–
		MP	*1*	–	–	–	–	–	–	–
	Downhole to 904 m	HP	*4*	0.10	0.60	–	0.33	–	0.27	–
	Downhole to 904 m	MP	*9*	–	–	–	–	–	–	–
2	RN–10	HP	*12*	0.18	0.82	0.25	0.52	0.10	0.43	0.13
	RN–22	MP	*3*	–	–	–	–	–	–	0.9
1	RN10	HP	*8*	–	0.40	–	0.24	–	0.18	–
	RN17B	HP	*1*	–	0.30	–	0.20	–	0.10	–
	RN–22	MP	*5*	0.45	2.34	0.65	1.64	0.25	1.28	0.09

Average values of raw geochemical data for scaling from the Reykjanes geothermal system sorted by groups (see text Section 4.1), well pressure, and specific location of sampling. Abbreviations for pressure (P) of wells: HP = high–pressure, MP = medium–pressure, LP = low–pressure. N = number of samples analyzed, and '–' = not above detection. Location abbreviations: OP = orifice plate, FFCV = fluid flow control valve.

21, 22, 23, 24, 26, and 28; V) in distal surface pipes from the separation station to the Grey Lagoon (Table A1).

4.1. Scale mineralogy

4.1.1. Group I scales: below the boiling zone

These samples represent mineral scales that precipitated directly from unboiled fluids at depth in the Reykjanes geothermal system. Fourteen composite samples were collected from three high-pressure wells beneath the boiling zone: between 1575 m and 1832 m depth in RN-10, between 1636 m and 1646 m depth in RN-22, and at 2700 m depth in RN-17B. Scales in RN-10 are at least 1 mm thick (maximum chip size ~5 mm) but the exact thickness at each sampling point is unknown due to the rotary drilling method of cleaning the wells and the highly fragmented nature of the scale samples. The deepest scales in RN-22 were no more than 2 mm thick (Hardardóttir, 2014).

The most common sulfides below the boiling zone in both RN-10 and RN-22 are dark-red pyramidal wurtzite (Fig. 6a) and dark brown to black sphalerite (Table 2). They are equally abundant and exhibit a variety of textures, most commonly as lath-shaped crystals up to 3 mm in size and as fine-grained dendrites, often with a preferred alignment or growth direction, often with chalcopyrite (Fig. 6b). In RN-10,

Table 5
Average trace element composition of selected minerals from EMPA. Data is in wt.%.

Depth (m)	Mineral	No. of analyses	Fe	S	Cu	Zn	Pb	Au	Ag
660	sph	10	3.69	32.54	2.02	59.45	0.109	0.084	0.162
	cpy	8	27.16	33.70	30.90	7.13	0.073	0.099	0.046
	bn	–	–	–	–	–	–	–	–
	py	–	–	–	–	–	–	–	–
	el	–	–	–	–	–	–	–	–
1098	sph	3	3.53	33.47	0.400	62.73	0.048	0.064	–
	cpy	3	30.63	35.08	34.38	–	0.076	0.092	0.025
	bn	3	14.57	29.69	54.92	–	0.084	0.051	0.516
	py	3	47.75	54.04	bdl	bdl	0.118	0.129	bdl
	el	4	2.14	0.662	2.97	1.40	–	76.18	20.26
1668	sph	3	7.43	34.04	0.879	57.07	0.087	0.105	bdl
	cpy	3	30.76	35.21	34.27	–	0.142	0.123	0.010
	bn	–	–	–	–	–	–	–	–
	py	–	–	–	–	–	–	–	–
	el	–	–	–	–	–	–	–	–
1832	sph	3	4.87	33.81	0.314	60.97	0.089	0.128	bdl
	cpy	6	30.94	35.27	33.66	0.098	0.089	0.106	bdl
	bn	–	–	–	–	–	–	–	–
	py	1	45.07	52.11	1.53	0.518	0.214	0.082	0.034
	el	–	–	–	–	–	–	–	–

Microprobe analyses on sphalerite, chalcopyrite, bornite, pyrite, and electrum from different depths in well RN-10. Many analyses represent mixed analyses of fine-grained intergrowths of sphalerite, chalcopyrite, and/or bornite. Due to the small size of electrum/discrete Au-bearing phases, data for electrum was only obtained from 1098 m depth, and is semi-quantatative only (Supplementary Table B1). Abbreviations: sph = sphalerite, cpy = chalcopyrite, bn = bornite, py = pyrite, el = electrum.

inclusions of chalcopyrite are abundant, often as aligned crystals within dendritic Zn-sulfides. The chalcopyrite is variably associated with bornite and/or covellite, which are complexly intergrown with the host Zn-sulfide at a micron-scale, giving the sphalerite and wurtzite a mottled appearance (Fig. 6c). The lath-shaped crystals of sphalerite and wurtzite are commonly skeletal and can have high porosity (e.g., Fig. 6a). Sphalerite locally forms 'hopper' crystals (Fig. 6d) indicative of supersaturated solutions where sphalerite crystallized rapidly, leaving gaps between crystal domains and small inclusions of chalcopyrite aligned along growth planes. Wurtzite has two distinct habits (bladed and pyramidal) enabling clear identification in many samples, and was confirmed by XRD (Table 2). It has strong red internal reflections and contains variable amounts of chalcopyrite and associated minor bornite or covellite. At and below 1680 m in RN-10, some wurtzite has a distinctive bladed 'sawtooth' habit, commonly with abundant coarse monomineralic chalcopyrite (Fig. 6e).

Chalcopyrite is present in nearly all scale samples below the boiling zone in RN-10, most commonly as rims on massive sphalerite/wurtzite, as blebs in massive sphalerite/wurtzite, and as coarse, monomineralic blades up to 5 mm in size (Fig. 6f). Coarse, bladed chalcopyrite increases in abundance downhole, particularly between 1737 m and 1800 m depth in RN-10. Chalcopyrite blebs within, and interstitial to Zn-sulfide dendrites and laths in RN-10 are associated with bornite, digenite, and covellite. Unlike RN-10, the deep scales in RN-22 (from 1638 to 1648 m) contain very little to no Cu- or Cu-Fe-sulfides, although this may reflect a sampling bias. Chalcopyrite- and rare pyrite-bearing scales, rock fragments, and clay were found at the bottom of the well liner (~1650 m relative depth) when pulled to surface.

Other sulfides are found in trace quantities in Group I scales. Well-crystallized pyrrhotite, minor skeletal galena, and trace pyrite occurs in scales from 2700 m depth in well RN-17B (see also Seward, 2014), but no pyrrhotite or galena were seen in scales below the boiling zone in wells RN-10 or RN-22. XRD analysis indicates that isocubanite is present at 1800 m and 1832 m depths in RN-10, and covellite between 1575 and 1800 m. There is a thin coating of fine-grained covellite on many samples that is removed during polishing, indicating that it may be due to late oxidation of the samples. One coarse monomineralic pyrite scale was recovered from 1832 m depth in RN-10. Elsewhere, fine-grained euhedral to subhedral pyrite is only rarely found in Zn-sulfides or chalcopyrite; where seen it is commonly brecciated, overgrown and partially replaced.

Coarse, monomineralic magnetite up to 5 mm in size is present at and above 1575 m in RN-10. Below this depth, and in RN-22, magnetite decreases in abundance and only occurs as 5–20 μm disseminations in fine-grained silica. Secondary hematite and goethite occur in samples recovered from 1636 m in RN-22.

Free grains of gold (< 5 μm) were found within sulfide crystals captured on the stainless steel apparatus placed at 2700 m in well RN-17B as part of a downhole experiment (cf. Hardardóttir et al., 2013). The gold is particularly associated with chalcopyrite and pyrrhotite (Fig. 6g). Dendrites of native silver are also common in RN-17B (this study; Fig. 6h). XRD analyses indicate the deep scales from RN-10 and RN-22 also contain minor amounts of amorphous silica, chlorite (chamosite, clinochlore, nimite), epidote, enstatite, diopside, amphibole (hornblende), and clinozoisite. Smectite is present at 1504 m in RN-10, but is not found at greater depths (Table 2).

4.1.2. Group II scales: lower boiling zone

Sulfide scales formed above boiling onset were collected in 15 samples from 1085 to 1504 m in RN-10 and 1050 to 1088 m in RN-22. The scales are dominated by sphalerite and wurtzite, similar to the massive, dendritic, and skeletal Zn-sulfides from deeper in the wells. Wurtzite is present in all samples from this group in RN-10, recognized by its dark red-brown color and hemimorphic pyramidal habit. It is distinct from the lighter-colored wurtzite in the Group I scales and increases in abundance up the well above the onset of boiling. Hopper crystals of Zn-sulfide occur between 1245 m and 1138 m in RN-10. Colloform-banded sphalerite plus chalcopyrite was found in one sample recovered from 1099 m depth (Fig. 6i). The abundance of chalcopyrite increases upwards through the lower boiling zone in well RN-10, with massive coarse chalcopyrite observed in the samples from 1168 m to 1095 m. Chalcopyrite blebs within, and interstitial to, dendritic Zn-sulfide laths are common and occur with variable bornite, covellite and digenite. Bornite and digenite (often replacing sphalerite) increase above 1136 m depth (Table 2), and between 1136 m and 1085 m, they are more abundant than chalcopyrite. Compared to RN-10, Cu-bearing sulfides are relatively rare in RN-22.

Electrum is abundant in Group II scales, between 1148 m and

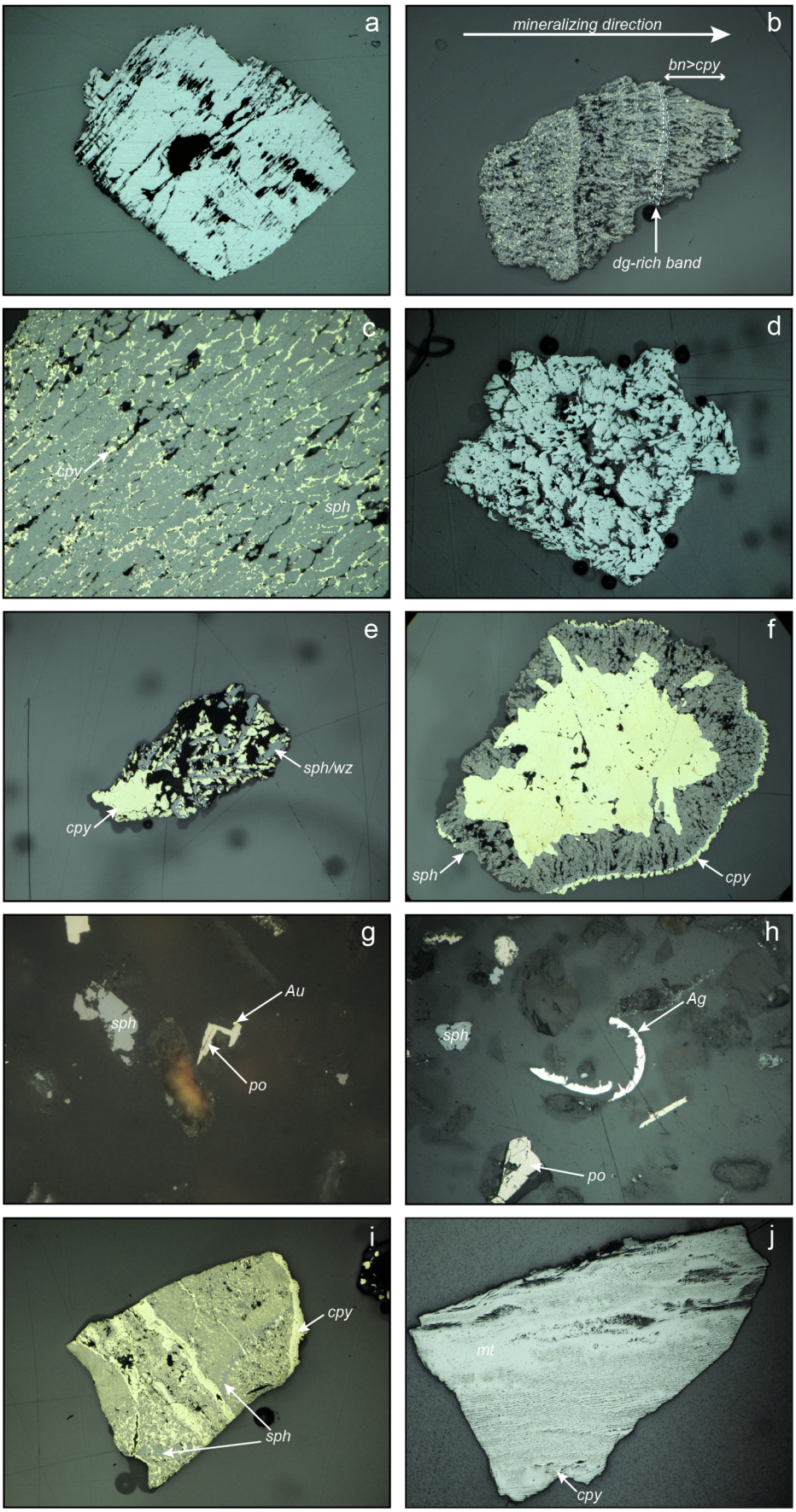

(caption on next page)

Fig. 6. Representative photomicrographs of sulfide scales in the Reykjanes system. FOV = field of view. A) Pyramidal wurtzite (gray) containing minimal inclusions. The wurtzite has a distinctive blocky texture. In Group I scales below the boiling zone near 1800 m depth in high-pressure well RN-10 (sample RN10-2014–1800). FOV = 3 mm. B) At least three stages of growth of dendritic sphalerite (gray) with variable porosity and interstitial chalcopyrite (yellow). Mineral growth (assumed to correspond to flow direction) is from left to right. A less porous more digenite-rich band is indicated by the dashed white lines. The growth band on the far right contains more bornite than chalcopyrite. In Group I scales from below the boiling zone near 1575 m depth in high-pressure well RN-10 (sample RN10-2014–1575). FOV = 3 mm. C) Interstitial chalcopyrite (yellow) and bornite (pink) in low-porosity sphalerite (gray). In Group I scales from below the boiling zone near 1832 m depth in high-pressure well RN-10 (sample RN10-2014–1832). FOV = 0.15 mm. D) Early-stage sphalerite/wurtzite hopper crystals (gray) in Group II scales from the lower boiling zone near 1136 m depth in high-pressure well RN-10 (sample RN10-2014–1136). FOV = 3 mm. E) Zn-sulfide (gray) with distinctive 'sawtooth' habit associated with coarse chalcopyrite (yellow) and minor internal Cu- and Cu-Fe-sulfide inclusions. The chalcopyrite is interstitial to the sphalerite/wurtzite laths. In Group I scales from below the boiling zone near 1575 m depth in high-pressure well RN-10 (sample RN10-2014–1575). FOV = 3 mm. F) Coarse, bladed chalcopyrite (yellow) with later laths of sphalerite (gray) plus interstitial chalcopyrite, and a rim of massive chalcopyrite. In Group I scaling from below the boiling zone near 1800 m depth in high-pressure well RN-10 (sample RN10-2014–1800). FOV = 3 mm. G) Gold grain (dark yellow) associated with pyrrhotite (beige) in Group I scaling from below the boiling zone near 2700 m depth in high-pressure well RN-17B (sample 17RN-2011–2700). FOV = 0.15 mm. H) Dendrites of native Ag (white) with pyrrhotite (beige) and sphalerite (gray) in Group I scaling from below the boiling zone near 2700 m depth in high-pressure well RN-17B (sample 17RN-2011–2700). FOV = 0.15 mm. I) Colloform chalcopyrite (yellow) and sphalerite (gray) in Group II scales from the lower boiling zone near 1099 m depth in high-pressure well RN-10 (sample RN10-2014–1099). FOV = 3 mm. J) Monomineralic banded magnetite (possibly Liesegang texture) in Group III scales from the upper boiling zone near 660 m depth in high-pressure well RN-10 (sample RN10-2014–660). FOV = 3 mm. K) Chip of sphalerite (gray) with high porosity, rimmed by chalcopyrite (yellow) in Group III scales from the upper boiling zone near 660 m depth in high-pressure well RN-10 (sample RN10-2014–660). FOV = 3 mm. l) Gray sphalerite laths (to the left) transitioning into coarser-grained sphalerite altered to digenite (pale blue-gray) and covellite (dark blue), and grading into higher concentrations of fine-grained bornite (red), chalcopyrite (yellow), and covellite. In Group IV scales from the surface boiling zone downstream on the FFCV in high-pressure well RN-11 (sample 11RNE2-07). FOV = 0.7 mm. M) Fine-grained sphalerite laths (gray) grading into a Cu-sulfide-rich band of bornite (pink), and chalcopyrite (yellow). Sphalerite laths again become dominant to the right. Mineralizing growth direction is shown. In Group III scales from the upper boiling zone upstream of the OP in high pressure-well RN-23 (sample 23RN6-2007). FOV = 0.15 mm. N) Fine-grained sphalerite (gray) and galena (light gray) between bornite-rich bands and zones (red). In Group IV scales from the surface boiling zone downstream on the FFCV in low-pressure well RN-18 (sample 18RNE2-2007). FOV = 0.15 mm. O) Sphalerite (gray) partially altered to digenite (blue-gray), bornite (red) and covellite (dark blue) with cooling fractures filled by an unknown secondary mineral. In Group IV scales from the surface boiling zone downstream on the FFCV in low-pressure well RN-18 (sample 18RNE2-2007). FOV = 0.15 mm. P) Early, brecciated pyrite (pale yellow) in chalcopyrite (dark yellow) band and in coarse-grained sphalerite (gray). In Group III scales from the upper boiling zone near 660 m depth in high-pressure well RN-10 (sample RN10-2014–660). FOV = 0.7 mm. In Group IV scales from the surface boiling zone downstream on the OP in high-pressure well RN-22 (sample 22RN-16–07). FOV = 0.7 mm. Q) Fine-grained sphalerite laths with patchy alteration to digenite (light blue) plus isolated areas of covellite (dark blue) after bornite (red) and minor chalcopyrite (yellow). A Cu-sulfide-rich band is outlined by the white dashed lines. Group IV surface boiling zone, downstream on OP, RN-22, sample 22RN-16–07, high-pressure well. FOV = 0.7 mm. R) Fine-grained laths of sphalerite (gray) with minor alteration to digenite (pale blue), transitioning into coarser-grained, less-altered sphalerite laths. The white arrow indicates mineralizing growth direction. In Group IV scales from the surface boiling zone downstream on the OP in high-pressure well RN-23 (sample 23RN-1A). FOV = 0.7 mm. S) Fine-grained sphalerite laths within amorphous silica and minor Cu-Fe-sulfides. Two distinct mineralizing growth (flow) directions are indicated by the white arrows and demarcated by the white dashed line. In Group IV scales from the surface boiling zone downstream of the OP in high-pressure well RN-23 (sample 23RN-1A-2006). FOV = 0.7 mm. T) Coarse sphalerite with low porosity containing interstitial bornite (red), covellite (blue) after rare chalcopyrite. In Group IV scales from the surface boiling zone 32 m downstream of the OP in high-pressure well RN-23 (sample 23RN6-2007). FOV = 0.7 mm. Abbreviations: sph = sphalerite, cpy = chalcopyrite, bn = bornite, cv = covellite, dg = digenite, gn = galena, po = pyrrhotite, mt = magnetite, Au = native Au, Ag = native Ag. (For interpretation of the references to color in this figure legend, the reader is referred to the web version of this article.)

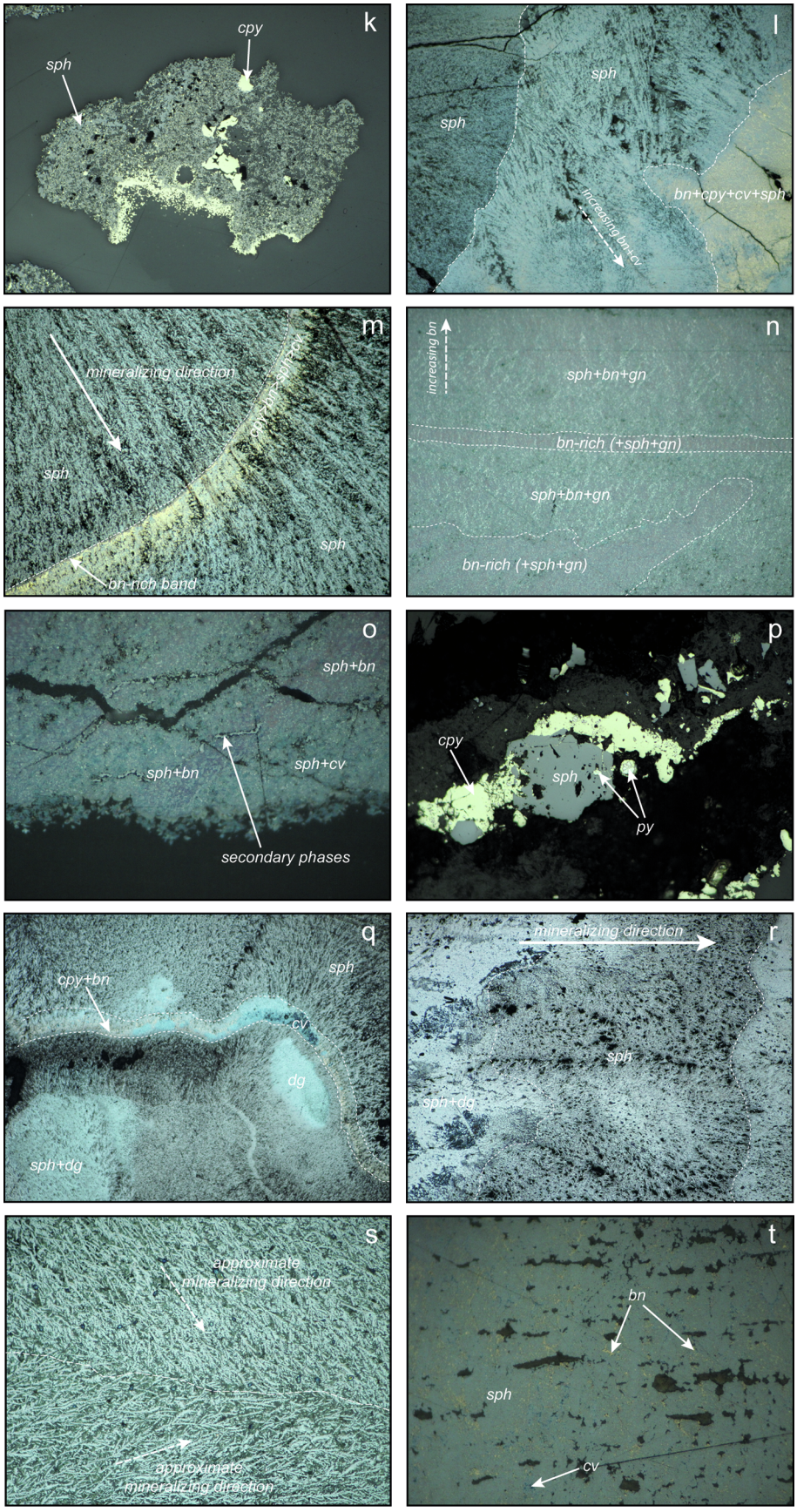

Fig. 6. (*continued*)

1085 m depth in RN-10, and increases in grain size and abundance up the well from the bottom of the boiling zone (Table 2). In all wells electrum is common in dendritic sphalerite and occurs with blebby chalcopyrite as < 0.5–3 μm grains, typically at the grain boundaries between chalcopyrite and sphalerite/wurtzite (Fig. 7a) and only rarely in wurtzite where chalcopyrite is absent. It is coarsest (~8 μm grains) when associated with massive, coarse chalcopyrite, for example at 1098 m in RN-10. It is rarely associated with bornite or covellite. Electrum is also not present in the 'hopper' crystals of Zn-sulfides.

Pyrite was observed as fractured crystals within chalcopyrite bands at downhole depths of 1098 m, 1198 m, and 1245 m in RN-10 but is otherwise uncommon in the lower boiling zone. Magnetite is common in Group II scales as isolated blocky grains with or without chalcopyrite inclusions, and locally with distinctive bands similar to Liesegang banding (Fig. 6j).

Amorphous silica and Fe-Mg silicates (chamosite and clinochlore) are present in Group II scales. Other minerals identified by XRD include illite/montmorillonite, kaolinite, hornblende, enstatite, spinel, garnet (almandine), nontronite, saponite, and zoisite (Table 2) and are likely found in altered basalt chips.

4.1.3. Group III scales: upper boiling zone

Thirteen samples of scales were collected from wells RN-10 and RN-22 between 904 m and the surface wellhead. Nineteen samples were also collected from the top of the boiling zone between the wellhead and the first throttle point (OP). These samples were from high-pressure (32–50 bar) wells RN-10, 11, 14, 14B, 22, 23, and 28, a medium-pressure (28–32 bar) well RN-12, and two low-pressure (25–28 bar) wells RN-13B and 15.

Sphalerite is the dominant sulfide, with minor wurtzite. It has distinctive dendritic and skeletal textures similar to those in Group I and II scales. This is interpreted to reflect early-stage nucleation and very rapid precipitation. Fine-grained sphalerite with high porosity was also observed (Fig. 6k). Pyrite and pyrrhotite are rare; trace pyrite is present at 660 m depth in RN-10 and at between 618 m and 141 m depths in RN-22. Pyrrhotite was also documented in RN-22 and in surface scales by Hardardóttir et al. (2010), but it is not directly associated with either pyrite or magnetite. Magnetite decreases in abundance up the well to ~660 m depth in both in RN-22 and RN-10 (Table 2). Hematite (and maghemite: Hardardóttir, 2011) is more common in the shallow scales, particularly above 669 m in RN-22.

Electrum is abundant at 660 m in RN-10, where it is associated with chalcopyrite at grain boundaries with sphalerite, as in the lower boiling zone (Table 2). Fine-grained (< 1μm) electrum also occurs in fractures in rare brecciated pyrite at 660 m depth but is not associated with pyrite in any other samples in this group. Scales from RN-22, between 669 m and 141 m, contain discrete < 5 μm clusters of native silver intergrown with semi-massive sphalerite and bornite (Hardardóttir et al., 2010).

Closer to the wellhead and first throttle point in the surface pipes, all sulfide minerals in Group III scales become more fine-grained and contain less chalcopyrite. Dendritic and lath-shaped sphalerite are intergrown with chalcopyrite, bornite, and trace digenite (Fig. 6l), often showing a preferred mineralizing direction (Fig. 6m). Mineral abundances vary between wells; the high-pressure well RN-23 has a higher abundance of well-crystallized sphalerite, chalcopyrite, and electrum grains. RN-12 (medium-pressure) and RN-14B (high-pressure) contain less sphalerite but greater amounts of galena (e.g., Fig. 6n), and silver and secondary minerals filling late cooling fractures (Fig. 6o). Trace, brecciated pyrite (< 10 um) is dispersed in chalcopyrite-rich bands in wellhead scales in RN-10 and up to the first orifice plate in RN-11 (Fig. 6p), similar to downhole scales.

Amorphous silica and Fe-Mg silicates (chamosite and clinochlore) are also present in the scales near the wellhead. Other minerals identified by XRD from scales in the upper part of the boiling zone in RN-10 and RN-22 include epidote, clinozoisite, amphibole (hornblende), diopside, spinel, garnet (almandine), wollastonite, micas, and calcite (Table 2). Similar to Group II scale samples, these minerals are likely sourced from altered basalt.

4.1.4. Group IV scales: surface boiling zone

Sixty one samples were collected downstream from the orifice plate (OP) in high-pressure wells (RN-10, 11, 14, 14B, 22, 23, 26, 28), medium-pressure wells (RN-12, 21, 24) and low-pressure wells (RN-13, 13B, 15, 18). These scales are dominated by sphalerite and minor wurtzite intergrown with digenite and bornite within fine-grained silica. The Zn-sulfides have textures that are similar to Group I, II, and III scales but are much finer-grained. Chalcopyrite is much less abundant, and bornite and digenite are the most common Cu-bearing sulfides, particularly on the OP and FFCV (Fig. 6q). Discrete mm-scale bands of the very fine-grained (< 2 μm) Cu- and Cu-Fe-sulfides are often intergrown with bands of similarly fine-grained (~4 μm) Zn-sulfides. Where present, the sphalerite laths commonly have preferred orientations that indicate fluid flow direction, particularly on the FFCV (Fig. 6r). Abundant fine-grained galena is intergrown with bornite and digenite, particularly in samples from medium- and low-pressure wells (Fig. 6n). On the OP and FFCV and in samples collected farther downstream in low-pressure pipes, dense scales with abundant galena (Pb > ~12 wt.%) and chalcopyrite (Cu > ~20 wt.%) show distinctive cooling fractures that are filled with remobilized minerals and silver, similar to that described by Hardardóttir (2011). Discrete grains of electrum (< 1–2 μm) occur with trace chalcopyrite on the FFCV; however, electrum is visible under the microscope only where Au concentrations exceed ~250 ppm.

Late fine-grained covellite alters and coats the sulfides at and immediately after the OP in RN-12 and RN-23 (e.g., Fig. 6q). Downstream from the OP and FFCV, Cu-bearing sulfide abundance decreases in all well types (Fig. 6r). The proportions of all sulfides in most wells decrease relative to silica immediately after the OP and FFCV and often show varying flow directions within the same samples (Fig. 6s). However, the scales from high-pressure well RN-23 still contain significant sphalerite and Cu-bearing sulfides ~32 m downstream (Fig. 6t).

4.1.5. Group V precipitates: separator station and Grey Lagoon

Group V samples are dominated by silica; sulfides (mainly sphalerite) are only present in trace amounts. Scales from the separator station include thin, alternating bands of dark grey or black amorphous silica with traces of disseminated sulfides. Scales from the venthouse are thicker (~3 cm) and composed of similar < 1 mm to 1 cm layers of dark gray to black amorphous silica with traces of sphalerite alternating with nearly pure white amorphous silica layers (see also Hardardóttir, 2011). At the point of discharge into the Grey Lagoon, at atmospheric pressure and < 100 °C, amorphous silica is deposited in soft, unconsolidated layers in the pool (Hardardóttir, 2011).

4.2. Mineral paragenesis

In the majority of scales, a natural paragenetic sequence is difficult to determine because mineral precipitation was artificially induced by changes in pressure and temperature during well management. However, some important relationships are evident. The coarsest sulfide grains formed at high pressures and temperatures at depth in the wells. Crystal aggregates of coarse-grained scales are also commonly observed as clasts or "chips" embedded in later scales, indicative of local rip-up and re-deposition. Some chips are several mm in length, often with rims of high-temperature minerals such as chalcopyrite, and they appear to have broken from the well linings in the fluid flow and re-deposited. In intact scales, complex banding and intergrowths of chalcopyrite and sphalerite, locally with well-defined sharp boundaries are common.

The very fine-grained intergrowths and dendritic texture of Zn-sulfides with Cu- and Cu-Fe-sulfides are likely caused by rapid co-

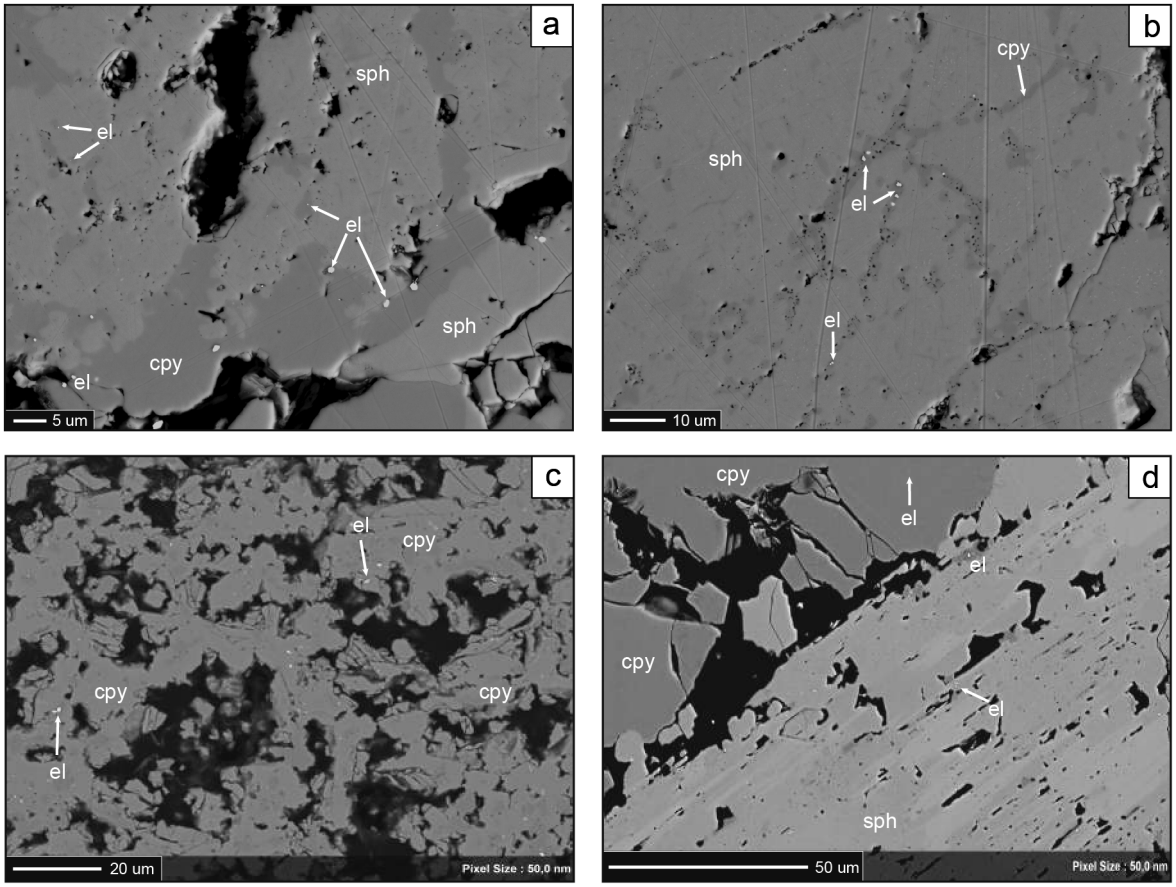

Fig. 7. High-resolution SEM images of electrum (el) associated with chalcopyrite (cpy) and sphalerite (sph) in downhole samples from RN-10. All bright spots in SEM images are electrum. A) Electrum is located mainly within coarse-grained, monomineralic chalcopyrite or at grain boundaries between chalcopyrite. This sample contains the coarsest electrum observed in this study. In Group II scales from the lower boiling zone near 1098 m depth in high-pressure well RN-10. B) Electrum associated with interstitial chalcopyrite in coarse-grained sphalerite in Group II scales from the lower boiling zone near 1098 m depth in high-pressure well RN-10. C) Abundant fine-grained electrum in coarse-grained, monomineralic chalcopyrite in Group II scales from the lower boiling zone near 1098 m depth in high-pressure well RN-10. D) Fine-grained electrum disseminated throughout sieve textured, coarse sphalerite. Electrum is associated with inclusions of chalcopyrite, within the sphalerite, or in voids and fractures. In Group I scales from below the boiling zone near 1832 m depth in high-pressure well RN-10.

precipitation, commonly with chalcopyrite growing epitaxially on skeletal sphalerite or wurtzite. As the Zn-sulfide fully crystallized, blebs of chalcopyrite were preferentially aligned subparallel to crystal edges or laths of the Zn-sulfide and are typical of high degrees of supersaturation and precipitation conditions far from equilibrium (e.g., Craig and Scott, 1976).

In many samples recovered from downhole in well RN-10, Cu- and Cu-Fe-bearing sulfides form an outer coating, indicating higher temperatures just prior to sampling. In strongly banded scales from well RN-10, a repeated sequence is observed of a thin, fine-grained silica layer followed by dendritic sphalerite, with or without chalcopyrite (and other Cu- and Cu-Fe-sulfides), and then a monomineralic, often coarse grained, chalcopyrite band. This suggests repeated cycles of abrupt cooling followed by progressive heating. In the majority of scales containing pyrite (e.g., in RN-10), the pyrite is earlier than chalcopyrite and sphalerite (e.g., Fig. 6p). Clasts of pyrite are either coated by fine-grained chalcopyrite and/or sphalerite and wurtzite, or contain these sulfides (and electrum) as later fracture fill.

Electrum is associated with all of the primary sulfide phases (sphalerite, wurtzite, and chalcopyrite), whereas native Ag and secondary minerals filling fractures (potentially sulfosalts; Hardardóttir, 2011) are coeval with or later than galena.

4.3. Mineral chemistry

Iron contents of sphalerite and wurtzite range from 4.8 to 13.5 mol % FeS (Table B1.1). Sphalerite and wurtzite from Group I scales in RN-10 collected at 1668 m and 1832 m depths (Table 5) have the highest Fe contents (avg. 13.0 mol % FeS in samples from 1668 m and 8.5 mol % FeS in samples from 1832 m). Minor amounts of Cu (average of ~0.5 wt.%) in the sphalerite most likely reflect ultrafine inclusions of chalcopyrite. Sphalerite and wurtzite from Group II and III scales (1098 m and 660 m, respectively, in RN-10: Table 5) contain an average 6.1 mol % FeS (1098 m) and 7.0 mol % FeS (660 m), as well as significant Cu (avg. 1.6 wt.% and 2.2 w.t%, respectively).

Chalcopyrite in Group II and III scales from RN-10 was also analyzed (Table 4). At 660 m, it contains an average of 7.1 wt.% Zn, and less Cu (avg. 30.9 wt.%) and Fe (27.2 wt.%) than stoichiometric chalcopyrite. The compositions likely represent a Cu-Zn-Fe-S intermediate solid-solution close to stoichiometric chalcopyrite, and similar to that reported in surface pipes by Hardardóttir et al. (2010). The unusual Cu-rich pyrrhotite in the upper part of the system may also be a product of an intermediate Fe-Cu-S solid solution or a metastable phase (Hardardóttir et al., 2010). Several analyses of bornite in RN-10, which is very fine-grained and therefore difficult to analyze, indicate a non-

stoichiometric, Ag-rich (avg. 0.52 wt.%) composition (Table 5), very similar to that reported from RN-22 by Hardardóttir et al. (2010). Despite the very high Ag concentrations of the bulk samples, no significant Ag was detected in microprobe analyses of chalcopyrite.

Due to the abundance of ultrafine inclusions in the other minerals, high concentrations of certain trace elements (Ag, Pb, Au) were detected in many of the EPMA analyses (Table B1.1). Analyses of Group II Zn-sulfides indicated the presence of locally significant Ag (avg. 0.14 wt.%), Au (avg. 0.19 wt.%), Pb (avg. 0.11 wt.%), and Cu (avg. 1.6 wt.%). Analyses of pyrite from Group I scales at 1832 m depth also indicated the presence of significant Cu (avg. 1.53 wt.%), Zn, (avg. 0.52 wt.%), Pb (avg. 0.21 wt.%), and Au (avg. 0.08 wt.%), and in pyrite from Group II scales at 1098 m depth significant Pb (avg. 0.12 wt.%) and Au (avg. 0.13 wt.%) (Table 5). Massive magnetite from 660 m in RN-10 contains significant Mn (avg. 0.72 wt.%), Si (avg. 0.58 wt.%), and Cr (avg. 0.16 wt.%) (see Table B1.2 for full dataset).

There is an apparent increase in the Ag content of electrum from nearly pure Au at 2700 m depth to more Ag-rich electrum in Groups II and III (Table 4), to native Ag in Group IV surface pipes. Electrum-bearing samples from RN-10 within the lower boiling zone (Group II: 1098 and 1099 m depth) and below the boiling zone (Group I: 1832 m depth) were analyzed by HR-SEM. Fig. 7 shows examples of electrum at grain boundaries between chalcopyrite and sphalerite (1098 and 1832 m depths) and within fractured sphalerite (1832 m depth). In coarse, clean chalcopyrite, grains of electrum are commonly larger, and in backscatter are brighter, indicating higher Au and lower Ag. Free grains of gold (< 5 μm) in association with chalcopyrite and pyrrhotite were found within sulfide crystals from the downhole apparatus recovered from 2700 m in well RN-17B (Fig. 6g) (Hardardóttir et al., 2013).

4.4. Bulk geochemistry

The major and trace element geochemistry were determined for 129 scale samples from the deep sub-surface through to distal surface pipelines. The downhole variations in the bulk compositions of the scales are illustrated in Figs. 8 and 9.

4.4.1. Major elements

Silica: Bulk SiO_2 concentrations are similar in scales from below and at the onset of boiling (Group I and II: avgs. 17.9 and 16.5 wt.%, respectively) and increase slightly to the surface wellhead and upstream of OP/FFCV (Group III). Beyond the throttle point (Group IV), SiO_2 concentrations increase to a maximum of 84.0 wt.%. The scales in medium-pressure scales contain more SiO_2 (avg. 23.7 wt.%) than those in high-pressure wells (avg. 12.0 wt.%). Group V scales contain on average 65.7 wt.% SiO_2 (Fig. 8). Scales from the venthouse are almost entirely SiO_2 (92.2 wt.%).

Iron: Iron concentrations in all scales are highest downhole at the onset of boiling and decrease to the top of the boiling zone. The variation from the bottoms to tops of the wells are highly dependent on the well pressure. Iron concentrations are highest in the deep scales of RN-17B (28.7 wt.%) and in the lower part of the boiling zone (e.g., Group II scales, avg. 23.9 wt.%; Table 4). Group III scales show a decrease in Fe concentrations (avg. 8.83 wt.%) up to the wellhead. There is a reversal at the OP and FFCV, particularly for medium-pressure wells (Fig. 9), where Group IV scales contain up to 12.9 wt.% Fe. Iron concentrations in Group V scales are the lowest (avg. 3.16 wt.%); however there is still significant Fe in scales at the separator station (avg. 9.08 wt.%). The majority of the Fe in scales is contained in Fe-bearing sulfides such as chalcopyrite, but there is a significant amount of Fe in Fe-silicates from the wall rock, such as amphiboles and pyroxene, and silicates precipitated with the sulfides, such as chlorite (chamosite and corrensite), and clays such as saponite and nontronite (Fig. 10a; Table D1).

Manganese: Manganese shows very similar relative abundances as Fe. It is most abundant downhole and is particularly enriched in RN-22 (up to 0.78 wt.%, averaging 0.18 wt.%) and RN-17B (0.42 wt.%). Group I scales from below the boiling zone in RN-10 have somewhat lower Mn (avg. 0.08 wt.%). Manganese concentrations in scales from the lower boiling zone increase at the onset of boiling, but then are highly variable to the top of the boiling zone, including on the OP and FFCV, in all wells. Concentrations in the high-pressure and medium-pressure wells are similar, but they are lower in the low-pressure wells (Fig. 9). Manganese concentrations increase in Group IV scales downstream from the control valves, and distal Group V scales have the lowest Mn concentrations (avg. 0.13 wt.%). Average concentrations of 0.40 wt.% Mn in scales from the separator station show that there is still significant Mn in the system at the most distal discharge, although absolute concentrations decrease in the Grey Lagoon (to < 0.03 wt.%) owing to dilution by silica. Manganese is present in magnetite but is also positively correlated with Al (and Ga), particularly in low-pressure Group III scales, and therefore likely contained within Al-bearing minerals such as clays (Fig. 10b and 10c; see below).

Copper: Copper concentrations in the sulfide scales increase significantly at the onset of boiling (from Group I to Group II) all the way to the surface (Group III scales) and especially at the FFCV (Group IV: Fig. 8). Copper concentrations in Group I scales average 1.50–1.42 wt.%, respectively, in RN-10 and RN-22, but are low in the deepest scales from 2700 m in RN-17B (0.08 wt.%). Scales in the medium-pressure wells and low-pressure wells are particularly enriched in the upper part of the boiling zone (avg. 6.37 wt.% and 12.0 wt.%, respectively) compared to the sampled material from the high-pressure wells (avg. 3.15 wt.%), probably reflecting the lower temperatures of the low-pressure wells that cause the precipitation of Cu-Fe-sulfides. There is an increase in Cu contents in scales from the high-pressure wells between the wellhead and OP. The highest concentrations of Cu in every well are at the OP and FFCV (Group IV scales: avg. 15.4 wt.%) reaching a maximum of 27.1 wt.% on the FFCV. Copper concentrations decrease downstream, particularly in low-pressure wells, although samples from as much as 32 m downstream locally still contain up to 13.8 wt.% Cu. Distal scales contain significantly less Cu (avg. 0.69 wt.% in Group V).

Zinc: Zinc is the most abundant metal in all scales, especially below the boiling zone (Group I: avg. 27.2 wt.%), decreasing slightly in Group II scales and then increasing again in the upper boiling zone and surface pipelines (Fig. 8). Zinc concentrations in Group I scales reach 51.0 wt.% at 1575 m depth in RN-10 and are somewhat lower in RN-22 (avg. 14.4 wt.%). However, the minor scales from the deepest part of the system (2700 m depth in RN-17B) contain much less Zn (3.14 wt.%). In the boiling zone, Zn concentrations average 17.1 wt.% (Group II scales) to 39.4 wt.% (Group III scales), with the highest concentrations at the wellhead (36.6–40.3 wt.% Zn) and on the upstream side of the FFCV (up to 64.7 wt.% Zn in well RN-28) (Fig. 9). Scales in the high-pressure wells are particularly enriched in Zn in the upper part of the boiling zone (avg. 46.9 wt.%) compared to scales from the medium- (avg. 15.4 wt.%) and low-pressure wells (avg. 24.0 wt.%). Group IV scales from high-pressure wells are still highly enriched in Zn even ~32 m downstream from the OP, with up to 44.9 wt.% Zn. Distal Group V samples contain significantly less Zn (avg. 3.67 wt.%), and no Zn was detected in the silica-rich scales from the venthouse.

Lead: Concentrations of Pb are low in the Group I scales from below the boiling zone and are highest in scales deposited by surface boiling (Fig. 8). Group I scales contain an average of 0.02 wt.% Pb, slightly higher in RN-22 (avg. 0.06 wt.%) than in RN-10 (avg. 0.01 wt.%). The deepest scales from RN-17B contain no detectable Pb. Lead concentrations remain low in the high-temperature boiling zone (avg. < 0.01 wt.% in Group II scales) but sharply increase at the wellhead where scales from medium-pressure wells contain an average of 5.75 wt.% Pb. Scales from the boiling zone of the low-pressure wells contain an average of 9.54 wt.% Pb, whereas scales from the high-pressure wells have an average of only 0.05 wt.%. Lead concentrations decrease sharply downstream of the OP in all well types (Fig. 9); ~32 m downstream in RN-23, the scales contain only 0.64 wt.% Pb. Distal

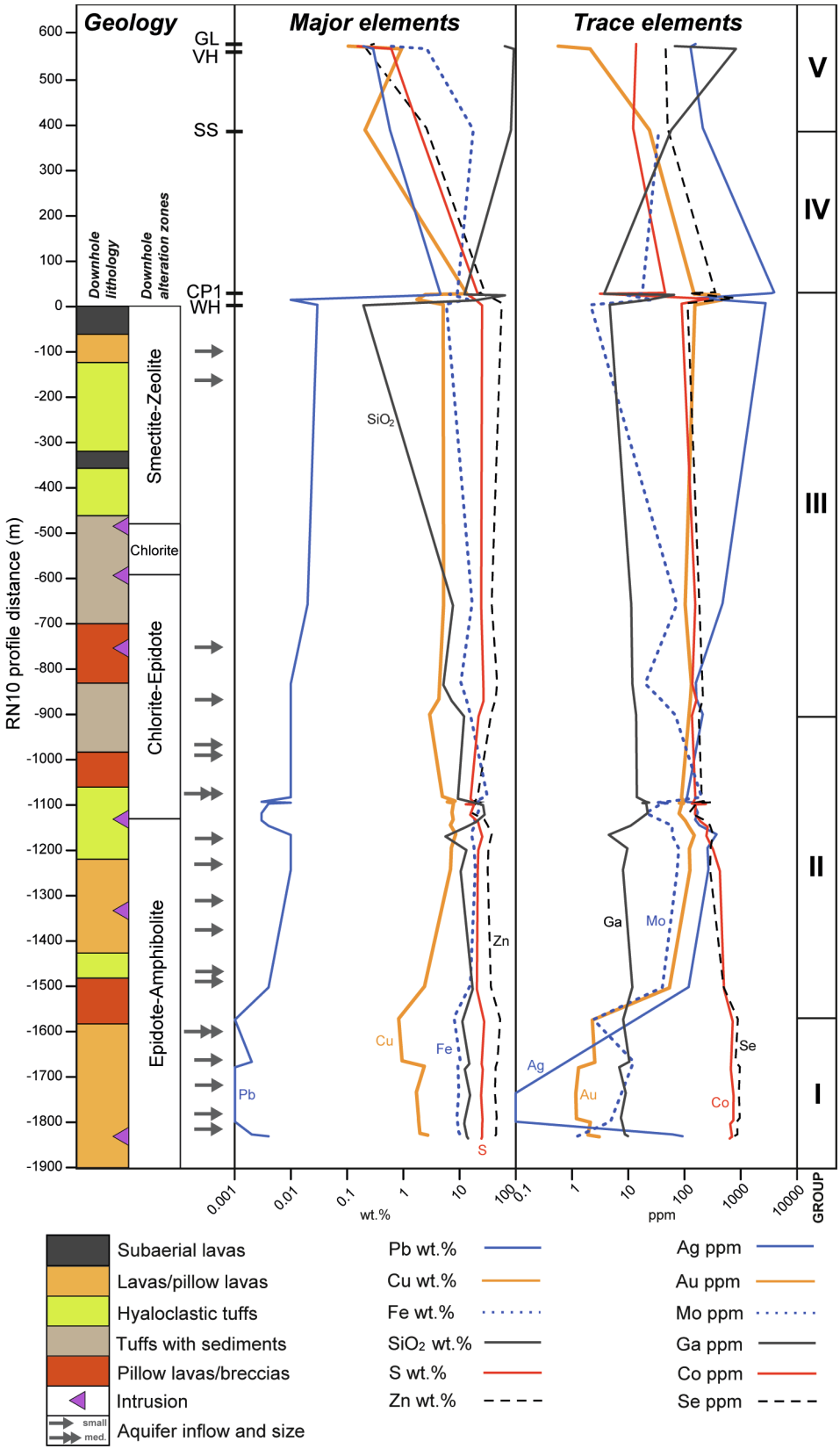

Fig. 8. Profile of selected trace and major element average concentrations in scales from well RN-10 according to scale group. Profile is true vertical distance from the base of sampling to the wellhead and then true horizontal distance from the wellhead to the Grey Lagoon. See text for discussion of the major and trace element behavior. Major and trace elements with comparable behavior and distribution are shown by similar color and line designations. Surface sampling locations are indicated: WH = wellhead, CP1 = OP and FFCV, SS = separator station, VH = venthouse, GL = Grey Lagoon. Downhole lithologies, alteration zones, and aquifer inflow data are from Franzson et al. (2002).

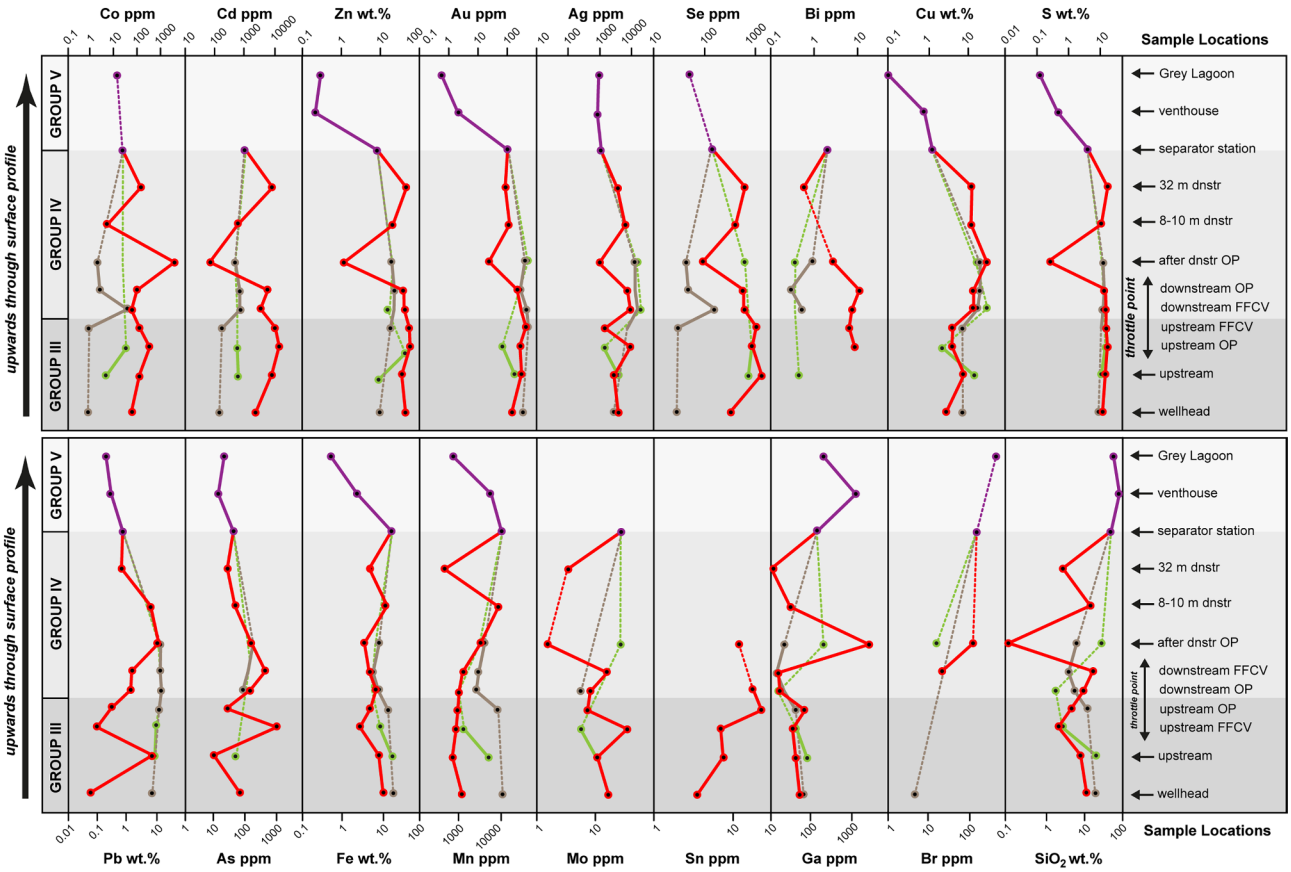

Fig. 9. Downhole profiles (averages) of individual elements by scale group from the wellhead to the Grey Lagoon for high- (red), medium- (brown), and low-pressure (green) wells. Purple segments include the average concentrations of samples from all scale types from the separator station to the Grey Lagoon. Sample locations are indicated on the right hand side panel, and by black circles on the profiles. Profiles are not to scale. Dashed lines linking sites indicate concentrations are below detection limit at intermediate locations. (For interpretation of the references to color in this figure legend, the reader is referred to the web version of this article.)

Group V scales have an average of 0.29 wt.% Pb; lower than in Group IV scales but significantly higher than in Group I and II scales. Lead is below detection in the silica-rich scales from the venthouse.

Sulfur: Bulk sulfide concentrations increase from below the boiling zone, through the lower and upper boiling zones to the surface throttle point (Fig. 8). Group I scales contain an average of 17.0 wt.% S; at the onset of boiling, scales in RN-10 contain less sulfide (e.g., between 1504 m and 1085 m), but Group III scales have high concentrations (avg. 23.8 wt.% S). The most abundant sulfide is deposited upstream of the FFCV in the high-pressure wells (avg. 29.9 wt.% S: Fig. 9). Scales from low- and medium-pressure wells have comparable bulk sulfide contents. Distal Group V scales contain significantly less sulfide (avg. 2.13 wt.%).

4.4.2. Trace metals and metalloids

Gold: Group I scales below the boiling zone are all enriched in Au (avg. 172.5 ppm in scales from RN-22, 66.0 ppm in scales from RN-10, and 40.9 ppm in scales from RN-17B). Gold concentrations increase at the onset of boiling, and in the upper boiling zone Group III scales contain an average of 188.5 ppm Au. The highest Au concentrations downhole are in the high-pressure well RN-22, in which there is an overall increase in Au concentration towards the top of the boiling zone (wellhead). At the wellhead Au is significantly enriched in both medium-pressure (250 ppm Au) and high-pressure scales (avg. 134 ppm Au), but concentrations exceed 400 ppm Au in scales on the upstream side of the OP. Scales on the FFCV in high-pressure wells are particularly enriched (up to 948 ppm Au). Group IV scales are still highly enriched in Au, particularly in medium- and low- pressure wells (up to 421 ppm Au), even ~32 m downstream in RN-23 (82.4 ppm Au in Group IV scales) and in distal Group V scales (average of 58.2 ppm Au).

Silver: Bulk Ag concentrations in the sulfide scales from all wells closely track Au. Silver concentrations increase from below the boiling zone (Group I), through the lower boiling zone (Group II) and in the surface pipelines (Group III: Fig. 8). Group I scales from RN-22 contain an average of 122 ppm Ag, samples from RN-10 contain 66 ppm, and the deepest samples from RN-17B contain 24 ppm. Silver is most enriched in scales near the top of the boiling zone (wellhead and upstream of OP), averaging 6612 ppm and up to 1.77 wt.% on the FFCV. After the OP, Ag concentrations decrease in all well types (Fig. 9), but even ~32 m from the OP in RN-23, Group IV scales still contain 1290 ppm Ag. Group V scales contain an average of 58 ppm Ag. Scales from the venthouse prior to fluid release to Grey Lagoon contain 10 ppm Ag, and the low-temperature precipitates in the Grey Lagoon contain a maximum of 0.15 ppm Ag.

Antimony: Group I scales below the boiling zone in RN-10 contain no Sb, and only trace amounts are found in scales from RN-22 (avg. 2.0 ppm) and RN-17B (1.2 ppm). At the onset of boiling, Sb concentrations increase gradually from the base of the lower boiling zone (avg. 2.71 ppm in Group II scales) to the upper boiling zone (avg. 26.5 ppm in Group III scales). The highest concentrations are found in scales from low-pressure wells, similar to Pb. Scales from the boiling zone in the surface pipes have an average concentration of 17.3 ppm Sb, but the concentrations drop sharply in scales after the FFCV and OP and are below detection at ~32 m downstream. Distal Group V precipitates contain only 1 ppm Sb on average.

Arsenic: Only minor As is present in scales from below the boiling zone (avg. 22 ppm in Group I scales and below detection in RN-10: Table 3) and in the lower boiling zone (avg. 24 ppm in Group II scales).

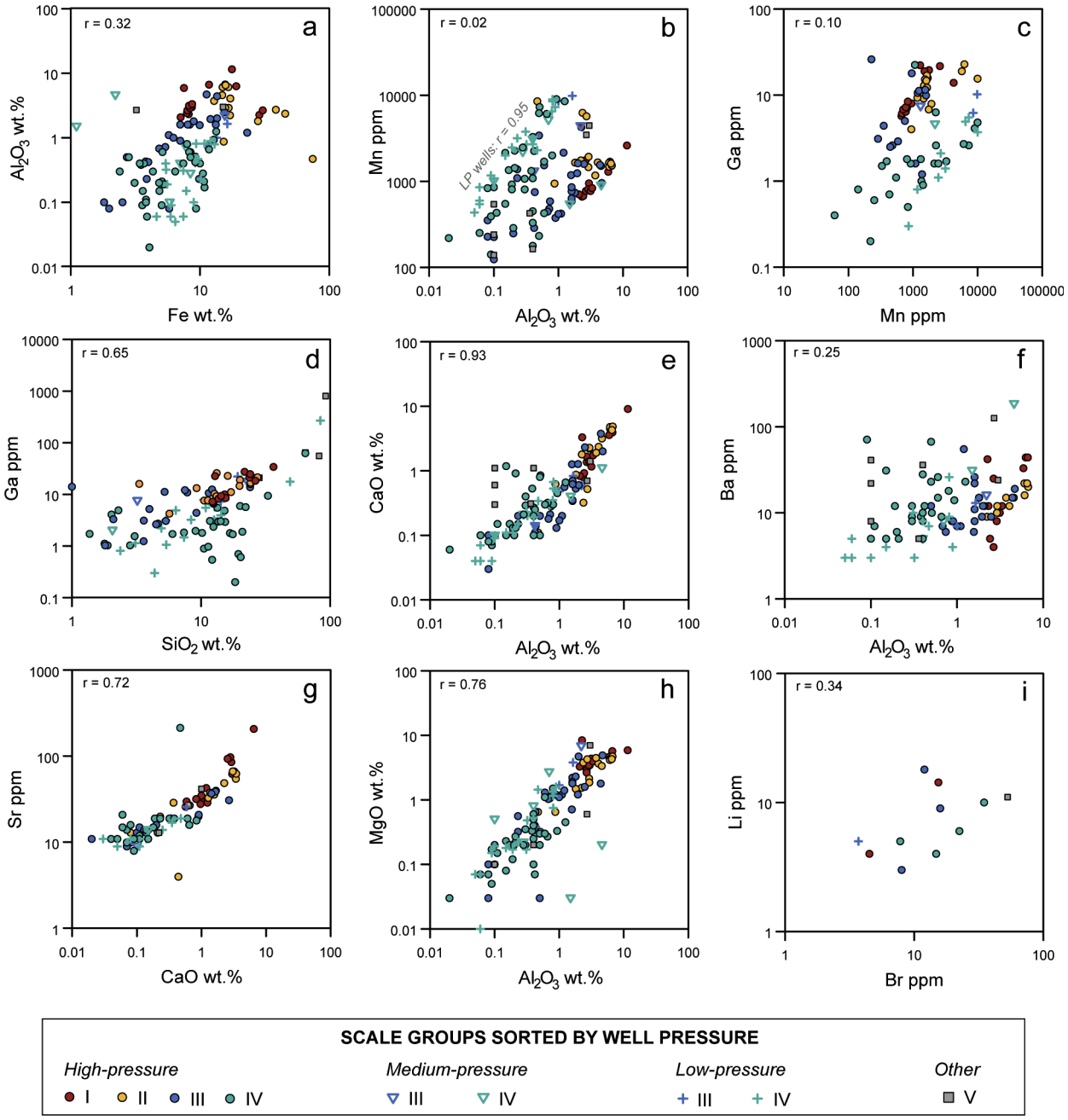

Fig. 10. Bivariate plots of selected non-sulfide trace elements in different scales of the Reykjanes system. All data (except in Fig. 10d) have been normalized to zero SiO_2 to remove the variable effects of dilution. A) Fe versus Al_2O_3 showing a significant positive correlation in all scales. A substantial proportion of Fe in the Reykjanes scales is likely contained within Fe-aluminosilicates. B) A positive correlation of Al_2O_3 versus Mn showing that Mn is primarily contained within Al-bearing minerals (e.g., clays) rather than ore-forming elements, particularly in low-pressure wells (Table 6). C) Mn versus Ga showing a positive correlation indicating that that Ga may be hosted in similar Al-bearing non-sulfide phases to Mn. D) SiO_2 versus Ga showing the significant positive correlation in all scales. Gallium is likely present in Si-bearing phases such as smectite in low-temperature precipitates. E) A positive correlation of Al_2O_3 versus Ca showing that Ca is likely hosted by Ca-bearing aluminosilicates such as smectites, chlorites, amphiboles, and pyroxenes. F) Al_2O_3 versus MgO showing a positive correlation indicating that that Al and Mg occur together in phases such as chlorite, smectites, pyroxene, amphiboles, and minor spinel. G) A positive correlation of Al_2O_3 versus Ba showing that Ba is preferentially hosted by Al-bearing minerals, likely aluminosilicates (see Si versus Al in Table 6). H) CaO versus Sr showing a positive correlation and that Sr likely substitutes for Ca in Ca-bearing minerals. I) A positive correlation of Br versus Li showing that these two elements represent a remnant brine phase. Abbreviations: LP = low-pressure wells, Group I scales = below boiling zone, Group II scales = lower boiling zone, Group III scales = upper boiling zone, Group IV scales = surface boiling zone, Group V scales = distal, lower-temperature scales.

Arsenic concentrations are somewhat higher in Group II scales from RN-22 (avg. 62 ppm) compared to RN-10. The concentrations increase upwards through the boiling zone, similar to Sb, reaching an average of 279 ppm in Group III scales and 3030 ppm on the FFCV in the high-pressure wells. Group IV scales from the high- and medium-pressure wells also contain significant As (avg. 254 ppm), but scales from the low-pressure wells, even on the FFCV, contain no detectable As. At ~32 m downstream, scales contain no more than 26 ppm As, and the average concentration in Group V scales is only 6.5 ppm.

Mercury: Mercury was not detected in any Group I or Group II scales. However, Hg concentrations reach 34 ppm at 160 m depth in the upper boiling zone (Group III scales). Scales on the downstream side of the OP

and FFCV (Group IV) also contain 14–32 ppm Hg. Mercury reaches a maximum of 46 ppm after the OP in the medium-pressure well RN-24 and tracks Cu, Au, and Se in the surface pipes. No Hg was detected in distal Group V scales.

Cadmium: Below the boiling zone, Cd concentrations in the Group I scales are generally high, reflecting the abundance of Zn-sulfide. Within the boiling zone, the concentrations are variable, decreasing slightly in Group II scales and then increasing again in the upper boiling zone and surface pipelines, tracking Zn (Fig. 8). The concentrations in Group I scales average 0.42 wt.% (avg. 5642 ppm in scales from RN-22 and 4127 ppm in RN-10). Concentrations of Cd in scales from the upper boiling zone are similarly high (avg. 4578 ppm in Group III scales), especially in the high- and medium-pressure wells and immediately upstream of the FFCV and OP. Cadmium concentrations in the surface boiling zone are lower (avg. 1853 ppm) and decrease rapidly right after the OP (Fig. 9), but 32 m downstream, Group IV scales still contain up to 5220 ppm. Cadmium decreases in Group V scales but is still significant in scales from the separator station (avg. 271 ppm).

Tin: The highest concentrations of Sn (up to 77.7 ppm) were found in Group II scales within below the boiling zone. Tin concentrations decrease to the top of the boiling zone and are sporadic in the surface boiling zone. Group I scales from RN-17B and RN-22 contain an average of 17.7 ppm and 13.0 ppm, respectively. Concentrations of Sn from scales in the boiling zone (Group II) are uniformly ~17 ppm. Tin increases slightly near the top of the boiling zone in high-pressure wells (max. 30.3 ppm), but it is below detection in medium-pressure wells. No Sn was detected in the surface boiling zone or distal Group V scales and appears to track the abundance of chalcopyrite in the system where it is most likely hosted.

Bismuth: Concentrations of Bi are low in all samples. Bismuth is present only in trace quantities in Group I scales from RN-10 (avg. 2.0 ppm) and RN-17B (0.2 ppm), and is not detected in any scales from the lower boiling zone. At the top of the boiling zone the scales in low-pressure wells contain only 0.4 ppm; somewhat higher concentrations are found in scales from the high-pressure wells on the OP and FFCV (avg. 14 and 9.4 ppm, respectively). Group V scales from the separator station contain only 2 ppm Bi on average, and Bi was not detected in precipitates from the Grey Lagoon.

Cobalt: The highest Co concentrations are in Group I scales from RN-10 (up to 622 ppm). Concentrations of Co are high in all scales from below the boiling zone (avg. 392 ppm in Group I) but decrease at the onset of boiling to an average of 170 ppm in Group II scales and 151 ppm in Group III scales (Fig. 8). Cobalt concentrations increase again in scales immediately upstream of the wellhead, especially in high-pressure wells (up to 449 ppm in RN-23). The concentrations are 1–2 orders of magnitude higher in the high-pressure wells compared to the medium- and low-pressure wells (Fig. 9). The concentrations drop after the FFCV and OP to an average of 60 ppm in Group IV scales. Thereafter, Co contents decrease rapidly through the surface pipes, and only trace Co is present in Group V scales from the separator station (avg. 12.2 ppm), Grey Lagoon (avg. 2.0 ppm) and venthouse (below detection). Cobalt is associated with all sulfide phases, but appears to most closely track Fe and Cu abundance downhole.

Nickel: High concentrations of Ni are found in scales from below the boiling zone (avg. 187 ppm in Group I scales), with the deepest scales at 2700 m depth in RN-17B containing 456 ppm. Nickel concentrations increase to an average of 231 ppm in Group II scales at the onset of boiling and then decrease towards the top of the boiling zone (avg. 48 ppm in Group III scales). Scales from the high-pressure wells contain an average of 80 ppm Ni in Group III scales, but no Ni was detected in the Group III scales from the medium-pressure wells and only minor Ni was found in the low-pressure wells. Scales on the FFCV and at the OP contain only trace Ni, although higher Ni was found in scales further downstream in high-pressure wells (avg. 50 ppm). Nickel is below detection in Group V scales.

Selenium: High concentrations of Se are found in scales from below the boiling zone (avg. 563 ppm in Group I scales), with scales from RN-10 containing an average of 763 ppm, although the scales from 2700 m depth in RN-17B contain only 17.8 ppm Se. Selenium concentrations decrease to an average of 204 ppm in Group II scales at the onset of boiling and then increase again towards the top of the boiling zone (avg. 725 ppm in Group III scales: Fig. 9). Group III scales from RN-22, between 669 m and 141 m, are significantly enriched in Se (avg. 1144 ppm), reaching a maximum of 1600 ppm and then decreasing to the surface wellhead. Scales from the high-pressure wells have generally higher concentrations of Se than scales from medium-pressure wells. Selenium concentrations in scales from the surface boiling zone (avg. 527 ppm in Group IV scales) are comparable to those in Group I scales below the boiling zone. Scales on the FFCV average 865 ppm Se in the medium- and low-pressure wells, and then the concentrations drop sharply right after the OP. However, Se concentrations in the high-pressure wells still reach 497 ppm ~32 m downstream. There is also significant Se in scales from the distal parts of the system (avg. 75.5 ppm in Group V scales at the separator station and avg. 20 ppm in Grey Lagoon). No Se was detected in scales from the venthouse.

Tellurium: Scales that formed below the boiling zone have high concentrations of Te (avg. 61 ppm in Group I scales), with the highest concentrations in scales from RN-10 (up to 79 ppm Te). However, the deepest scale sample from RN-17B contains only trace Te (0.4 ppm). Low concentrations were found in scales formed at the onset of boiling (avg. 13.8 ppm in Group II scales), and then concentrations increase towards the top of the boiling zone (avg. 58 ppm in Group III scales from medium-pressure wells). Scales on the OP in medium-pressure wells contain a maximum of 63 ppm Te. Tellurium was not detected in any Group III or Group IV scales from low-pressure wells. Tellurium concentrations in scales formed by boiling in the surface pipes are 20–30 ppm, and concentrations decrease downstream rapidly away from the OP. Tellurium was not detected in Group V scales from the Grey Lagoon or venthouse; however, a single sample with 67 ppm Te was collected from the separator station.

Molybdenum: Group I scales contain an average of 38.5 ppm Mo, with up to 69.9 ppm in scales from 2700 m depth in RN-17B, although Group I scales from RN-10 have low Mo (avg. 4.3 ppm). Molybdenum concentrations increase slightly at the onset of boiling in Group II scales, with average concentrations of 62.8 ppm, and then decreases to the top of the upper boiling zone in both high- and low- pressure scales. Mo was not detected in the upper boiling zone of medium-pressure wells, and only traces of Mo are present ~32 m downstream of the OP. However, Group V scales from the separator station contain an average of 22.3 ppm Mo.

Gallium: Group I scales below the boiling zone contain an average of 12 ppm Ga, with 13.9 ppm in RN-17B and 19.6 ppm in RN-22. Gallium concentrations increase in Group II scales from the bottom (avg. 12.9 ppm) to the top of the boiling zone (up to 26 ppm) and then decrease in the surface boiling zone. Gallium concentrations are generally higher in scales from low-pressure wells. Group V scales are notably enriched in Ga, and samples from the venthouse are most enriched (63 ppm). Samples from the separator station (avg. 12.6 ppm) and Grey Lagoon (avg. 23.2 ppm) also contain significant Ga. Gallium is not strongly correlated with the sulfide content of the scales and the positive correlation of Ga and Al indicates that Ga is likely hosted in Al-bearing non-sulfide phases such as clays (Fig. 10d), behavior which is similar to Mn (Fig. 10c).

Vanadium: Group I scales below the boiling zone contain significant amounts of V (avg. 191 ppm), notably in scales from RN-22 (avg. 349 ppm). At the onset of boiling, the concentrations in Group II scales are 98 ppm, on average; they vary in the lower boiling zone but then increase in the upper boiling zone to an average of 208 ppm V. Concentrations of V in scales from the surface boiling zone average 35.9 ppm and are higher, on average, in the medium- and low-pressure wells. At 32 m downstream there is still significant V in Group IV scales (119 ppm), but Group V scales from the separator station contain only

21.5 ppm V. Samples from the Grey Lagoon contain an average of 11 ppm, and no V was detected in samples from the venthouse.

Chromium: Chromium is most abundant in scales from below the onset of boiling (Group I scales) and decreases to the top of the boiling zone. Chromium concentrations increase again in the distal Group V scales. Group I scales contain an average of 435 ppm Cr, with 754 ppm in scales from RN-17B and an average of 371 ppm in scales from RN-22, although the scales from RN-10 contain no detectable Cr. All Group II scales contain an average of 281 ppm Cr, with an average of 699 ppm in scales from RN-22 and 176 ppm in RN-10. Scales in the upper boiling zone also contain high Cr (avg. 115 ppm) up to the wellhead. Chromium concentrations then increase again downstream in scales from all well types, especially after the OP in low-pressure wells (avg. 770 ppm) and in Group V scales from the separator station (avg. 333 ppm). Samples from the Grey Lagoon contain 95.5 ppm Cr, but no Cr was detected in the scales from the venthouse.

Tungsten: Concentrations of W are low in most scales. Group I scales below the boiling zone contain an average of 7.1 ppm W. Group II scales from the onset of boiling contain notable W, averaging 86 ppm (excluding one sample: see below). Concentrations in scales from the upper boiling zone (Group III) average less than 5 ppm, and the concentrations decrease sharply to the wellheads. Limited amounts of W (max 11.1 ppm) were found in scales from the surface pipes in high- and low-pressure wells, including on the FFCV, and no W was detected in medium- pressure wells. Samples from the venthouse contain up to 8 ppm W, but W is below detection in other Group V scales.

Germanium, Tl, In, U, and Th are present in trace quantities in all scales (Tables 4 and 5). Samples from the upper boiling zone contain up to 15 ppm Ge (at the wellhead of RN-11) and 1.4 ppm Tl (in shallow downhole scales from RN-22). Scales from the surface boiling zone contain up to 1.3 ppm In, 0.7 ppm U, and 0.7 ppm Th.

4.4.3. Other elements

Calcium: Scales from below the boiling zone contain an average of 2.5 wt.% Ca, with the highest concentrations in scales from RN-22 (avg. 4.4 wt.%). Most of the calcium is likely present in Al-bearing smectites such as saponite, chlorites (e.g., corrensite), actinolite and epidote (Fig. 10e). Calcium concentrations in the scales from the boiling zone are variable (0.02–4.8 wt.%); here, a higher proportion of Ca is likely contained in carbonate alteration minerals (Table 2). However, higher concentrations are found in the scales on the OP and FFCV, and there is significant Ca in distal Group V precipitates (avg. 0.79 wt.%), particularly at the separator station (1.05 wt.% Ca). As carbonates were not identified in these samples, the Ca is most likely present in clays (e.g., Hardardóttir, 2011).

Barium: Group 1 scales in RN-17B contain 42 ppm Ba; in RN-22 the average concentration is 34 ppm and somewhat lower in RN-10 (9 ppm). Similar concentrations of Ba are found in scales from the lower boiling zone, decreasing to the surface wellhead and in the surface pipes. Barium concentrations average 55 ppm in scales on the FFCV and OP but are generally lower in the low-pressure wells. The highest concentrations of Ba are in scales from distal Group V (avg. 37 ppm), with a maximum of 75 ppm in scales from the separator station. Barium is potentially hosted by Ba-bearing minerals such as barite and adularia similar to that observed by Libbey and Williams-Jones (2016c). This is supported by a strong positive correlation between Ba and Al in Group I and Group II scales (Fig. 10f), even though barite or adularia concentrations were potentially not high enough to be detected during XRD analysis.

Strontium: Concentrations of Sr are highest in Group I and II scales (max. 328.5 ppm) and decrease in Group III scales (avg. 16.2 ppm) where concentrations are uniformly low up to the Group IV scales (avg. 16.5 ppm). Strontium concentrations increase slightly in distal Group V scales (avg. 27.4 ppm), particularly from the venthouse (max. 189.4 ppm). Strontium is very strongly correlated with Ca and likely substitutes for Ca in minerals such as calcite or other Ca-bearing silicate phases confirmed by XRD data (Fig. 10g; Table D1).

Aluminum (Al_2O_3): Aluminum is most abundant in Group I scales (avg. 4.08 wt.%), decreasing only slightly in Group II scales at the onset of boiling (avg. 3.60 wt.%). Concentrations decrease further in Group III scales (avg. 1.24 wt.%) and then drop significantly in Group IV scales (avg. 0.42 wt.%). One anomalous sample from the venthouse contains 7.90 wt.% Al_2O_3. The XRD analyses confirm that Al_2O_3 is mainly present in aluminosilicate minerals and clays (Table D1).

Magnesium (MgO): Similar to Al, Group I scales contain the most Mg (avg. 4.33 wt.%) and concentrations decrease only slightly above the onset of boiling (avg. 3.02 wt.% in Group II scales). Magnesium contents are lower in Group III scales (avg. 1.52 wt.%) and decrease significantly across the OP and FFCV (avg. 0.40 wt.% in Group IV scales). The venthouse sample contains 9.73 wt.% MgO. Magnesium is mostly present in Mg-rich silicate minerals such as enstatite and diopside (as confirmed by XRD), and clay minerals in distal surface scales (Fig. 10h).

Bromine: The sulfide scales in the lower part of the wells (both above boiling onset and below the boiling zone) contain traces of Br (< 15 ppm in all samples), possibly from evaporated brine. Scales on the OP in the high-pressure wells contain 22 ppm Br on average; distal Group V scales contain 159 ppm, and samples from the Grey Lagoon contain up to 429 ppm, following the brine into the discharge pool.

Lithium: Lithium was detected in only three Group I scales (max. 19.5 ppm) and was not detected in Group III scales until relatively shallow depths between 141 m and 669 m in RN-22 (max. 18 ppm). The highest measured Li was 27.2 ppm, in a Group III scale from RN-10. A small cluster of data above detection occurs in Group IV scales on the downstream side of the OP in the high-pressure well RN-22. One sample from the venthouse contained 15.3 ppm. A weak correlation with Br in the same samples suggests that most of the Li is related to evaporated brine (e.g., Fig. 10i).

Fluorine: All samples analyzed for fluorine were below the minimum limit of detection (< 0.01 wt.%).

Boron: Boron was not detected in Group I scales and only one analysis was above detection (40 ppm) in Group II scales from 1168 m depth in RN-10. Boron was detected in Group III scales from RN-22 at 669 m, 449 m, 350 m, and 270 m depths (max 30 ppm). The highest measured B was 100 ppm in an upstream scale from the high-pressure well RN-10. Two downstream Group IV scales from RN-10 contained 40 ppm B, all other scale were below detection. Boron was above detection limit at 30 ppm in only one Group V sample from the Grey Lagoon. Likely due to scarcity of samples above detection limits, B has no obvious correlations with any other element.

Rare Earth Elements: Total REE concentrations are highest in Group I and Group II scales, decreasing in Group III (Table 4). The Group IV scales are slightly enriched in HREE (e.g., Yb, Lu), but all values are low and close to detection limits. Group V scales are depleted in REE compared to all other samples; all but La, Ce, Nd, and Dy are below detection. Fig. 11 shows REE plot profiles (chondrite-normalized) for each type of scale. Overall REE concentrations are extremely low and the profiles irregular because many elements are close to the detection limit; however, the weak negative Ce anomaly and positive Eu anomaly in some of the scales are similar to chimney samples from seafloor hydrothermal systems (Fig. 11). Fowler et al. (2019) showed that REE concentrations in boiled hydrothermal fluids from the Reykjanes geothermal system are indeed lower than those in any high-temperature (> 240 °C) submarine hydrothermal fluid encountered thus far, and appear to have a similar weak negative Ce anomaly and positive Eu anomaly similar to the chondrite-normalized bulk geochemical data in this study.

5. Discussion

Downhole scales from the high-temperature Reykjanes geothermal system have been analyzed for the first time in this study, including samples from below the boiling zone. The scales were collected during

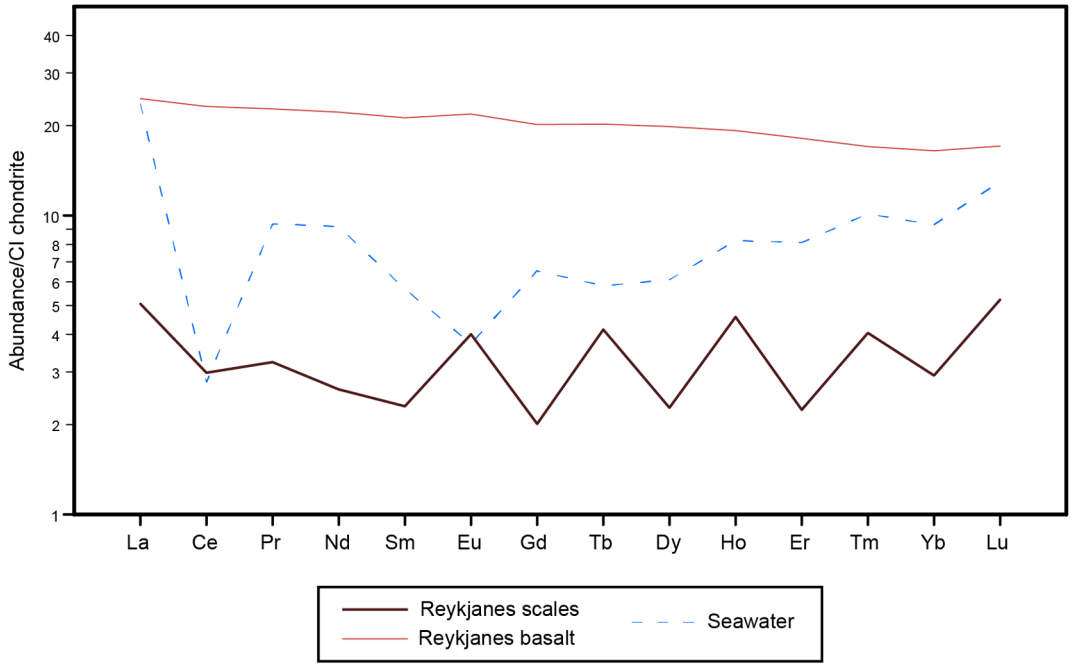

Fig. 11. Chondrite-normalized rare earth element (REE) plot for average scale REE contents across the Reykjanes geothermal system. The scale profile is fairly flat; however a slight negative Ce anomaly positive Eu anomaly resemble those of seawater-dominated submarine hydrothermal systems. Chondrite-normalized data for seawater (Li et al., 1991), and Reykjanes basalt are also presented for comparison. The average REE composition of Reykjanes basalt (n = 34) was calculated from data held in the GEOROC database (https://georoc.mpch-mainz.gwdg.de).

routine maintenance over several years. Deep downhole samples from RN-22 have good depth control determined directly from the retrieved well liner, but do not form a continuous downhole profile. Scales from RN-10 were collected in situ, and provide a more continuous profile with depth.

The distribution of the major minerals can be calculated from the mineral compositions and the bulk geochemistry. Table 6 lists the abundances for the sulfide fraction only (plus magnetite), normalized to zero SiO_2 to remove effects of variable dilution. For this calculation, all Pb was assumed to be in galena and all Zn equally distributed between sphalerite and wurtzite. Iron and Cu were attributed first to chalcopyrite, then bornite, and then the Cu-bearing sulfides (digenite and covellite) until all Cu was consumed. A portion of the remaining Fe and S was then assigned to Zn-sulfides, taking into account the Fe contents from the microprobe analyses (Table B1.1). The remaining Fe balance was assigned to pyrite, pyrrhotite and magnetite based on relative abundances estimated from petrography. The Zn-sulfides (sphalerite and wurtzite, based on petrography) account for 60–70 wt.% of the total sulfide from below the boiling zone to the surface (Table 6). Chalcopyrite accounts for ~20 wt.% in the deep scales and lowermost boiling zone, whereas the sulfides in the upper part of the system contain roughly equal amounts of chalcopyrite and bornite, by weight. Covellite and digenite account for < 5 wt.% of the sulfides in the upper part of the boiling zone, and galena about 6 wt.%.

The compositions of the scales can be divided into two main groups: those enriched in elements deposited at high pressures and temperatures at depth in the wells (Fe, Mn, Zn, Cd, Cu, Co, Ni, Sn, Se, Te, V, Ni, Mo, W), and those enriched in elements deposited at lower temperatures and pressures in the surface pipes (Pb, Ag, Sb, Bi, As, Hg, Ga). Consistent enrichments and depletions of the trace elements, according to temperature-dependent solubilities, are similar to those observed in seafloor chimneys and in ancient volcanogenic massive sulfide deposits (Fig. 12). Scales formed at the highest temperatures below the boiling zone are particularly enriched in Fe, Mn, Co, and Ni, as well as Zn, Cd, and Sn. The latter are also highly enriched in scales throughout the boiling zone and on the FFCV and OP. Copper, Se, and Te are mostly enriched in scales from the lower (higher-temperature) part of the boiling zone, but also where flashing has been induced in the surface pipes at the FFCV. Lead, Ag, Sb, (± Bi) are mostly enriched in the upper (lower-temperature) part of the boiling zone and immediately downstream of the FFCV. Arsenic and Hg are enriched in scales even farther downstream. Other trace elements, such as Mo, Ga, V, and Cr are enriched in the deepest scales and also in silica-rich precipitates in the surface pipes, but are not present in abundance in the boiling zone. This behavior presumably reflects different aqueous complexing of these elements at different temperatures and precipitation in different mineral phases in different parts of the system (e.g., sulfides and oxides at depth; clays and other silicates in the downstream precipitates). Scales at depth and in the high-pressure wells have low silica contents compared to the surface pipes, owing to the high temperatures. Silica deposition occurs mainly in the surface boiling zone and especially where the fluids have cooled conductively in the surface pipelines. The presence of amorphous silica even prior to boiling is consistent with the higher pH of the Reykjanes fluids compared to MOR vents (lower pH in MOR systems has been proposed to inhibit kinetics of silica precipitation, e.g., Fournier, 1985 and discussed in Tivey et al., 1999).

Brecciated samples indicate the possibility of clastic transport in the wells; however, the consistent downhole enrichments and depletions argue strongly against random contamination of the scales by remobilized material, or electrostatic scavenging of metals by the reducing steel liner and casing (McKibbon et al., 1990), although we have only analyzed scale material that is uncontaminated by well liners. For almost all samples, contamination from fragments of the steel pipes and drilling equipment also can be ruled out. Fowler and Zierenberg (2016) suggested that drill cuttings in well RN-17B were contaminated by Cu, Ni, Ta, and Nb from drilling equipment (e.g., alloys in Cu-Ni-rich non-magnetic drill collars, and Na and Ta from worn drill bits). In the absence of magnetite or other spinels in drill cuttings, they also attributed high Cr concentrations to Cr-rich alloys commonly used in drill bits, stabilizers, and drill collars. However, we found no consistent correlation between Cr, Cu, Ni, Ta, or Nb in the analyzed scales. One likely reason is that most of the scales in this study were removed from the

Table 6
Calculated normative abundances of principal mineral phases in the sulfide fraction from Reykjanes geothermal scaling.

Mineral and element composition		Group I		Group II		Group III		Group IV^		Group V	
		Composition (wt.%)	Abundance (vol.%)	Composition (wt.%)	Abundance (vol.%)	Composition (wt.%)	Abundance (vol.%)	Composition (wt.%)	Abundance (vol.%)	Composition (wt.%)	Abundance (vol.%)
Zn-sulfides	Zn	60.97	65	62.73	61	59.45	65	64.88	71	*64.06*	2
	Fe	4.87		3.53		3.69		3.74		*2.88*	
	S	33.81		33.47		32.54		31.49		*33.06*	
Chalcopyrite	Cu	33.66	18	34.38	23	30.90	10	31.54	10	–	–
	Fe	30.94		30.63		*27.16*		30.35		–	
	S_2	35.27		35.08		33.70		31.49		–	
Bornite	Cu_5	*63.31*	10	54.92	12	^56.16	16	63.76	8	–	–
	Fe	*11.13*		14.57		^13.77		8.66		–	
	S_4	*25.56*		29.69		^26.77		23.60		–	
Digenite	Cu	*78.10*	1	*78.10*	1	*78.10*	3	71.11	3	–	–
	S	*21.90*		*21.90*		*21.90*		22.67		–	
Covellite	Cu	*66.46*	0.5	*66.46*	1	*66.46*	0.5	66.91	2	–	–
	S	*33.54*		*33.54*		*33.54*		28.33		–	
Pb-sulfides	Pb	*86.60*	3	*86.60*	0	*86.60*	0.5	78.39	6	–	–
(galena)	S	*13.40*		*13.40*		*13.40*		13.57		–	
Pyrite	Fe	45.07	0.5	47.75	< 0.5	^45.83	< 0.5	*46.55*	< 0.5	–	–
	S_2	52.11		54.04		^51.89		*53.45*		–	
Pyrrhotite	Fe	*62.33*	< 0.5	–	–	^62.78	< 0.5	–	–	–	–
	S	*37.67*		–		^24.00		–		–	
Magnetite	Fe_2	*72.36*	2	*72.36*	2	72.24	5	–	–	–	–
	O_4	*27.64*		–		–		–		–	

Calculated normative abundances of the principal mineral phases in scales from the Reykjanes geothermal field. Normative calculations were performed for each scale group rather than combining all samples over the entire profile. Data was normalized to zero SiO_2 to remove effects of dilution and this table represents the normative mineralogy of the sulfide fraction (plus magnetite) only. For the purposes of this calculation, all Pb was assumed to be in galena and all Zn were assumed to be in Zn-sulfides (sphalerite and the high-temperature sphalerite polymorph wurtzite). All Cu was assumed to be in the Cu-sulfides of chalcopyrite, bornite, and covellite and Cu was apportioned according to relative mineralogical abundances estimated from petrography. Compositions in regular type are from electron microprobe analyses (this study), data in italics denotes that stoichiometric compositions were used, ^ denotes electron microprobe data from Hardardóttir et al. (2010), and '–' indicates this mineral was not present in a specific scale group. All Pb was assigned to galena and once all Pb was consumed, the remaining S, plus Fe and Cu were attributed first to chalcopyrite, then bornite, then covellite until all Cu was consumed. Using the average concentration of Fe and Zn measured in Zn-sulfides, the remaining Fe and S was then apportioned to Zn-sulfides until all Zn was consumed. The remaining Fe and S were then assigned to pyrite, pyrrhotite and magnetite respectively. Group I scales = below boiling zone, Group II scales = lower boiling zone, Group III scales = upper boiling zone, Group IV scales = surface boiling zone, Group V scales = distal, lower-temperature scales.

pipes without cutting, whereas the wall rock samples described by Fowler and Zierenberg (2016) were obtained by drilling. An exception may be the high Cr in some scale samples from RN-10, which were removed by a rotary drilling method used to clean the well. However, metal geothermal pipe shards present in some of our samples were removed during sample preparation using a strong magnet, and there are significant amounts of naturally occurring magnetite, minor rutile, and trace spinel in the samples that can account for all or most of the Cr and Ti (Table 2). Niobium and tantalum were not detected where Cr is high, ruling out the contamination suggested by Fowler and Zierenberg (2016), and Cr is positively correlated with other elements that show a strong temperature dependence in the wells (e.g., Fe, Ni, Sn, Mo, Co, Mn, Cd; Fig. 13a-c). Several samples that do contain elevated W, Nb and Ta (scales from 1245 m in RN-10 with 9.6 ppm Nb, 212 ppm Ta, and 2700 ppm W) do appear to have been contaminated by pipe shards (Fig. 13d). These elements were removed from the dataset for this sample and for four other samples from RN-10. Importantly, scales from RN-17B were not collected from the linings of the wells but rather are scales precipitated directly from the geothermal fluid onto the housing of a downhole experiment, and were then carefully removed in the laboratory. These scales contain magnetite and high Ni, Mo, Mn, Sn, W, and Cr, but low Ti and no Nb or Ta.

5.1. Trace metal associations

Inter-element plots of selected metals and metalloids are shown in Fig. 14, and the Pearson correlation coefficients for element pairs listed in Table 7. All element abundances are strongly influenced by dilution of the sulfide component by SiO_2, therefore data have been normalized to zero SiO_2 to eliminate this effect.

Zinc concentrations are strongly correlated with elements commonly incorporated in Zn-sulfides (Cd, Se: e.g., Fig. 14a) as observed in SMS deposits (e.g., Monecke et al., 2016). The Zn:Cd ratio of ~100:1 is consistent with a uniformly high Cd concentration in sphalerite of 0.61 wt.%. Selenium has a robust positive correlation with Zn in the majority of scales reflecting primary incorporation into sphalerite (Fig. 14b). Positive correlations of Cu, Zn, Se and the prevalence of Zn-sulfide mineralization at high temperature has previously been hypothesized to in part reflect relatively high pH of higher temperature vent fluids versus most MOR vent fluids (e.g., Kristall et al., 2011).

Selenium is strongly correlated with Fe and Cd in downhole Group I and II scales, reflecting deposition in high-temperature Fe-rich sphalerite and wurtzite. Selenium is also positively correlated with Cu and Hg in Group IV scales (Fig. 15a and b), and this may reflect the similar behavior of Se, Cu, and Hg as minor volatile species in the hydrothermal fluids (e.g., Monecke et al., 2016). A weak positive correlation of Se with Pb in low-pressure Group IV scales (Fig. 15c), likely reflects Se incorporation into Se-bearing galena or trace clausthalite (PbSe) in surface pipe scaling (e.g., Hardardóttir, 2011; Grant et al., 2015).

Copper does not correlate with Fe, except in samples where only one Cu-(Fe)-sulfide dominates, as in the bornite-rich scales (Fig. 14c). Copper correlates well with Zn in scales from low-pressure wells and from the upper (i.e., lower-temperature) boiling zones, but it does not correlate with elements such as Te or Co, as in many SMS deposits. Instead, in many scales, Cu correlates most strongly with Ag (e.g., Hardardóttir et al., 2010). Cobalt correlates positively with Fe, Zn, and Cd in all scales (e.g., Fig. 14d), and is particularly enriched in Group I scales below the boiling zone (Fig. 16a). Cobalt and Se are positively

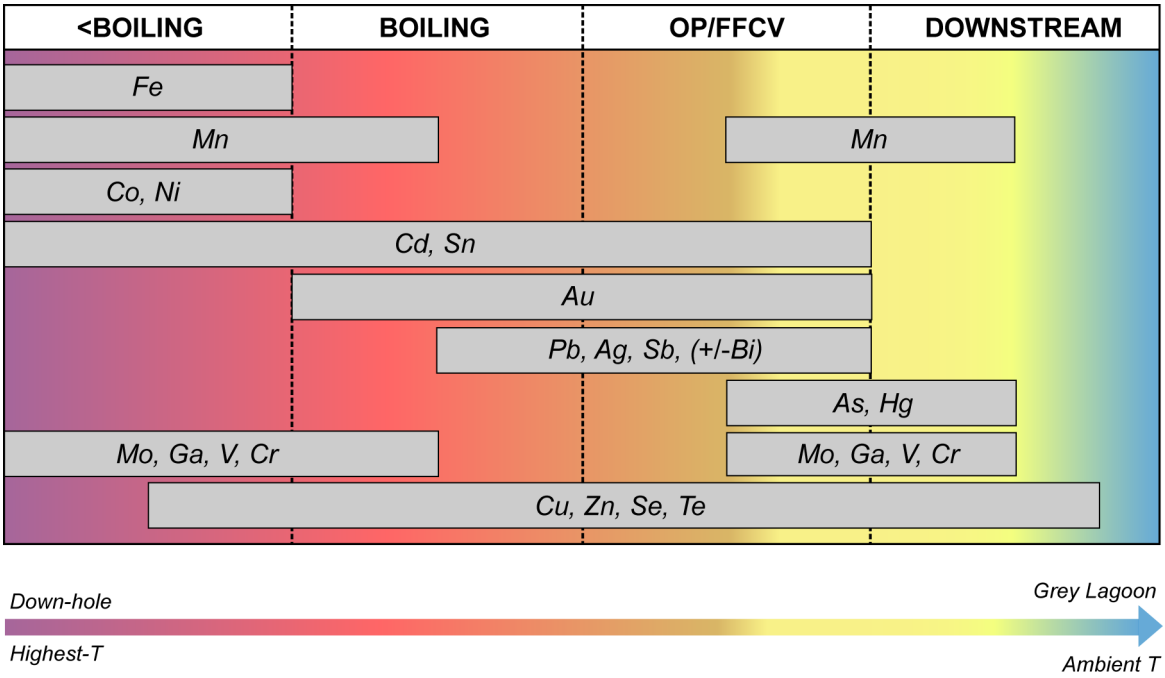

Fig. 12. A summary of the consistent enrichments and depletions in sulfide pipeline scaling from the Reykjanes geothermal field. Trace and major elements follow temperature-dependent patterns consistent with actively-forming and ancient seafloor massive sulfide deposits. Scales formed at the highest temperatures below the boiling zone are enriched in Fe, Mn, Co, and Ni, as well as Cd, and Sn. The latter are also highly enriched in scales from throughout the boiling zone and on the FFCV and OP. Zinc, Cu, Se, and Te are mostly enriched in the lower (higher-temperature) part of the boiling zone, including the FFCV, but are still present in appreciable quantities downstream. Lead, Ag, Sb, (+/-Bi) are mostly enriched in the upper (lower-temperature) part of the boiling zone and immediately downstream of the fluid flow control valve. Arsenic and Hg are enriched in scales downstream. Other trace elements, such as Mo, Ga, V, and Cr are enriched in the deepest scales and in silica-rich precipitates in the surface pipes, but are not present in abundance in the boiling zone.

correlated in higher-temperature scales below the boiling zone (Group I) and in the lower boiling zone (Group II; Fig. 14e). The unexpected correlation of Co with Cd and Zn may reflect the substitution of Co^{2+} for Zn^{2+} in ZnS, especially in high-temperature wurtzite (Vaughan and Rosso, 2006; Maslennikov et al., 2017).

Gold and Ag, which are enriched in scales throughout the Reykjanes system, are variably correlated with Cu, Cd, Te, Bi, and Pb in some but not all samples (Table 7), Although no Au-tellurides have been observed, Te is correlated with Au throughout the Reykjanes system (Fig. 17a). In Group I scales, Au shows strong positive correlations with Cd, Zn, Se, and S and negative correlations with Pb, As, Fe, Mn, and SiO_2 (Table 7). In Group II scales, Au is correlated with Cd (Fig. 17b) and Ag (Fig. 17c). In Group II, II, and IV scales, Au is correlated with Hg (Fig. 17d). The latter reflects lower temperatures of deposition and is consistent with the strong correlation observed between Ag and Pb in samples from the top of the boiling zone in medium- and low-pressure wells (e.g., Fig. 14f). In these samples Ag is also positively correlated with both Sb and As (Fig. 14h and i) and Ag is likely hosted by Sb-bearing galena in high-pressure wells (Fig. 14h). Silver is strongly associated with Cu in Group IV scales dominated by bornite.

Iron is most strongly correlated with Mn, Ni, Cr, Mo, and Sn. The correlation with Cr, in particular, is consistent with these elements being hosted by both silicate and oxide phases, and both elements are weakly correlated with Ca and Ti. Manganese has a positive correlation with Fe (Fig. 14j) and Mo (Fig. 14k), but is not correlated with Ti. This observation is consistent with Libbey and Williams-Jones (2016b) who reported that hematite in the Reykjanes host rock is enriched in Mn relative to sulfide phases. The occurrence of Ni is enigmatic and even though it is enriched, Ni does not directly correspond to any major metals or sulfide mineral throughout the system and is likely primarily associated with a non-sulfide phase. The non-sulfide phases of the scales dictate the behavior of other elements, such as Ga and V. Gallium and V are positively correlated with each other and with SiO_2 (e.g., Fig. 10c) and negatively correlated with Cu, Zn and S, confirming a fundamentally different non-chalcophile behavior for these elements (Wood and Samson, 2006). In the lower temperature distal parts of the system, both Ga and V are positively correlated with strongly lithophile elements (e.g., Cr, Sr, Rb, Sc, and Ba), the lanthanide REE, and all major oxides except for MnO. Thus, they are most likely present in silicates or clays, although Hardardóttir (2011) also noted increased V concentrations in association with maghemite in scales from RN-22. The behavior of Ga and V contrasts with that in seafloor sulfide deposits, where these elements are generally correlated with Cu and Zn (e.g., Grant et al., 2018).

A principal components analysis of the bulk geochemical data on the scales is shown in Table 8, which shows the loadings on the first six factors accounting for 60% of the total variance in the dataset. Large positive loadings on Factor 1 for Fe, Ni, Cr, Mo, Sn, Ga, Ca, Ti, and SiO_2 reflect the co-enrichment of these elements in the oxide and silicate phases. Negative loadings for Zn, Se, S, Ag, Cu, and Pb reflect their co-enrichment in sulfides both below the boiling zone (Group I) and at the OP in the upper boiling zone. Positive loadings on Factor 2 for Co, Se, and Cd reflect the association of these elements with the Zn-sulfides in all scales. Positive loadings on Factor 3 for SiO_2, Na_2O (and Br) correspond to low-temperature precipitation in distal fluids from which most of the metals have already been lost (i.e., downstream Group IV and Group V scales). High positive loadings for Mo, As, and Sb on Factor 4 reflect metal deposition immediately downstream of the OP in the surface boiling zone. The trace metal associations evident in the sulfide scales are similar to those previously reported for the altered and mineralized host rocks sampled in drill cuttings (e.g., Pope et al., 2009; Marks et al., 2015; Libbey and Williams-Jones, 2016b).

5.2. Controls on ore element distribution

The Reykjanes system can be viewed as mostly a closed system

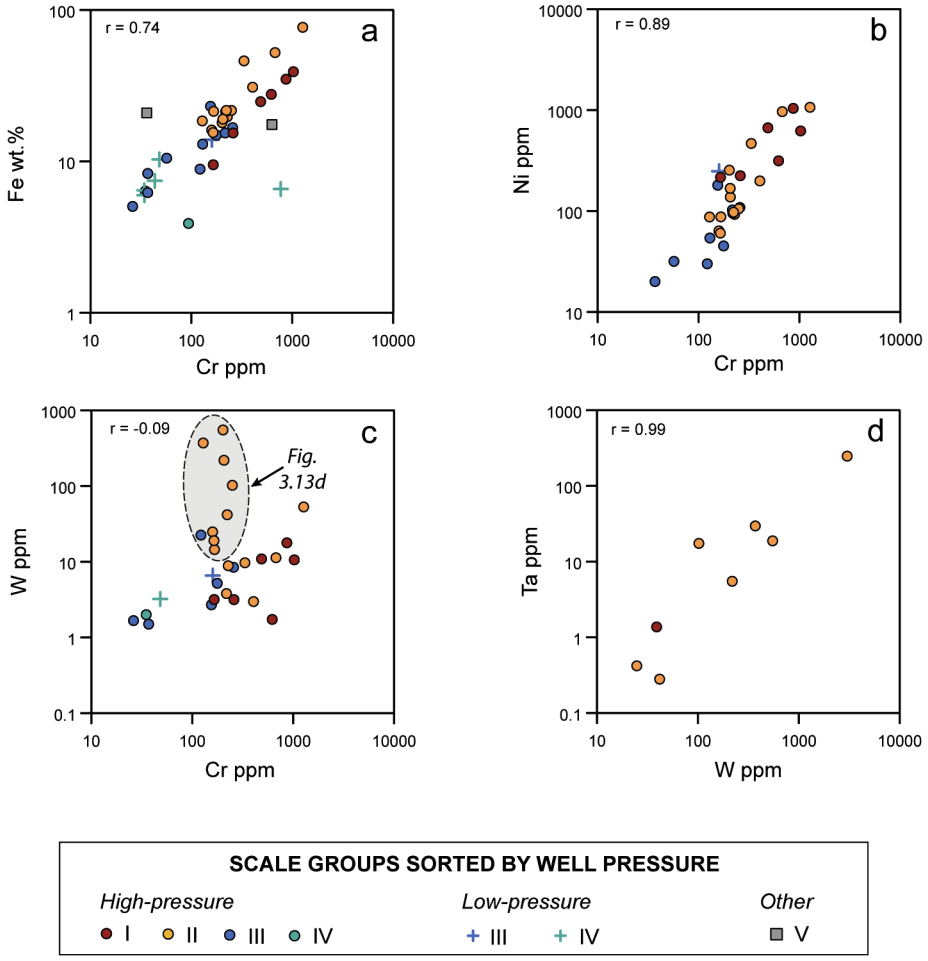

Fig. 13. Bivariate plots for elements in scale samples that may have been affected by drilling contamination or fragments of geothermal well pipe. Positive correlations of Fe and Cr (A) and Cr and Ni (B) likely reflect contamination (see Section 5). Tungsten versus Cr shows a bimodal distribution in (C), with those in gray likely affected by drilling contamination as W concentrations are much higher than any other scales in this study. Samples in C interpreted to have been affected by drilling contamination show a positive correlation with Ta (D) likely from worn drilling equipment, and particularly down-well (see Section 5).

(particularly in surface pipes) as there is limited or no influx of cold seawater reacting with the hot hydrothermal fluid. Scaling is caused by pressure (and temperature) decrease due to boiling during power production. The main ore minerals (sphalerite and wurtzite, chalcopyrite and bornite, galena, native silver and electrum) are precipitated due to abrupt changes in temperature and pH during phase separation, with the acid-generating gases CO_2 and H_2S partitioning into the vapor phase (see Fuchs et al., 2019, for a review).

Cooling in response to boiling is an effective depositional mechanism for the major metal sulfides (Bourcier and Barnes, 1987). Zinc is precipitated as the hexagonal polymorph wurtzite at higher temperatures and mainly as the cubic polymorph sphalerite at and below ~250 °C (Scott and Barnes, 1971). Chalcopyrite precipitation occurs mainly at temperatures between 280° and 320 °C, coincident with the onset of boiling in the Reykjanes system. In the high-pressure wells, more of the Cu remains in solution up to the FFCV where the largest pressure and temperature decrease in the boiling zone occurs, and producing scales with the highest Cu concentrations (e.g. Fig. 16b). In many wells, unordered intermediate Cu-Fe-S solid solutions (i.e., along the bornite-digenite join above 265 °C: Grguric et al., 2000) are produced as a result of rapid quenching, and in many cases, the Cu-and Cu-Fe-sulfides (especially bornite and digenite) appear to have formed by exsolution from an original Cu-Fe-S solid solution (Fig. 6l). These microscopic intergrowths are particularly characteristic of Group III and IV surface scales (Hardardóttir et al., 2010). The formation of optically visible exsolution products has been ascribed to coalescing of submicroscopic domains initially formed during the quenching process (Grguric and Putnis, 1999). Conversely, galena and other Pb-bearing sulfides are most abundant in medium-pressure wells immediately upstream from the OP (Fig. 16b), and somewhat further downhole in lower-pressure wells. Abundant galena is first observed in the scales at the wellhead (T_{max} = 247 °C in RN-12).

Because the Au is likely transported as aqueous sulfur complexes, any process that cause a loss of reduced sulfur, such as sulfide precipitation, boiling, or fluid mixing will destabilize the Au complexes (Seward et al., 2014). Boiling is the dominant precipitation mechanism, and the abundance of Au (i.e., electrum) in the wells increases dramatically with the onset of boiling (e.g., Williams-Jones and Migdisov, 2014; Fuchs et al., 2019). Whereas Ag-chloride complexes predominate at aquifer temperatures, at boiling temperatures, Ag may also be partly transported as aqueous sulfur complexes, like Au (e.g., $AgHS_2^-$: Stefansson and Seward, 2003). In the deeper scales, Ag is mainly present with Au in electrum, rather than as native Ag, and commonly in association with chalcopyrite. Native Ag becomes increasingly abundant at shallow depths in Group III scales in the upper boiling zone. The native Ag filling fractures in scales from RN-21 may have exsolved from Ag-rich Cu- and Cu-Fe-sulfide phases and precipitated in fractures that formed during cooling (e.g., Hardardóttir et al., 2010). The skeletal habit of the native Ag suggests that precipitation was a response to rapid changes in hydrothermal fluid conditions. The spectacular enrichment of Ag at the top of the boiling zone (two orders of magnitude compared to deep scales) and the presence of visible native silver must

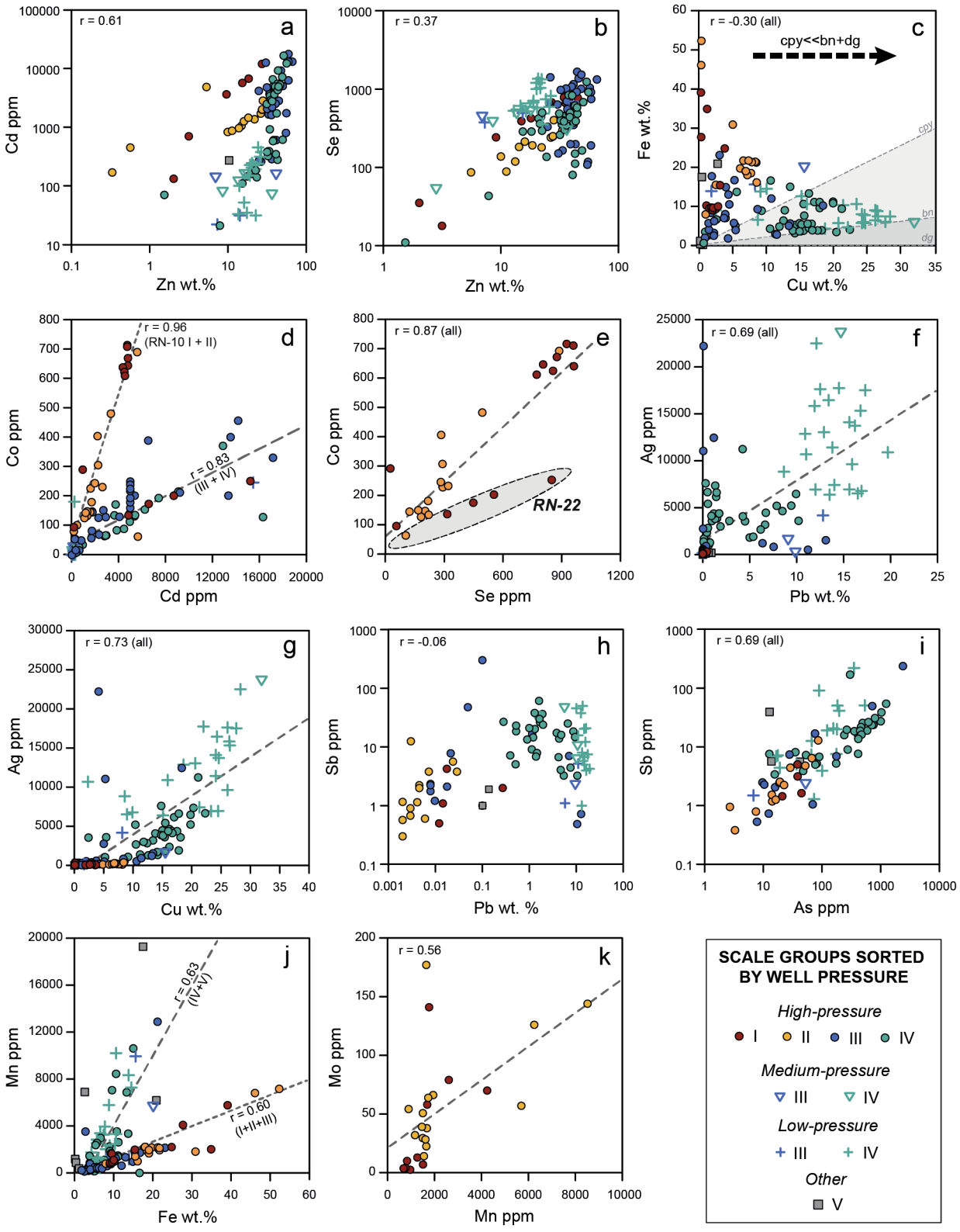

(caption on next page)

Fig. 14. Bivariate plots of selected major and trace elements in different scales of the Reykjanes system. All data have been normalized to zero SiO_2 to remove the variable effects of dilution. A) Zn versus Cd showing a strong positive correlation in all scale groups and sphalerite controls on the distribution of Cd. B) Zn versus Se showing a positive correlation in the majority of scales, particularly in downhole Group I and Group II scaling. C) Fe versus Cu showing the abundance of chalcopyrite in downhole scales compared to Cu-Fe-sulfides with a higher Cu concentration in surface scales (mainly bornite in Group IV). Compositional fields of chalcopyrite, bornite, and digenite are indicated. D) Cd versus Co showing the bimodal distribution of these elements in RN-10 and RN-22 (downhole scales). E) Co versus Se showing the bimodal distribution between Groups I and II (downhole scales) versus Groups III, IV, and V (mainly surface scales). F) Ag versus Pb showing the positive correlation, particularly in Group III and IV scales from medium- and low-pressure wells. G) Cu versus Ag showing the strong positive correlation in all scales. Similar to Pb, the strongest positive correlation of Cu with Ag is in Group III and IV scales from low- and medium-pressure wells. H) Pb versus Sb showing a positive correlation in scales from high-pressure wells only. I) As versus Sb showing the positive correlation between the elements in all scales with the highest concentrations in Group IV scales. J) Fe versus Mn showing the strong bimodal enrichment in both surface and downhole scales. K) Mn versus Mo showing a positive correlation in Group I and II scales. Abbreviations: HP = high-pressure wells, MP = medium-pressure wells, LP = low-pressure wells, cpy = chalcopyrite, bn = bornite, dg = digenite. Group I scales = below boiling zone, Group II scales = lower boiling zone, Group III scales = upper boiling zone, Group IV scales = surface boiling zone, Group V scales = distal, lower-temperature scales.

reflect processes related to flash boiling. However, native silver is also common in late fractures in the scales on the OP and FFCV and immediately upstream or downstream. One interpretation is that Ag-bearing Cu- and Zn-sulfides first precipitated in the scales, and the Ag was remobilized (possibly from solid solution) into the cooling fractures (cf. Hardardóttir et al. 2010).

The distribution of the major and trace metals is mainly due to the temperature-dependence of their aqueous complexes. Zinc, Cd, Pb, and Mn are highly soluble as neutral to weakly-charged chloride complexes (e.g., $ZnCl_2^0$, $CdCl_2^0$, $CdCl_3^-$, $MnCl_2^0$, $MnCl^+$) in high-temperature saline hydrothermal fluids above 300 °C (Suleimenov and Seward, 2000; Bazarkina et al., 2010), and therefore are not expected in the high-temperature scales. However, fluctuations in pressure during artificial well management may have caused the precipitation of these elements even in the deepest parts of the system.

At depths deeper than the boiling zone, Co and Sn, which are transported mainly as chloride complexes in high-temperature, acidic, reduced, saline hydrothermal fluids above 300 °C (e.g., Heinrich, 1990; Liu et al., 2011; Migdisov et al., 2011), are consistently enriched in the Group I scales. Libbey and Williams-Jones (2016b) also noted increased Co concentrations in drill cuttings of mineralized rocks from below the boiling zone. The concentrations decrease with decreasing temperature towards the top of the boiling zone. Iron, Mn, and Ni are transported to lower temperatures than Co and Sn reflecting the relative stabilities of their aqueous complexes (e.g., Suleimenov and Seward, 2000; Testemale et al., 2009; Liu et al., 2012). Elevated concentrations of Ag, Au, As, Cd, Pb, Sb, and Zn occur at and above the boiling zone, and this was also observed in drill cuttings of altered rocks (Libbey and Williams-Jones, 2016b). In general, higher temperatures (e.g., in high-pressure wells) result in Cu-rich scales with low Ag but some As (e.g., Fig. 18), whereas lower temperatures, especially in the low-pressure wells, produce Pb-rich scales enriched in Ag in surface pipes.

Virtually all elements are enriched in Group II scales at the onset of boiling, in response to volatile loss from the liquid, pH change, and the cooling caused by heat loss required for vaporization (e.g., Williams-Jones and Migdisov, 2014; Fuchs et al., 2019). The nearly quantitative deposition of Ag and Cu in all Group IV scales, on the downstream side of the OP and FFCV, may reflect the behavior of their aqueous sulfur complexes destabilized by rapid changes in pressure and temperature, compared to chloride complexes of these metals, which may be dominant in the deeper liquids (Williams-Jones and Migdisov, 2014). Abrupt pressure and temperature decrease at the OP to ~22 bar and 220 °C also promote significant deposition of Bi, Se, As, and Sb at the transition from Group III scales in the upper boiling zone to Group IV scales in the surface pipes. Arsenic, Sb, and Bi, which are all likely transported as neutral hydroxide complexes [$Sb(OH)_3^0$, $As(OH)_3^0$, $Bi(OH)_3^0$: Susak and Crerar, 1985; Pokrovski et al., 2006; Tooth et al., 2013] are only deposited on the OP and FFCV.

After the wellhead, a high proportion of the fluid in the surface pipes is steam. Hardardóttir (2014) described distinctive blue Cu-rich scales in the upper half of upstream high-pressure pipes (Fig. 5e: well RN-22), which were interpreted as deposition from the vapor phase. This is where the steam phase and any volatile metals would be expected to accumulate. Samples of this type of scale from as much as 32 m downstream still contain up to 13.8 wt.% Cu. The strong association of Se and Hg with Cu in these scales (e.g., Fig. 15a) supports the inference that all three were in the vapor phase in these pipes, in contrast to downhole scales, where Se is negatively correlated with Hg. These findings are consistent with the suggestion that Cu can partition into the vapor (steam) during phase separation as HS^--bearing complexes in the presence of significant concentrations of sulfur (cf. Heinrich et al., 1999; Williams-Jones and Heinrich, 2005).

High concentrations of Se and Te in the higher-temperature sulfides in Group I scales are consistent with their behavior in seafloor sulfide deposits (Auclair and Fouquet, 1987; Grant et al., 2018). Selenium enrichment to 100's of ppm throughout the system, particularly in the high-pressure wells, reflects the strong temperature- and pH-dependence of the dissociation of H_2Se, resulting in near complete removal of Se from the fluid phase above 300 °C (e.g., Huston et al., 1995; Hannington et al., 1999). Selenium is also enriched in distal Group IV and V scales where it is positively correlated with Hg and Cu, as noted above (Fig. 15a and 15b). Tellurium, which closely tracks Se in the deep scales of high-pressure wells (Fig. 15d), likely reflects the similar behavior of H_2Te and H_2Se. The single sample with 67 ppm Te collected from the separator station could also reflect the volatility of Te.

Several elements such as Mo and W, which are found in both the deep high-temperature scales but also in the most distal pipes, are transported as oxyanions (e.g., $H_2MoO_4^o$, $HMoO_4^-$, MoO_4^{2-}: Minubayeva and Seward, 2010) and hydroxide complexes (tungstic acid: $H_4WO_4^o$). Their unusual bimodal distribution is controlled by higher-temperature Cu-rich sulfides at depth and oxides and silicates at the surface. Manganese, which is highly mobile, remains in solution and is deposited in the silica-rich scales at the end of the pipelines. Gallium is transported by neutral to weakly-charged hydroxide complexes (e.g., $GaOH^+$, $Ga(OH)_3^o$; Wood and Samson, 2006), and therefore its behavior is most similar to elements such as Mo. Similarly, there appears to be a strong redox control on the precipitation of V (see also Butler and Nesbitt, 1999). High Ba in the separator station may reflect partitioning of the Ba into the chloride-rich brine during phase separation.

5.3. Comparison with SMS deposits

The behavior of the major and trace elements in the sulfide scales of the Reykjanes geothermal system has many similarities to other basalt-hosted seafloor hydrothermal systems, although there is a range of trace metal distributions in MOR vent fluids and deposits, reflecting highly variable reaction zone temperature, pressure, rock composition, and possible impact of sediment/organic material. Conversely, the scales are pyrite-poor, Zn- and Si-rich, and contain far more magnetite than most mid-ocean ridge systems.

The TAG massive sulfide deposit at 26°N on the Mid-Atlantic Ridge is a possible analog (Grant et al., 2018). The TAG deposit is the only sediment-free basalt-hosted active, high-temperature seafloor hydrothermal complex that has been drilled from the seafloor to the bottom

Table 7
Pearson correlation coefficients calculated on log-transformed bulk geochemical data normalized to zero SiO_2 for all scales from the Reykjanes geothermal field.

	Co	Te	Se	Cd	Zn	S	Bi	Au	Cu	Pb	Ag	Sb	As	Mn	Fe	Ni
Co	1															
Te	**0.49**	1														
Se	0.31	0.20	1													
Cd	**0.55**	0.02	**0.43**	1												
Zn	**0.47**	0.08	**0.46**	**0.62**	1											
S	0.28	0.01	**0.55**	**0.41**	**0.88**	1										
Bi	0.05	−0.07	0.02	0.15	0.21	0.20	1									
Au	−0.25	0.13	0.22	0.01	0.05	0.17	**0.42**	1								
Cu	**−0.44**	−0.24	0.21	−0.31	0.02	**0.40**	−0.04	0.23	1							
Pb	**−0.46**	0.04	0.30	**−0.42**	−0.23	0.13	−0.11	**0.42**	**0.69**	1						
Ag	−0.34	−0.14	0.14	−0.29	−0.01	0.28	−0.08	0.16	**0.77**	**0.69**	1					
Sb	–	−0.11	−0.17	−0.02	0.13	0.11	−0.05	−0.04	0.08	0.02	**0.41**	1				
As	–	−0.14	−0.17	0.03	0.26	0.25	−0.06	−0.09	0.17	−0.06	**0.35**	**0.87**	1			
Mn	−0.33	0.24	−0.21	−0.35	**−0.48**	−0.33	−0.06	0.24	0.08	0.31	0.02	−0.02	−0.09	1		
Fe	−0.01	0.01	−0.24	−0.16	**−0.38**	**−0.35**	−0.07	−0.06	−0.24	−0.12	−0.22	−0.14	−0.18	**0.48**	1	
Ni	0.05	−0.13	−0.24	0.03	−0.32	**−0.36**	−0.07	−0.10	−0.30	−0.22	−0.22	−0.07	−0.11	0.24	**0.85**	1
Cr	0.02	−0.18	−0.32	−0.05	**−0.40**	**−0.45**	−0.08	−0.17	−0.34	−0.26	−0.26	−0.09	−0.13	0.21	**0.83**	**0.91**
Sn	0.05	−0.11	−0.13	0.16	−0.19	−0.28	0.10	−0.01	−0.33	−0.26	−0.24	−0.07	−0.12	0.22	**0.80**	**0.86**
Mo	0.10	−0.21	−0.37	0.01	−0.20	−0.26	−0.09	−0.20	−0.28	−0.32	−0.15	0.24	0.22	0.09	**0.69**	**0.74**
In	−0.09	−0.01	−0.02	−0.07	0.05	0.09	0.32	0.17	0.09	−0.05	0.02	−0.02	−0.05	−0.03	–	−0.04
Ge	−0.07	−0.07	−0.07	−0.07	−0.07	−0.15	−0.03	−0.06	−0.13	−0.09	−0.09	−0.03	−0.04	0.04	0.20	0.11
Ca	0.17	0.02	−0.30	−0.02	−0.28	−0.34	−0.10	−0.20	−0.34	−0.28	−0.31	−0.14	−0.17	0.04	0.30	0.30
Ga	0.06	−0.03	−0.23	0.06	−0.31	**−0.51**	−0.09	−0.14	**−0.56**	**−0.36**	**−0.36**	0.02	−0.13	0.02	0.25	0.33
V	0.24	−0.04	0.28	0.28	0.11	0.01	−0.10	−0.15	**−0.36**	−0.29	−0.28	−0.06	−0.11	−0.17	0.14	0.23
Ti	0.13	−0.07	−0.21	0.07	−0.23	−0.31	−0.07	−0.15	−0.29	−0.26	−0.25	−0.11	−0.14	−0.06	0.22	0.28
W	0.16	−0.02	−0.09	−0.03	−0.02	−0.03	−0.03	−0.05	−0.05	−0.09	−0.08	−0.04	−0.05	−0.01	0.11	0.09
SiO_2	−0.17	−0.02	**−0.49**	−0.27	**−0.63**	**−0.79**	−0.07	−0.15	**−0.41**	−0.21	−0.29	−0.02	−0.16	0.06	−0.07	0.02
Ba	−0.08	−0.11	−0.20	−0.06	−0.26	**−0.35**	−0.01	0.02	−0.20	−0.19	−0.18	–	−0.09	–	−0.05	0.04
Br	−0.10	−0.05	−0.24	−0.13	−0.28	**−0.39**	−0.04	−0.18	−0.21	−0.15	−0.15	−0.06	−0.06	−0.11	−0.13	−0.05
Tl	−0.07	−0.09	0.01	−0.04	−0.10	−0.12	−0.05	−0.06	−0.10	−0.06	−0.03	0.08	0.03	−0.04	0.07	0.02
Hg	−0.08	−0.14	**0.44**	−0.05	−0.01	0.12	−0.06	0.13	0.24	0.27	0.20	−0.03	−0.02	−0.13	−0.03	−0.08
U	−0.04	−0.05	0.04	−0.01	0.05	0.15	−0.02	−0.01	0.19	0.09	0.19	0.11	0.15	−0.01	−0.05	0.02
Th	−0.08	−0.08	−0.06	0.01	0.04	0.03	0.04	–	0.05	−0.06	0.01	–	0.04	−0.02	−0.08	−0.05

	Cr	Sn	Mo	In	Ge	Ca	Ga	V	Ti	W	SiO_2	Ba	Br	Tl	Hg	U	Th
Co																	
Te																	
Se																	
Cd																	
Zn																	
S																	
Bi																	
Au																	
Cu																	
Pb																	
Ag																	
Sb																	
As																	
Mn																	
Fe																	
Ni																	
Cr	1																

(*continued on next page*)

Table 7 (*continued*)

	Cr	Sn	Mo	In	Ge	Ca	Ga	V	Ti	W	SiO_2	Ba	Br	Tl	Hg	U	Th
Sn	**0.76**	1															
Mo	**0.78**	**0.64**	1														
In	−0.05	0.17	−0.05	1													
Ge	0.13	0.12	0.10	−0.02	1												
Ca	**0.40**	0.15	0.34	−0.06	−0.06	1											
Ga	0.34	**0.35**	0.29	−0.07	0.07	0.35	1										
V	0.17	0.21	0.12	−0.08	0.10	0.21	0.32	1									
Ti	0.34	0.19	0.30	−0.05	−0.04	**0.90**	0.33	0.34	1								
W	0.09	0.02	0.18	−0.01	−0.01	0.12	0.01	−0.02	0.07	1							
SiO_2	0.07	−0.04	−0.02	−0.05	0.03	0.21	**0.57**	−0.08	0.18	−0.01	1						
Ba	0.09	−0.01	0.02	−0.02	–	0.13	0.14	0.13	0.16	−0.02	**0.43**	1					
Br	−0.02	−0.07	−0.05	−0.03	−0.03	−0.03	−0.10	−0.10	−0.03	–	**0.40**	0.19	1				
Tl	0.04	0.03	0.05	−0.03	0.14	−0.07	0.13	0.23	−0.07	−0.03	0.11	0.18	–	1			
Hg	−0.05	−0.05	−0.09	−0.05	0.02	−0.20	−0.11	0.24	−0.11	−0.05	−0.19	0.09	−0.07	**0.45**	1		
U	−0.07	0.02	−0.03	0.14	−0.07	−0.02	−0.14	−0.08	0.02	−0.07	−0.12	0.02	−0.10	−0.13	−0.17	1	
Th	−0.04	−0.02	−0.05	0.19	−0.02	0.01	−0.09	−0.07	−0.02	−0.03	−0.04	0.14	−0.03	−0.05	−0.05	0.30	1

Pearson correlation coefficients for selected major and trace components calculated on log-transformed bulk geochemical data for all scales from the Reykjanes geothermal field. Data was normalized to zero SiO_2 to remove effects of dilution. Number of components (degrees of freedom) = 33. Correlations significant at the 99% confidence level are highlighted in bold and dark gray and correlations significant at the 95–99% confidence level are highlighted in bold and light gray. These significance thresholds (or critical values) are for n-2 degrees of freedom and a one-tailed *t*-test. '–' indicates no data.

of its stockwork zone (a depth of 125 m below seafloor: Petersen et al., 2000). However, unlike the Reykjanes geothermal system, the TAG upflow zone is completely open to seawater and therefore has been affected by mixing, and the high pressures at 3400–3600 m water depth prevent extensive boiling of the hydrothermal fluids in the sub-seafloor.

The compositions of the deepest scales at Reykjanes are similar to the highest temperature sub-seafloor stockwork mineralization at TAG, which is enriched in Cu, Co, Se, Bi, Sn, and Ni compared to the seafloor sulfides. The behavior of Se, however, which is locally enriched in the surface pipes, contrasts with typical seafloor hydrothermal systems, in which Se is only found in the highest-temperature sulfide assemblages. An atypical lack of correlation in Reykjanes scales versus typical seafloor hydrothermal systems is also observed for Zn and Ag due to the high pH of the Reykjanes reservoir fluids. In many/most MOR systems, wurtzite and sphalerite are saturated at significantly higher temperatures at a higher fluid pH. Since Ag is dominantly associated with lower temperature portions of deposits, under these conditions of high temperatures and an elevated fluid pH, there is a lack of correlation between Ag and Zn in the Reykjanes system (Tivey et al 1999; Kristall et al., 2011; Evans et al., 2017).

The abundance of Zn-sulfides at depth, compared to Cu-(Fe)-sulfides, mainly reflects the bulk compositions of the deep fluids, which have a high Zn/Cu ratio (Hardardóttir et al., 2009) compared to black smoker vents. Similarly high Zn/Cu ratios have been observed in some MOR and back-arc systems with lower reaction zone temperatures than EPR systems (e.g., Lucky Strike and some on the eastern Lau Spreading Center: Mottl et al., 2011; Evans et al., 2017). The influence of a higher pH is also reflected by precipitation of Zn-sulfide minerals either first or together with Cu-(Fe)-sulfides in the deep scales. If the pH is high, under these conditions sphalerite is precipitated at a much higher temperature than normally expected for MOR vents (Fig. 19).

Lower-temperature parts of the seafloor mound at TAG are enriched in Zn, Cd, In, Pb, Ag, Sb, and Tl, similar to the lower-temperature scales in the surface pipes at Reykjanes. For the most part, Mn behaves conservatively in the TAG deposit (i.e., not precipitated in the deposit and mainly lost to the hydrothermal plume), similar to its behavior in the Reykjanes system. Local enrichment of Mn in the deepest scales at Reykjanes likely reflects processes similar to the Mn enrichment in non-sulfide phases (chlorite and amphibole) in the alteration zones of some seafloor hydrothermal systems (e.g., Heft et al., 2008; Gillis and Thompson, 1993). Silica deposition at Reykjanes mainly is a consequence of conductive cooling of the brine phase in the surface pipelines, a process that is similar to the modeled deposition of silica by conductive cooling in the TAG deposit (Tivey et al. 1995). A key difference between TAG and Reykjanes as noted above is the lack of seawater entrainment in the Reykjanes system. The higher pH at Reykjanes however, likely explains the elevated abundances of amorphous silica in scales compared to most mid-ocean ridge systems.

Fluids in the TAG hydrothermal systems have only boiled at very high temperatures, owing to the pressure of the overlying water column (Petersen et al., 1998). However, boiling hydrothermal vents have now been documented widely and at a range of water depths comparable to the Reykjanes system (Monecke et al. 2014, 2016). Trace metal enrichments in the boiling chimneys are very similar to those documented in the scales at Reykjanes, with different metal associations at high- and lower-temperature boiling (Monecke et al., 2014; Gartman et al., 2018).

Fig. 20 compares the average trace element contents of Reykjanes scales to the bulk compositions of analogous high-temperature black smoker chimney samples from elsewhere along on the Mid-Atlantic Ridge. The majority of siderophile elements (e.g., Mn, Cd, Ni, Zn) are enriched in the Reykjanes system compared to black smokers, in part because of dilution by silica and sulfate in the seafloor vents. However, Fe, Co, Ga, Ge, In, and Mo are relatively depleted, implying a significant difference in fluid or source-rock concentrations. Copper, Se, and Te concentrations are similar. Gold, and the chalcophile elements Ag and Pb, are extremely enriched compared to MAR black smokers. Elements

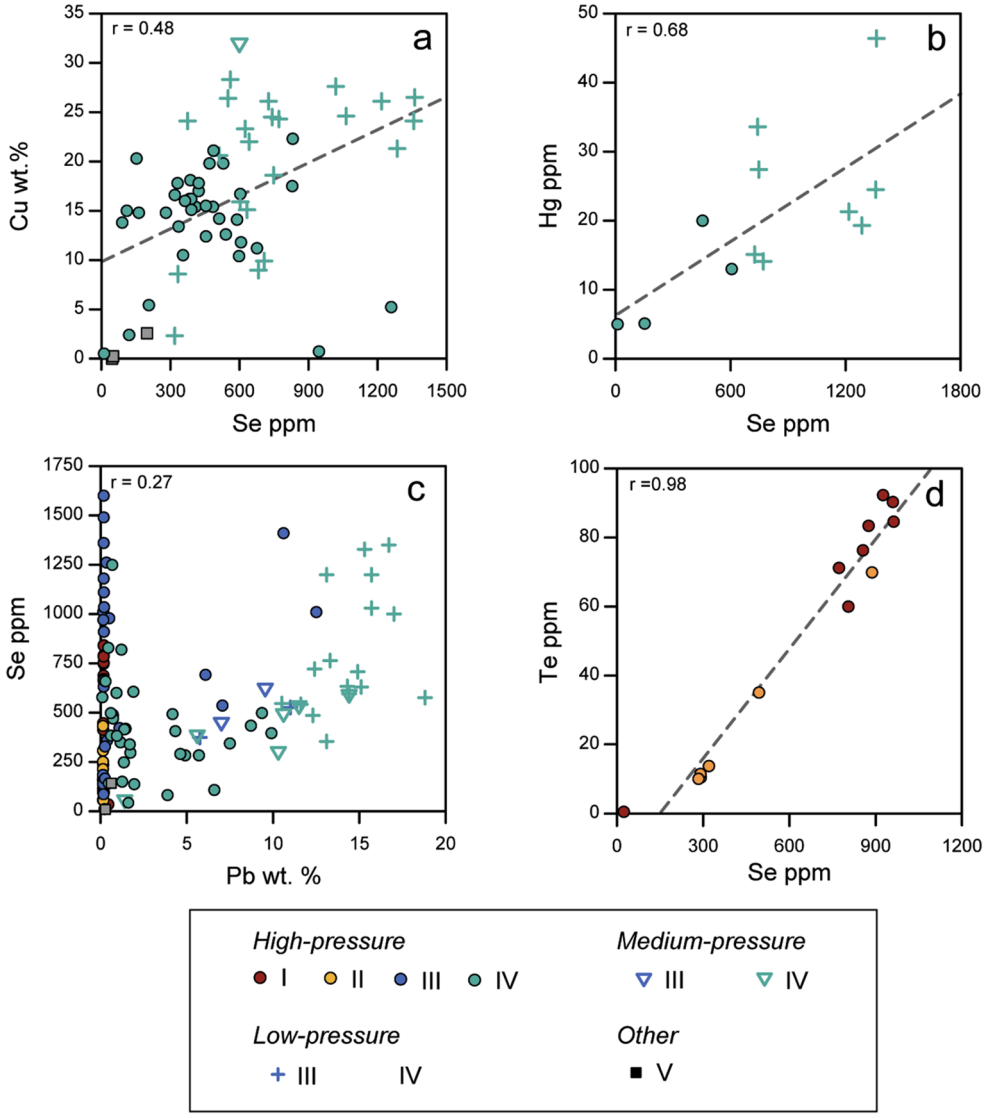

Fig. 15. Bivariate plots of Se versus Cu, Hg, and Te in different scales of the Reykjanes system. All data is normalized to zero SiO_2 to remove the variable effects of dilution. A) Se versus Cu showing the positive correlation in Group IV scales on the OP/FFCV and downstream, particularly in medium-pressure wells. B) Se versus Hg showing the positive correlation (above detection) in Group IV and V scales. C) Se versus Pb showing the positive correlation in medium- and low-pressure Group IV scales, likely indicating incorporation of Se into Pb-bearing minerals (e.g., galena). D) Se versus Te showing the positive correlation in Group I and II scales in all wells. Both Se and Te are higher in Group I scales below the onset of boiling. Group I scales = below boiling zone, Group II scales = lower boiling zone, Group III scales = upper boiling zone, Group IV scales = surface boiling zone, Group V scales = distal, lower-temperature scales.

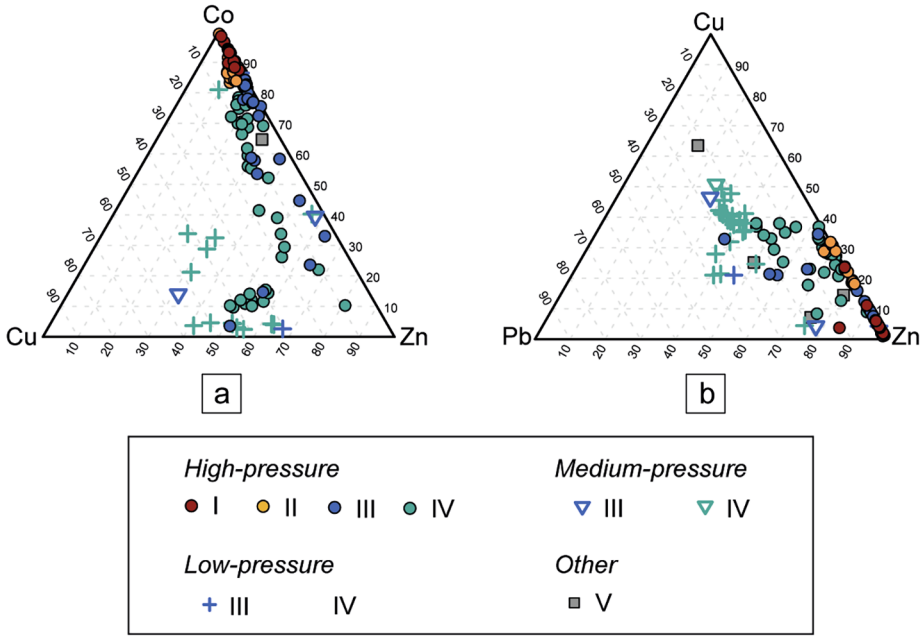

Fig. 16. Ternary plots for selected major and trace elements in scales from all well types in the Reykjanes system. All data are normalized to zero SiO_2 to remove the variable effects of dilution. Data for Cu, Zn and Pb is wt.%, and Co is in ppm. A) Co-Zn-Co ternary showing the relative enrichment of Co in the deep Group I (red) and Group II (orange) scales, which are generally more Fe-rich and Zn-poor compared to scales in the upper boiling zones. B) Cu-Zn-Pb ternary plot showing the enrichment of Zn in Group I scales (red) and increase in Cu in Group II scales (blue). Group IV scales are Pb- and Cu-rich and Zn-poor compared to the other scales. Scales from Group IV medium- and low-pressure wells have the highest Pb and Cu, and the least Zn. Group I scales = below boiling zone, Group II scales = lower boiling zone, Group III scales = upper boiling zone, Group IV scales = surface boiling zone, Group V scales = distal, lower-temperature scales. (For interpretation of the references to color in this figure legend, the reader is referred to the web version of this article.)

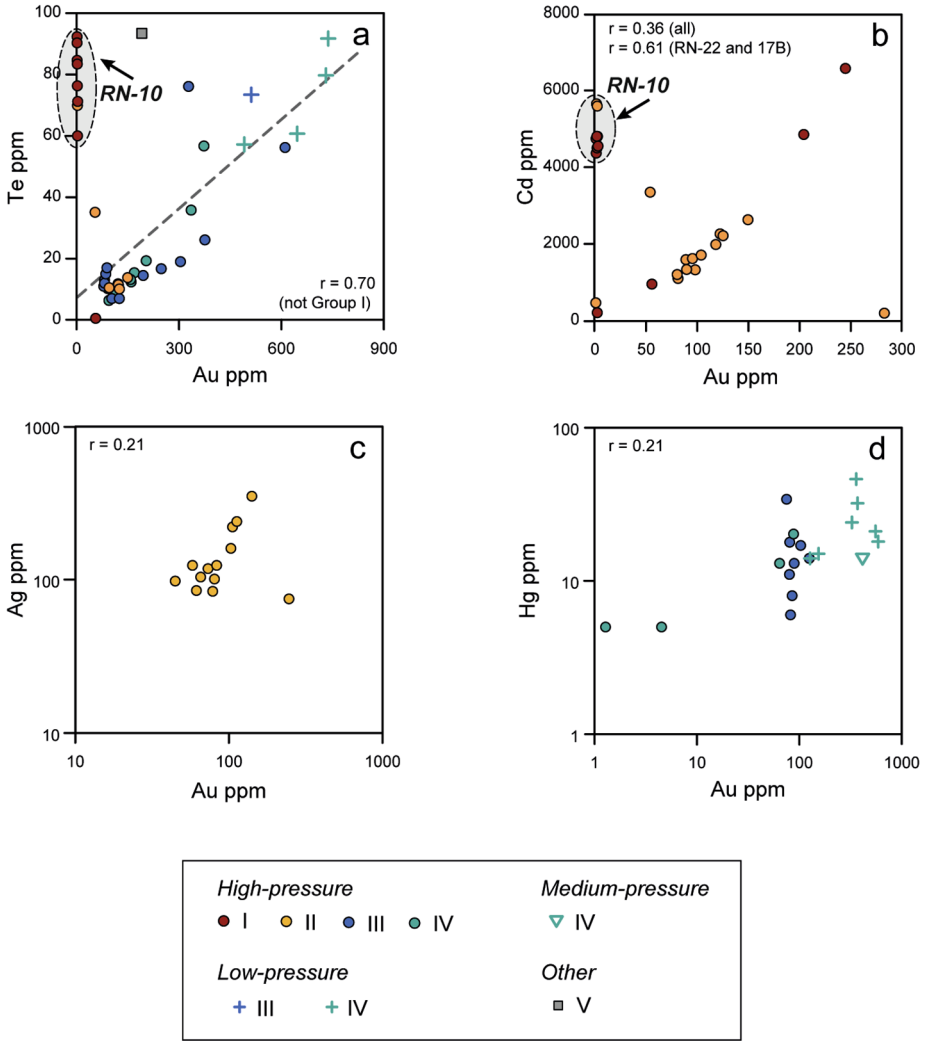

Fig. 17. Bivariate plots of Au versus Te, Cd, Ag, and Hg in different scales of the Reykjanes system. All data are normalized to zero SiO_2 to remove the variable effects of dilution. Gold concentrations are comparable in all of the wells within the boiling zone (e.g., Group II scales and higher). Below the boiling zone, Au concentrations in Group I scales are high in RN-17B and RN-22 but low in RN-10. A) Au versus Te showing positive correlations in Group II, III, and IV scales. Gold concentrations are highest in Group III and IV scales from medium-pressure wells. B) Au versus Cd showing positive correlation in Group I and II scales. C) Au versus Ag showing positive correlations in Group II scales indicating Au is hosted by electrum above the onset of boiling. Gold and Ag are not correlated in other scale groups. D) Au versus Hg showing positive correlations in all Group III and Group IV scales. Group I scales = below boiling zone, Group II scales = lower boiling zone, Group III scales = upper boiling zone, Group IV scales = surface boiling zone, Group V scales = distal, lower-temperature scales.

such as U, Tl, and Ba are depleted in the Reykjanes scales compared to seafloor black smokers because of the lack of seawater mixing in the wells.

The major differences in the trace metal concentrations between the Reykjanes scales and black smokers reflect the important role of boiling as a depositional mechanism; however, this cannot account for some of the high metal concentrations, as previously observed by Hardardóttir et al. (2009). Hannington et al. (2016) recently suggested that some metal enrichment may be due to accumulation of the metals in the deep geothermal reservoir prior to discharge into the hydrothermal system – a process that has not yet been observed in active seafloor hydrothermal systems. This is supported by the orders of magnitude differences in the ratios of Au, Ag, and Pb to the major elements for Reykjanes scales versus MAR black smokers (Fig. 21). Average Ag concentrations (10–100 ppm) in the deep scales are typical of what has been observed in black smokers and in drilled stockworks; by contrast, it seems likely that most of the Au and Pb in seafloor hydrothermal systems are lost to hydrothermal venting.

5.4. Implications for metal budgets of seafloor hydrothermal systems

The mass accumulation of metals in the downhole scales of the high-pressure well RN-10 between 2009 and 2014 can be estimated by assuming a uniform thickness of 0.5 cm from the wellhead to 1832 m depth. In the 5 years between cleaning of the well, approximately 24 tonnes (t) of scales had been deposited, consisting of 15.1 t sphalerite, 5.3 t chalcopyrite, 3.2 t bornite, 95 kg galena, and 44 kg electrum (calculations in Supp. Info. A1.1). Hardardóttir (2011) estimated that ~1 t of sulfide scale per year (t/yr) are deposited in a single high-temperature surface well pipe; combined with the downhole scales, this corresponds to an estimated total mass accumulation rate of ~5.7 t/yr for RN-10 (fluid discharge up to 2.3 kg/s; Sigurdsson, 2012).

A sulfide accumulation rate of ~5.7 t/yr in RN-10 corresponds to metal fluxes of 1.7 t/yr Zn, 0.3 t/yr Cu, 22.5 kg/yr Pb, 4.1 kg/yr Ag, and 0.5 kg/yr Au (Supp. Info. A1.2). Hardardóttir et al. (2009) calculated metal fluxes for the whole of the Reykjanes system from the metal concentrations in the deep fluids and estimated fluxes of ~47 t/yr Cu, 47 t/yr Zn, ~740 kg/yr Pb, 180 kg/yr Ag, and ~9 kg Au. The data presented from RN-10 indicates that relative to the metal contents of deep fluids feeding the entire geothermal system, the metal contents of Cu in particular in RN-10 scaling may be less than would be expected. However, across the entire system (i.e., RN-10 is one of the 16 current production wells), accumulation of Zn, Pb, Ag, and particularly Au may be roughly comparable. By comparison to a large SMS deposit, the calculated mass accumulation rates for the TAG active mound are 7.6–15.2 t/yr Cu, 1.5–3.0 t/yr Zn, 38–76 kg/yr Pb, 5.3–10.6 kg/yr Ag, and 0.19–0.38 kg/yr Au, assuming metal contents of 76 kt of Cu, 1.5 kt of Zn, < 380 t Pb, 53.2 t Ag, and 1.9 t of Au accumulated over the estimated 5000–10,000 years which the mound has been active (Lalou et al., 1995; Hannington et al. 1998). Calculated metal fluxes for one high-temperature Reykjanes production well show higher fluxes of Au compared to the entire TAG active mound, comparable fluxes for Zn,

Table 8
Results of Principal Components Analysis of all scale bulk geochemical data.

	Factor 1	Factor 2	Factor 3	Factor 4	Factor 5	Factor 6
Eigenvalue	6.69	3.94	3.54	2.43	2.05	1.75
Variance %	19.67	11.60	10.42	7.14	6.02	5.14
Cumulative %	19.67	31.27	41.69	48.83	54.85	59.98
Co	0.02	0.38	0.14	0.01	0.07	0.18
Te	−0.02	0.07	0.10	−0.22	0.19	0.25
Se	−0.21	0.21	−0.02	−0.28	−0.20	0.08
Cd	−0.04	0.40	0.09	0.01	−0.01	−0.09
Zn	−0.22	0.37	0.05	0.10	0.05	−0.07
S	−0.30	0.26	−0.08	0.05	0.04	0.02
Bi	−0.05	0.08	−0.01	−0.10	0.23	−0.46
Au	−0.12	−0.06	−0.13	−0.26	0.11	−0.24
Cu	−0.25	−0.21	−0.21	0.02	−0.02	0.10
Pb	−0.19	−0.27	−0.21	−0.18	−0.07	0.19
Ag	−0.21	−0.20	−0.21	0.16	−0.09	0.13
Sb	−0.06	−0.02	−0.08	0.52	−0.10	−0.02
As	−0.09	0.01	−0.09	0.54	−0.06	−0.01
Mn	0.08	−0.20	−0.22	−0.17	0.15	0.08
Fe	0.26	0.05	−0.34	−0.10	0.02	0.03
Ni	0.28	0.10	−0.30	−0.01	−0.01	−0.03
Cr	0.30	0.06	−0.26	0.01	−0.02	−0.01
Sn	0.24	0.14	−0.29	−0.05	0.03	−0.20
Mo	0.24	0.11	−0.26	0.23	−0.02	0.02
In	−0.03	0.00	−0.05	−0.04	0.23	−0.38
Ge	0.06	0.00	−0.05	−0.03	−0.14	−0.14
Ca	0.23	0.06	0.06	0.01	0.11	0.31
Ga	0.24	0.05	0.06	0.00	−0.11	−0.04
V	0.10	0.23	0.04	−0.08	−0.34	0.03
Ti	0.21	0.08	0.06	0.02	0.04	0.26
W	0.05	0.04	−0.01	0.02	0.07	0.13
SiO2	0.21	−0.24	0.27	0.03	−0.02	−0.11
Ba	0.11	−0.10	0.16	0.02	−0.14	−0.22
Br	0.09	−0.17	0.27	0.06	0.00	−0.10
Tl	0.03	−0.02	0.00	−0.01	−0.47	−0.19
Hg	−0.08	−0.01	−0.07	−0.15	−0.52	−0.06
U	−0.06	−0.01	−0.08	0.15	0.21	−0.01
Th	−0.02	−0.02	0.00	0.09	0.17	−0.20

The first six factor loadings resulting from Principal Components Analysis are ordered according to the percentage of total variance in the dataset. The data were normalized to zero SiO_2 to account for variable dilution effects.

Pb, and Ag, and a much lower flux for Cu. Table 9 shows the calculated amount of potential metal accumulation in well RN-10 during the life of the Reykjanes system (~20,000 years; Hardardóttir, 2011), if we assume continuous deposition of scales and no limitation on the space that could be filled with sulfides (calculations in Supp. Info. A1.3). The mass accumulation and metal flux calculations for only one production well indicate that the Reykjanes system is highly enriched in the trace elements Pb, Au, and Ag compared to the mature TAG mound, similar to that shown in Fig. 20. The calculated mass accumulation rates in Table 9 are also reasonable for mid-ocean ridge seafloor hydrothermal systems. There are currently 16 wells in operation, and assuming all deposited the same amount of scales (see Supp. Info. A1.3), ~91 t of sulfide is deposited in the geothermal wells at Reykjanes every year. Jamieson et al. (2014) calculated sulfide mass accumulation rates ranging between 1 and 794 t/yr for selected hydrothermal fields; a rate of ~91 t/yr for the whole Reykjanes system is geologically reasonable and is comparable to estimates for numerous high-temperature basalt-hosted seafloor hydrothermal systems (e.g., 101 t/yr at Snakepit; Jamieson et al., 2014).

Direct observations from this study show that at least three quarters of the metal budget of a similar boiling seafloor hydrothermal system may be deposited at depth or in the upflow zone (i.e., downhole pipes), before ever reaching the surface (e.g. Table 9). A comparison of published data by Hannington et al. (2016) on the composition of the deep liquids with the surface discharge shows that Fe, Zn, and Ni are nearly quantitatively precipitated in the sulfides downhole, 70–90% of the Mg is deposited, mainly as clay minerals, but only 30% of the As is deposited. This is consistent with the relative mass accumulations for these metals in downhole pipes versus surface pipes in Table 9.

The discovery of a supercritical fluid reservoir at 4.5 km depth at Reykjanes (Fridleifsson et al., 2017), and the accumulation of Au and potentially Ag and Pb in deep reservoirs (Hannington et al., 2016, and this study) further highlights the potential for metal enrichment and accumulation in the deep parts of the geothermal system. The deposition and residence of metals within the lower oceanic crust is supported by mass balance calculations in other deep oceanic crust profiles such as Hess Deep, Pito Deep, and Hole 1256D (e.g., Gillis and Thompson, 1993; Heft et al., 2008; Alt et al., 2010; Jowitt et al., 2012; Patten et al., 2016). Metal trapping efficiencies ranging from 4 to 37% were estimated by Patten et al. (2017) in the Troodos ophiolite between lower sheeted dyke sections and associated VMS deposits. Deep trapping processes may be much more common in the subseafloor than previously thought. Indeed, ODP drilling at the sedimented Middle Valley deposit found deep Cu-rich zones with grades between 8.0 and 16.6 wt. % below well-developed stringer zones (Zierenberg et al., 1998); these concentrations fall within the range of Cu grades of Reykjanes scales.

5.5. Conclusions

This paper focuses on observations of geochemical enrichments and depletion within the upflow zone of the Reykjanes geothermal system, a system directly analogous to basalt-hosted seafloor hydrothermal systems. Sulfide-rich scales in the geothermal wells provide a snapshot of metal precipitation from the hydrothermal fluids, in the absence of significant mixing with seawater as occurs in active seafloor hydrothermal systems. Well-constrained conditions of formation enable a rigorous interpretation of the behavior of trace elements, with Co, Se, Cu, and Sn deposited in the highest-temperature scales; Mo, As, Ni, and Te in high- to intermediate-temperature scales, and Ag, Pb, Sb, Zn, Cd, and Mn in lower-temperature scales. Distal hydrothermal precipitates, downstream of the OP and FFCV and in the separator station are enriched in Ga, V, Br, and SiO_2. These majority of these element associations show many similarities to trace element distribution in subseafloor SMS mineralization, as observed in the large, actively-forming TAG deposit (Grant et al., 2018). However mineralogical and trace element associations also show several differences compared to known SMS sub-seafloor mineralization: i) fluid pH is slightly acidic but high compared to most MOR vent fluids, and this high pH may explain the high abundances of Zn-sulfide minerals and amorphous silica in the scales; iii) high Cu, Zn, and Ag concentrations in sulfide scales likely in part reflect a combination of the relatively high Cu, Zn, and Ag concentrations and lower Fe concentrations of the Reykjanes fluids compared to most MOR fluids but also the efficiency of deposition of the metals and the lack of dilution by minerals precipitated during mixing with seawater (e.g., anhydrite); iv) Fe is surprisingly scarce; and v) Cu and Se which normally demarcate the highest-temperature mineralization, are also present in appreciable quantities in lower-temperature scales.

Additionally, and of greater significance, is that the Reykjanes scales show the significant influence that boiling has on the “subseafloor” deposition of the majority of trace elements. At least three quarters of the Reykjanes metal budget is deposited at depth or in the upflow zones of the boiling system. Deposition of a significant proportion of the metal budget deep in submarine hydrothermal systems has profound implications for metal enrichment and accumulation at depth and supports previous observations in ophiolites. The spectacular concentrations of Au in the scales from all parts of the boiling zone and throughout the surface pipelines reflect the efficiency of gold deposition due to boiling but also high concentrations of Au (and potentially Ag and Pb) that have accumulated in the reservoir liquids.

A calculated mass accumulation rate of ~91 t/yr for the Reykjanes

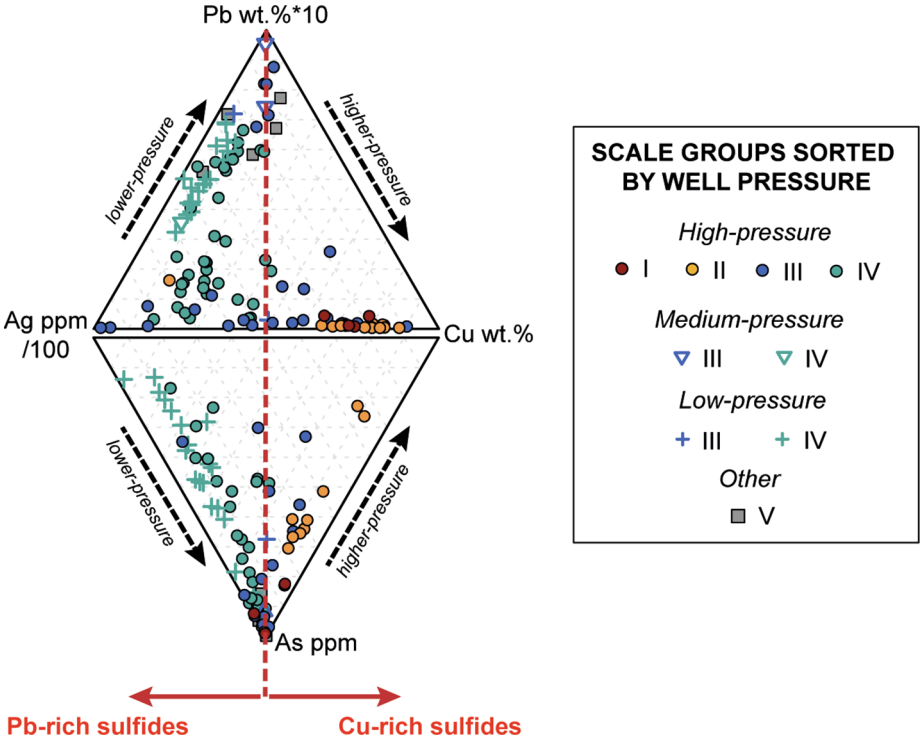

Fig. 18. Paired ternary plots showing the different distributions of As and Ag in Reykjanes scaling. All data have been normalized to zero SiO_2 to remove the variable effects of dilution. On the left side are mostly lower-pressure and lower-temperature Pb-rich scales from Groups III and IV, some with high Ag (low-pressure wells) and some with high As (high-pressure wells). On the right side are mostly Cu-rich downhole Group I and II scales from high-pressure wells with low-Ag, but some As. Group I scales = below boiling zone, Group II scales = lower boiling zone, Group III scales = upper boiling zone, Group IV scales = surface boiling zone, Group V scales = distal, lower-temperature scales.

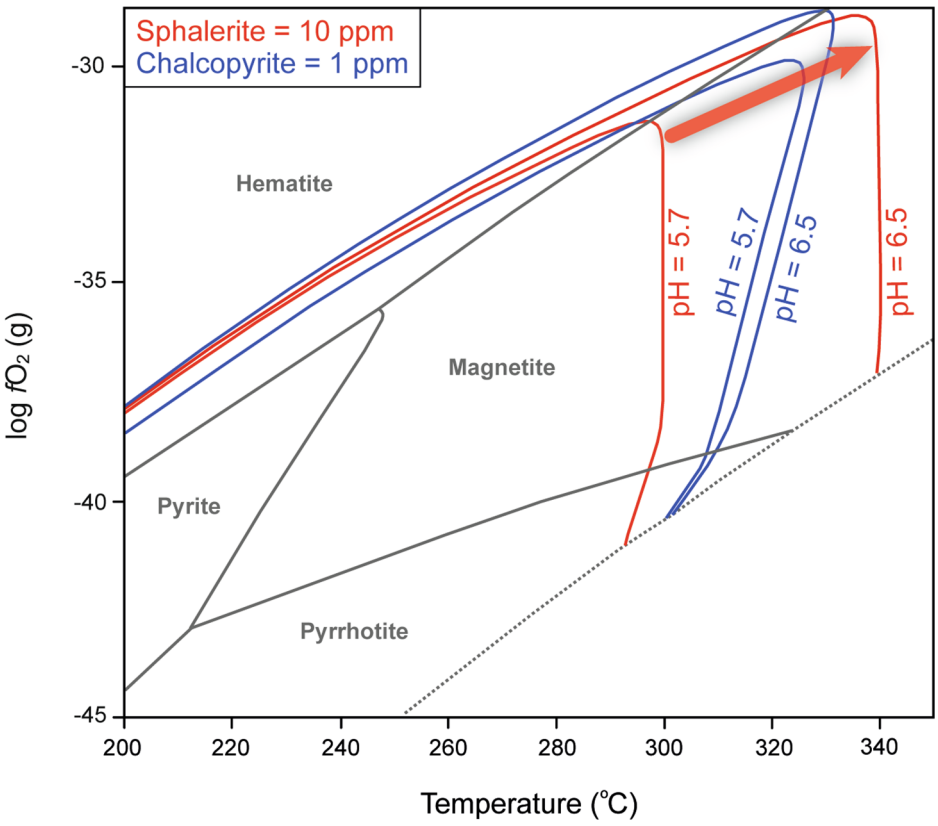

Fig. 19. Phase diagram of predominant Fe-mineral species as a function of the temperature and log fO_2 of the hydrothermal fluids from the Reykjanes geothermal field. To show how the solubility of the two major sulfide minerals in the Reykjanes system changes when pH is increased, sphalerite and chalcopyrite solubilities were plotted for pH (in situ) of 5.7 and 6.5 respectively. The in situ pH of 5.7 was calculated from the measured pH (at 25 °C) of 5.3 (Hannington et al., 2016). The red and blue lines are selected solubilities for sphalerite and chalcopyrite at the indicated pH. The higher pH of the Reykjanes fluids results in a large change in the solubility of sphalerite at higher temperatures, as indicated by the shift to the right of the 10 ppm solubility contour for sphalerite at pH 6.5 versus a pH of 5.7 (red arrow). An increase in pH does not significantly influence the solubility of chalcopyrite. The phase diagram was generated using thermodynamic data taken from the recent version of the SUPCRT database (Johnson et al., 1992), implemented in the Geochemist's Workbench software package (detailed description in Fuchs et al. 2019. Conditions to the right of the dotted line are highly reduced; water is not stable under these conditions and mineral phases are not precipitated. A pressure of 500 bars was assumed, and an average fluid composition of ΣS = 39 mg/kg, Cl^- = 18200 mg/kg were used (data from Hannington et al. 2016). (For interpretation of the references to color in this figure legend, the reader is referred to the web version of this article.)

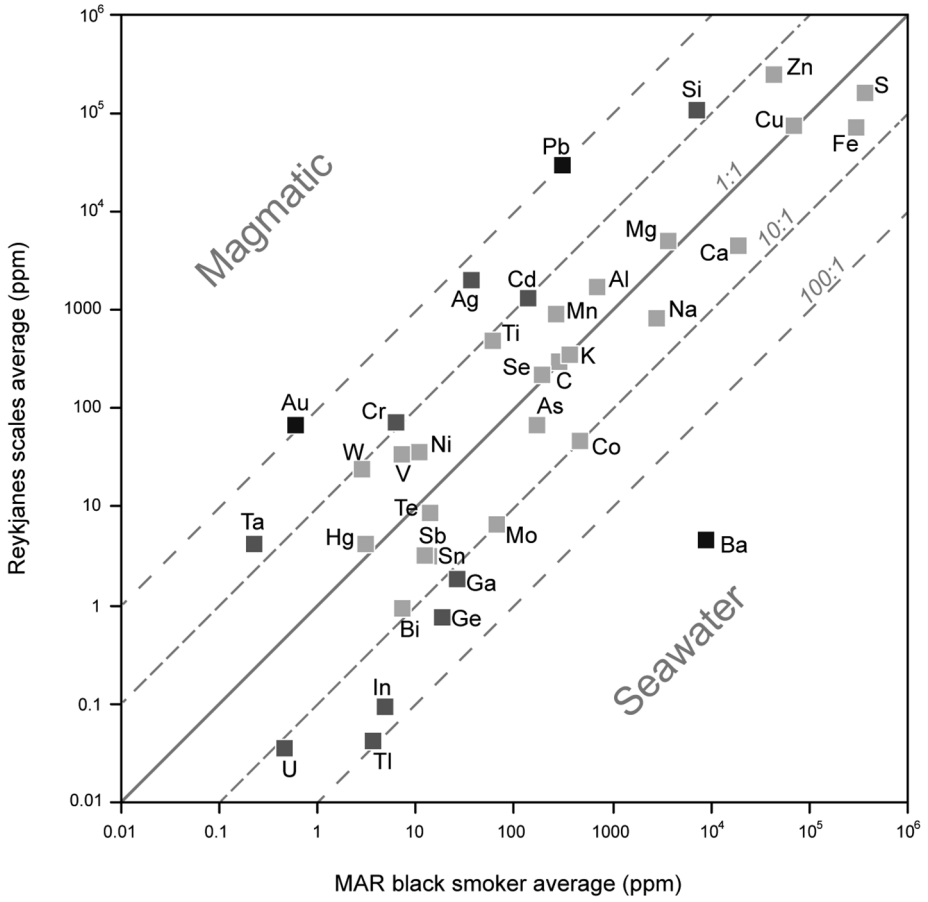

Fig. 20. Comparison of average bulk geochemistry for all scale samples (n = 129) from the Reykjanes geothermal field versus average bulk geochemical data for high-temperature black smoker samples (n = 103) from analogous basalt-hosted Mid-Atlantic Ridge (MAR) SMS deposits (GEOMAR unpublished database). Elements plotting above the 1:1 line are enriched in Reykjanes sulfide scales, and elements plotting below the 1:1 line are enriched in MAR samples. The darker the marker, the higher the relative enrichment. Gold, Ag, and Pb are significantly enriched in Reykjanes scales, and Ba is depleted compared to MAR black smoker sulfides. See Section 5.3 for discussion.

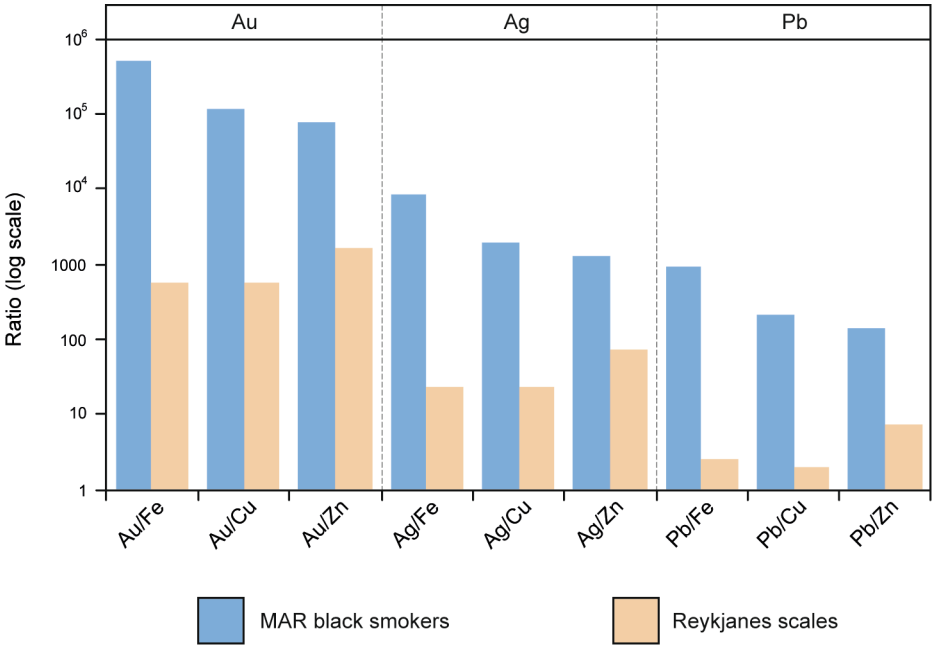

Fig. 21. Ratios of the trace metals Au, Ag, and Pb to major elements in Reykjanes scales and Mid-Atlantic Ridge (MAR) black smoker samples. Gold, Ag, and Pb are highly enriched in Reykjanes scales relative to analogous black smokers (Fig. 20). Orders of magnitude lower ratios in the Reykjanes samples illustrate the enrichment of Au, Ag, and Pb in hydrothermal fluids. Deposition of metals in the closed Reykjanes system is highly efficient compared to MAR fluids where the vast majority of metals are lost to hydrothermal venting. However, the sheer magnitude of difference in ratios supports the observations of Hannington et al. (2016) that metals such as Au, Ag, and Pb can accumulate in deep hydrothermal reservoirs and that the total metal budget of seafloor hydrothermal systems is far greater than previously estimated.

Table 9
Calculated mass accumulations (in tonnes and kg) for well RN-10 over the estimated lifetime of the Reykjanes geothermal system.

a	METALS (t)			b	OTHER ELEMENTS (t)			c	REEs (kg)		
	Total	Downhole	Surface		Total	Downhole	Surface		Total	Downhole	Surface
Zn	34,868	27,696	7172	S	21,756	17,757	3999	Ce*	283	255	28
Fe	13,592	12,459	1133	Si*	13,636	8273	5363	Nd*	124	94	30
Cu	5796	3648	2148	Ca	3309	2574	735	La*	112	84	28
Pb	450	4	446	Al	1819	1342	477	Dy*	74	65	9
Cd	317	241	76	Mg*	1742	1680	62	Yb*	56	32	24
Mn*	150	119	31	Na	602	532	70	Gd*	52	46	6
Ag	81	15	66	K	131	94	37	Sm*	45	36	9
Se	47	37	10	Ti	103	99	4	Er*	44	39	5
Co*	32	30	2	B	5	4	1	Pr*	38	33	5
Cr*	18	16	2	Sr*	3.4	3	0.4	Cs*	31	21	10
V*	10	8	1	P*	2	–	2	Eu*	27	21	6
Au	9	6	4	Hf*	1.5	1.2	0.3	Ho*	24	24	–
Ni	8	7	1	Ba	1.5	1.1	0.4	Tb*	17	15	2
As*	7	1	6	Sc*	0.6	0.5	0.1	Lu*	15	12	3
Te*	4.9	4.5	0.4	Ta*	0.41	0.40	0.01	Tm*	10	10	–
Mo*	4.1	3.8	0.3	Nb*	0.4	0.3	0.1				
W*	1.4	1.3	0.1	Rb*	0.4	0.3	0.1				
Ga*	1.0	0.9	0.1	Y*	0.31	0.30	0.01				
Sn*	0.7	0.5	0.2	Li*	0.2	–	0.2				
Sb*	0.5	0.1	0.4	Be*	0.2	–	0.2				
Bi*	0.4	0.2	0.2	Zr*	0.2	–	0.2				
Ge*	0.2	–	0.2								
Hg	0.2	–	0.2								
Tl	0.03	0.02	0.01								
U*	0.03	0.02	0.01								
Th	0.01	–	0.01								
In*	0.01	–	0.01								

Calculated total mass accumulations over the lifetime of Reykjanes production well RN-10 for all major and trace elements in this study. Data are in tonnes for a) metals and b) other elements. Data for the REEs are in kilograms. Calculations are based on an estimated mass sulfide accumulation rate of ~5.7 t/yr sulfide (see text Section 5.4) extrapolated to 20,000 years, and average bulk geochemical data. Calculation methods are outlined in Supp. Info. A1. Mass accumulations are separated into downhole (below surface wellhead) and surface pipes as Hardardóttir (2011) previously estimated mass accumulation rates for surface pipes. Estimations of downhole mass sulfide accumulation are from this study (text Section 5.4). Data are separated into three sections to distinguish a) primary metals of interest, b) other elements, and c) REEs. Elements denoted with a * are considered as 'critical' or 'strategic' by the European Commission and/or the U.S. Geological Survey (EU Commission, 2017; USDoE, 2018). '–' indicates either no data are available, or data are below detection limits.

geothermal system is comparable to other large, high-temperature basalt-hosted seafloor hydrothermal systems elsewhere on the Mid-Atlantic Ridge. Estimates of the total metal accumulations over the 20,000 year lifetime of the Reykjanes system indicate significant enrichment of Zn, Pb, Au, and Ag relative to metal contents of both modern and ancient mafic-dominated seafloor massive sulfide deposits.

Acknowledgements

This project was funded by the Cluster of Excellence "The Future Ocean" within the framework of the Excellence Initiative by the Deutsche Forschungsgemeinschaft (DFG) on behalf of the German Federal and State governments. This research was also supported by a grant from the Society of Economic Geologists (Hugh E. McKinstry Fund) and an Inge-Lehmann-Fonds award (GEOMAR) both to H.L.J.G. HS Orka are thanked for permission to work on the scale samples. We thank numerous GEOMAR staff for assistance during this study: S. Lange, A. Jegen, and M. Sims for assistance with sample preparation and image processing, M. Thoener for microprobe assistance, and J. Heinze for XRD analyses. Declarations of interest: none.

Appendix A. Supplementary data

Supplementary data to this article can be found online at https://doi.org/10.1016/j.oregeorev.2019.103145.

References

Adamies, N., 2010. Mafic-dominated volcanogenic massive sulfide deposits in the Troodos Ophiolite, Cyprus Part 2-A review of genetic models and guides for exploration. Appl. Earth Sci. Trans. Inst. Min. Metall. Sect. B 119, 193–204.

Alt, J.C., Honnorez, J.J., Laverne, C., Emmermann, R., 1986. Hydrothermal alteration of a 1 km section through the upper oceanic crust, Deep Sea Drilling Project Hole 504B: mineralogy, chemistry and evolution of seawater-basalt interactions. J. Geophys. Res. 91 (B10), 10309–10335.

Alt, J.C., 1995. Subseafloor processes in mid-ocean ridge hydrothermal systems. In: Humphris, S.E., Zierenberg, R.A., Mullineaux, L.S., Thompson, R.E. (Eds.), Seafloor Hydrothermal Systems: Physical, Chemical, Biological, and Geological Interactions, pp. 85–114 Geophysical Monograph Series 91.

Alt, J.C., Laverne, C., Coggon, R.M., Teagle, D.A.H., Banerjee, N.R., Morgan, S., Smith-Duque, C.E., Harris, M., Galli, L., 2010. Subsurface structure of a submarine hydrothermal system in ocean crust formed at the East Pacific Rise, ODP/IODP Site 1256. Geochem. Geophys. Geosyst. 11. https://doi.org/10.1029/2010GC003144.

Arnorsson, S., 1978. Major element chemistry of the geothermal sea-water at Reykjanes and Svartsengi, Iceland. Mineral. Mag. 42, 209–220.

Arnorsson, S., Stefansson, A., Bjarnason, J.Ö., 2007. Fluid-flow interactions in geothermal systems. Rev. Mineral. Geochem. 65, 259–312.

Auclair, G., Fouquet, Y., 1987. Distribution of selenium in high-temperature hydrothermal sulfide deposits at 13°N, East Pacific Rise. Can. Mineral. 25, 577–587.

Barker, A.K., Coogan, L.A., Gillis, K.M., Hayman, N.W., Weis, D., 2010. Direct observation of a fossil high-temperature, fault-hosted, hydrothermal upflow zone in crust formed at the East Pacific Rise. Geology 38, 379–382.

Bazarkina, E.F., Pokrovski, G.S., Zotov, A.V., Hazemann, J.-L., 2010. Structure and stability of cadmium chloride complexes in hydrothermal fluids. Chem. Geol. 276, 1–17.

Bourcier, W.L., Barnes, H.L., 1987. Ore Solution Chemistry - VII. Stabilities of Chloride and Bisulfide Complexes of Zinc to 350°C. Econ. Geol. 82, 1839–1863.

Butler, I.B., Nesbitt, R.W., 1999. Trace element distributions in the chalcopyrite wall of a black smoker chimney; insights from laser ablation inductively-coupled plasma mass spectrometry (LA-ICP-MS). Earth Planet. Sci. Lett. 167, 335–345.

Butterfield, D.A., McDuff, R.E., Mottl, M.J., Lilley, M.D., Lupton, J.E., Massoth, G.J., 1994. Gradients in the composition of hydrothermal fluids from the Endeavour segment vent field: Phase separation and brine loss. J. Geophys. Res. 99 (B5), 9561–9583.

Coogan, L.A., Manning, C.E., Wilson, R.N., 2007. Oxygen isotope evidence for short-lived high-temperature pervasive fluid flow in the lower oceanic crust at fast-spreading ridges. Earth Planet. Sci. Lett. 260, 524–536.

Craig, J.R., Scott, S.D., 1976. Sulfide phase equilibria. In: Ribbe, P.H. (Ed.), Sulfide Mineralogy, pp. CS1–CS110 Reviews in Mineralogy, Mineralogical Society of America 1.
Douville, E., Bienvenu, P., Charlou, J.-L., Donval, J.P., Fouquet, Y., Appriou, P., Gamo, T., 1999. Yttrium and rare earth elements in fluids from various deep-sea hydrothermal systems. Geochim. Cosmochim. Acta 63, 627–643.
Drummond, S.F., Ohmoto, H., 1985. Chemical evolution and mineral deposition in boiling hydrothermal solutions. Econ. Geol. 80, 126–147.
Edmond, J.M., Campbell, A.C., Palmer, M.R., Klinkhammer, G.P., German, C.R., Edmonds, H.N., Elderfield, H., Thompson, G., Rona, P., 1995. Time series studies of vent fluids from the TAG and MARK sites (1986, 1990) Mid-Atlantic Ridge: a new solution chemistry model and a mechanism for Cu/Zn zonation in massive sulphide ore bodies. In: Parson, L.M., Walker, C.L., Dixon, D.R. (Eds.), Hydrothermal vents and processes, pp. 77–86 Geological Society of London Special Publication.
Edmonds, H.N., German, C.R., Green, D.R.H., Huh, Y., Gamo, T., Edmond, J.M., 1996. Continuation of the hydrothermal fluid chemistry time series at TAG, and the effects of ODP drilling. Geophys. Res. Lett. 23, 3487–3489.
European Commission, 2017. Study on the review of the list of Critical Raw Materials. Available from: http://ec.europa.eu. [Accessed September 2017].
Evans, G.N., Tivey, M.K., Seewald, J.S., Wheat, C.G., 2017. Influences of the Tonga subduction zone on seafloor massive sulfide deposits along the Eastern Lau spreading center and Valu Fa Ridge. Geochim. Cosmochim. Acta 215, 214–246.
Fournier, R.O., 1985. The behavior of silica in hydrothermal solutions. Reviews in Economic Geology 2, 45–60.
Fowler, A.P.G., Zierenberg, R.A., Reed, M.H., Palandri, J., Oskarsson, F., Gunnarsson, I., 2019. Rare earth element systematics in boiled fluids from basalt-hosted geothermal systems. Geochim. Cosmochim. Acta 244, 129–154.
Fowler, A.P.G., Zierenberg, R.A., 2016. Geochemical bias in drill cutting samples versus drill core samples returned from the Reykjanes Geothermal System, Iceland. Geothermics 62, 48–60.
Fowler, A.P.G., Zierenberg, R.A., Schiffman, P., Marks, N., Fridleifsson, G.O., 2015. Evolution of fluid–rock interaction in the Reykjanes geothermal system, Iceland: Evidence from Iceland Deep Drilling Project core RN-17B. J. Volcanol. Geoth. Res. 302, 47–63.
Francheteau, J., Armijo, R., Cheminee, J.L., Hekinian, R., Lonsdale, P., Blum, N., 1990. 1 Ma East Pacific Rise oceanic crust and uppermost mantle exposed by rifting in Hess Deep (equatorial Pacific Ocean). Earth Planet. Sci. Lett. 101, 281–295.
Franzson, H., Thordarson, Bjornsson, G., Gudlaugsson, S.T., Richter, B., Fridleifsson, G.O., Thorhallsson, S., 2002. Reykjanes high-temperature field, SW-Iceland. Geology and hydrothermal alteration of well RN-10. In: Twenty-Seventh Workshop on Geothermal Reservoir Engineering. Stanford University, Stanford, California, pp. 1–9.
Fridleifsson, G.O., Albertsson, A., Elders, W.A., Sigurdsson, O., Karlsdottir, R., Palsson, B., 2011. The Iceland Deep Drilling Project (IDDP): Planning for the Second Deep Well at Reykjanes. GRC Transactions 35, 347–354.
Fridleifsson, G.O., Elders, W.A., Zierenberg, R.A., Stefansson, A., Fowler, A.P.G., Weisenberger, T.B., Hardarson, B.S., Mesfin, K.G., 2017. The Iceland Deep Drilling Project 4.5 km deep well, IDDP-2, in the seawater-recharged Reykjanes geothermal field has successfully reached its supercritical target. Sci. Drill. 23, 1–12.
Fridriksson, Th., Oskarsson, F., Eyjolfsdottir, E., Sigurdsson, O., 2015. Fluid chemistry scenarios anticipated for IDDP-2 to be drilled in Reykjanes, Iceland. In: Proceedings World Geothermal Congress. Melbourne, Australia, pp. 1–9.
Fuchs, S., Hannington, M.D., Petersen, S., 2019. Divining gold in seafloor polymetallic massive sulfide systems. Miner. Deposita 54, 789–820.
Gallant, R.M., von Damm, K.L., 2006. Geochemical controls on hydrothermal fluids from the Kairei and Edmond Vent Fields, 23°-25°S, Central Indian Ridge. Geochem. Geophys. Geosyst. 7. https://doi.org/10.1029/2005GC001067.
Gamo, T., Chiba, H., Masuda, H., Edmonds, H.N., Fujioka, K., Kodama, Y., Nanba, H., Sano, Y., 1996. Chemical characteristics of hydrothermal fluids from the TAG mound of the mid-Atlantic Ridge in August 1994: implications for spatial and temporal variability of hydrothermal activity. Geophys. Res. Lett. 23, 3483–3486.
Gartman, A., Hannington, M.D., Jamieson, J.W., Peterkin, B., Garbe-Schoenberg, D., Findlay, A.J., Fuchs, S., Kwasnitschka, T., 2018. Boiling-induced formation of colloidal gold in black smoker fluids. Geology 46, 39–42.
Gillis, K.M., Thompson, G., 1993. Metabasalts from the Mid-Atlantic Ridge: new insights into hydrothermal systems in slow-spreading crust. Contrib. Miner. Petrol. 113, 502–523.
Gillis, K.M., Muehlenbachs, K., Stewart, M., Karson, J., Gleeson, T., 2001. Fluid flow patterns in fast-spreading East Pacific Rise crust exposed at Hess Deep. J. Geophys. Res. 106, 26311–26329.
Grant, H.L.J., Hannington, M.D., Petersen, S., Frische, M., Fuchs, S.H., 2018. Constraints on the behavior of trace elements in the actively-forming TAG deposit, Mid-Atlantic Ridge, based on LA-ICP-MS analyses of pyrite. Chem. Geol. 498, 45–71.
Grant, H.L.J., Layton-Matthews, D., Peter, J.M., 2015. Distribution and controls on silver mineralization in the Hackett River Main Zone, Nunavut, Canada: An Ag- and Pb-enriched Archean volcanogenic massive sulfide deposit. Econ. Geol. 110, 943–982.
Grguric, B.A., Putnis, A., 1999. Rapid exsolution behavior in the bornite-digenite series and implications for natural ore assemblages. Mineral. Mag. 63, 1–12.
Grguric, B.A., Harrison, R.J., Putnis, A., 2000. A revised phase diagram for the bornite-digenite join from in situ neutron diffraction and DSC experiments. Mineral. Mag. 64, 213–231.
Hannington, M.D., Galley, A.G., Herzig, P.M., Petersen, S., 1998. Comparison of the TAG Mound and Stockwork Complex with Cyprus-Type Massive Sulfide Deposits. In: Herzig, P.M., Humphris, S.E., Zierenberg, R.A. (Eds.), Proc. ODP Sci. Results, 158, pp. 389–415 College Station, TX (Ocean Drilling Program).
Hannington, M.D., Bleeker, W., Kjarsgaard, I., 1999. Sulfide mineralogy, geochemistry, and ore genesis of the Kidd Creek Deposit: Part II. The Bornite Zone. *Economic Geology Monograph* 10, 225–266.
Hannington, M.D., de Ronde, C.E.J., Petersen, S., 2005. Sea-floor tectonics and submarine hydrothermal systems. Econ. Geol. 100, 111–141.
Hannington, M.D., 2014. Volcanogenic Massive Sulfide Deposits. In: Scott, S.D. (Ed.), Treatise on Geochemistry, second ed. Elsevier, pp. 463–488 13.
Hannington, M.D., Hardardóttir, V., Garbe-Schönberg, D., Brown, K.L., 2016. Gold enrichment in active geothermal systems by accumulating colloidal suspensions. Nat. Geosci. 9, 299–302.
Hardardóttir, V., Brown, K., Fridriksson, T., Hedenquist, J.W., Hannington, M.D., Thorhallsson, S., 2009. Metals in deep liquid of the Reykjanes geothermal system, southwest Iceland: Implications for the composition of seafloor black smoker fluids. Geology 37, 1103–1106.
Hardardóttir, V., Hannington, M.D., Hedenquist, J.W., Kjarsgaard, I.M., 2010. Cu-Rich Scales in the Reykjanes Geothermal System, Iceland. Econ. Geol. 105, 1143–1155.
Hardardóttir, V., 2011. Metal-rich Scales in the Reykjanes Geothermal System, SW Iceland: Sulfide Minerals in a Seawater-dominated Hydrothermal Environment. University of Ottawa, Ottawa, Canada, pp. 288.
Hardardóttir, V., Hannington, M., Hedenquist, J., 2013. Metal concentrations and metal deposition in deep geothermal wells at the Reykjanes high-temperature area, Iceland. Procedia Earth Planet. Sci. 7, 338–341.
Hardardóttir, V., 2014. Sulfide scaling, well by well review. ISOR report 13-0365 prepared for HS Orka, November 2014.
Heft, K.L., Gillis, K.M., Pollock, M.A., Karson, J.A., Klein, E.M., 2008. Role of upwelling hydrothermal fluids in the development of alteration patterns at fast spreading ridges: Evidence from the sheeted dike complex at Pito Deep. Geochem. Geophys. Geosyst. 9. https://doi.org/10.1029/2007GC001926.
Heinrich, C.A., 1990. The chemistry of hydrothermal tin (-tungsten) ore deposition. Econ. Geol. 85, 457–481.
Heinrich, C.A., Gunther, D., Audetat, A., Ulrich, T., Frischknecht, R., 1999. Metal fractionation between magmatic brine and vapor, determined by microanalysis of fluid inclusions. Geology 27, 755–758.
Herzig, P.M., Becker, K.P., Stoffer, P., Baecker, H., Blum, N., 1988. Hydrothermal silica chimney fields in the Galapagos Spreading Center at 86°W. Earth Planet. Sci. Lett. 89, 261–272.
Huston, D.L., Sie, S.-H., Suter, G.F., Cooke, D.R., 1995. Trace Elements in Sulfide Minerals from Eastern Australian Volcanic-Hosted Massive Sulfide Deposits: Part I. Proton Microprobe Analyses of Pyrite, Chalcopyrite, and Sphalerite, and Part II. Selenium Levels in Pyrite: Comparison with $\delta^{34}S$ Values and Implications for the Source of Sulfur in Volcanogenic Hydrothermal Systems. Econ. Geol. 90, 1167–1196.
Jakobsson, S.P., Jonsson, J., Shido, F., 1978. Petrology of the Western Reykjanes Peninsula, Iceland. J. Petrol. 19, 669–705.
James, R.H., Green, D.R.H., Stock, M.J., Alker, B.J., Banerjee, N.R., Cole, C., German, C.R., Huvenne, V.A.I., Powell, A.M., Connelly, D.P., 2014. Composition of hydrothermal fluids and mineralogy of associated chimney material on the East Scotia Ridgeback-arc spreading centre. Geochim. Cosmochim. Acta 139, 47–71.
Jamieson, J.W., Clague, D.A., Hannington, M.D., 2014. Hydrothermal sulfide accumulation along the Endeavour Segment, Juan de Fuca Ridge. Earth Planet. Sci. Lett. 395, 136–148.
Johnson, J.W., Oelkers, E.H., Helgeson, H.C., 1992. SUPCRT92: A software package for calculating the standard molar thermodynamic properties of minerals, gases, aqueous species, and reactions from 1 to 5000 bar and 0 to 1000°C. Computers and Geoscience 18, 899–947.
Jowitt, S.M., Jenkin, G.W.T., Coogan, L.A., Naden, J., 2012. Quantifying the release of base metals from source rocks from volcanogenic massive sulfide deposits: Effect of protolith composition and alteration mineralogy. J. Geochem. Explor. 118, 47–59.
Kadko, D., Butterfield, D., 1998. The relationship of hydrothermal vent composition and crustal residence time to maturity of vent fields on the Juan de Fuca Ridge. Geochim. Cosmochim. Acta 62, 1521–1533.
Kadko, D., Gronvold, K., Butterfield, D., 2007. Application of radium isotopes to determine crustal residence times of hydrothermal fluids from two sites on the Reykjanes Peninsula, Iceland. Geochim. Cosmochim. Acta 71, 6019–6029.
Koschinsky, A., Garbe-Schoenberg, D., Sander, S., Schmidt, K., Gennerich, H.-H., Strauss, H., 2008. Hydrothermal venting at pressure-temperature conditions above the critical point of seawater, 5°S on the Mid-Atlantic Ridge. Geology 36, 615–618.
Kristall, B., Nielsen, D., Hannington, M.D., Kelley, D.S., Delaney, J.R., 2011. Chemical microenvironments within sulfide structures from the Mothra Hydrothermal Field: Evidence from high-resolution zoning of trace elements. Chem. Geol. 290, 12–30.
Lalou, C., Reyss, J.-L., Brichet, E., Rona, P.A., Thompson, G., 1995. Hydrothermal activity on a 10^5-year scale at a slow-spreading ridge, TAG hydrothermal field, Mid-Atlantic Ridge 26°N. J. Geophys. Res. Solid Earth 100, 17855–17862.
Li, Y.-H.H., 1991. Distribution patterns of elements in the oceans: A synthesis. Geochim. Cosmochim. Acta 55, 3223–3240.
Libbey, R.B., Williams-Jones, A.E., 2016a. Compositions of hydrothermal silicates and carbonates as indicators of physiochemical conditions in the Reykjanes geothermal system, Iceland. Geothermics 64, 15–27.
Libbey, R.B., Williams-Jones, A.E., 2016b. Relating sulfide mineral zonation and trace element chemistry to sub-surface processes in the Reykjanes geothermal system, Iceland. J. Volcanol. Geoth. Res. 310, 225–241.
Libbey, R.B., Williams-Jones, A.E., 2016c. Lithogeochemical approaches in geothermal system characterization: An application to the Reykjanes geothermal field, Iceland. Geothermics 64, 61–80.
Liu, W., Borg, S.J., Testemale, D., Etschmann, B., Hazemann, J.-L., Brugger, J., 2011. Speciation and thermodynamic properties for cobalt chloride complexes in hydrothermal fluids at 35–440°C and 600 bar: An in-situ XAS study. Geochimica Cosmochimica Acta 75, 1227–1248.
Liu, W., Migdisov, A., Williams-Jones, A.E., 2012. The stability of aqueous nickel(II)

chloride complexes in hydrothermal solutions: Results of UV-visible spectroscopic experiments. Geochim. Cosmochim. Acta 94, 276–290.
Macleod, C.J., Celerier, B., Frueh-Green, G.L., Manning, C.E., 1996. Tectonics of Hess Deep: A synthesis of drilling results from Leg 147. In: Mevel, C., Gillis, K.M., Allan, J.F., Meyer, P.S. (Eds.), Proc. ODP Sci. Results, 147, pp. 461–475 College Station, TX (Ocean Drilling Program).
Marks, N., Schiffman, P., Zierenberg, R.A., Franzson, H., Fridleifsson, G.O., 2010. Hydrothermal alteration in the Reykjanes geothermal system: Insights from Iceland deep drilling program well RN-17. J. Volcanol. Geoth. Res. 189, 172–190.
Marks, N., Zierenberg, R.A., Schiffman, P., 2015. Strontium and oxygen isotopic profiles through 3 km of hydrothermally altered oceanic crust in the Reykjanes Geothermal System, Iceland. Chem. Geol. 412, 34–47.
Maslennikov, V.V., Maslennikova, S.P., Large, R.R., Danyushevsky, L., Herrington, R.J., Ayupova, N.R., Zaykov, V.V., Lein, A.Yu., Tseluyko, A.S., Melekestseva, I.Yu., Tessalina, S.G., 2017. Chimneys in Paleozoic massive sulfide mounds of the Urals VMS deposits: Mineral and trace element comparison with modern black, grey, white, and clear smokers. Ore Geol. Rev. 85, 64–106.
McKibbon, M.A., Williams, A.E., Hall, G.E.M., 1990. Solubility and transport of platinum-group elements and Au in saline hydrothermal fluids: constraints from geothermal brine data. Econ. Geol. 85, 1926–1934.
Metz, S., Trefry, J.H., 2000. Chemical and mineralogical influences on concentrations of trace metals in hydrothermal fluids. Geochim. Cosmochim. Acta 64, 2267–2279.
Migdisov, A.A., Zezin, D., Williams-Jones, A.E., 2011. An experimental study of cobalt (II) complexation in Cl^- and H_2S-bearing hydrothermal solutions. Geochimica Cosmochimica Acta 75, 4065–4079.
Minubayeva, Z., Seward, T.M., 2010. Molybdic acid ionization under hydrothermal conditions to 300°C. Geochim. Cosmochim. Acta 74, 4365–4374.
Monecke, T., Petersen, S., Hannington, M.D., Grant, H.L.J., Samson, I., 2016. The minor element endowment of modern sea-floor massive sulfides and comparison with deposits hosted in ancient volcanic successions. Reviews in Economic Geology 18, 245–306.
Monecke, T., Petersen, S., Hannington, M.D., 2014. Constraints on water depth of massive sulfide formation: Evidence from modern seafloor hydrothermal systems. Econ. Geol. 109, 2079–2101.
Mottl, M.J., 1983. Metabasalts, axial hot springs, and the structure of hydrothermal systems at mid-ocean ridges. GSA Bulletin 94, 161–180.
Mottl, M.J., Seewald, J.S., Wheat, C.G., Tivey, M.K., Michael, P.J., Proskurowski, G., McCollom, T.M., Reeves, E., Sharkey, J., You, C.-F., Chan, L.-H., Pichler, T., 2011. Chemistry of hot springs along the Eastern Lau spreading center. Geochim. Cosmochim. Acta 75, 1013–1038.
Oskarsson, F., Fridriksson, T., Thorbjornsson, D., 2015. Geochemical Monitoring of the Reykjanes Geothermal Reservoir 2003 to 2013. In: Proceedings World Geothermal Congress. Melbourne, Australia, pp. 1–9.
Oudin, E., Constantinou, G., 1984. Black smoker chimney fragments in Cyprus sulphide deposits. Nature 308, 349–353.
Parmentier, E.M., Spooner, E.T.C., 1978. A theoretical study of hydrothermal convection and the origin of the ophiolitic sulphide ores of Cyprus. Earth Planet. Sci. Lett. 40, 33–44.
Patten, C.G.C., Pitcairn, I.K., Teagle, D.A.H., Harris, M., 2016. Mobility of Au and related elements during the hydrothermal alteration of the oceanic crust: implications for the sources of metals in VMS deposits. Miner. Deposita 51, 179–200.
Patten, C.G.C., Pitcairn, I.K., Teagle, D.A.H., 2017. Hydrothermal mobilisation of Au and other metals in supra-subduction oceanic crust: Insights from the Troodos ophiolite. Ore Geol. Rev. 86, 487–508.
Peate, D.W., Baker, J.A., Jakobsson, S.P., Waight, T.E., Kent, A.J.R., Grassineau, N.V., Skovgaard, A.C., 2009. Historic magmatism on the Reykjanes Peninsula, Iceland: a snap-shot of melt generation at a ridge segment. Contrib. Miner. Petrol. 157, 359–382.
Petersen, S., Herzig, P.M., Hannington, M.D., 1998. Fluid inclusion studies as a guide to the temperature regime within the TAG hydrothermal mound, 26°N, Mid-Atlantic Ridge. In: Herzig, P.M., Humphris, S.E., Zierenberg, R.A. (Eds.), Proc. ODP Sci. Results, 158, pp. 163–178 College Station, TX (Ocean Drilling Program).
Petersen, S., Herzig, P.M., Hannington, M.D., 2000. Third dimension of a presently forming VMS deposit: TAG hydrothermal mound, Mid-Atlantic Ridge, 26°N. Miner. Deposita 35, 233–259.
Petersen, S., Kraetschell, A., Augustin, N., Jamieson, J.W., Hein, J.R., Hannington, M.D., 2016. News from the seabed – Geological characteristics and resource potential of deep-sea mineral resources. Marine Policy 70, 175–187.
Pokrovski, G.S., Borisova, A.Y., Roux, J., Hazemann, J.L., Petdang, A., Tella, M., Testemale, D., 2006. Antimony speciation in saline hydrothermal fluids: A combined X-ray absorption fine structure spectroscopy and solubility study. Geochimica at Cosmochimica Acta 70, 4196–4214.
Pope, E.C., Bird, D.K., Arnorsson, S., Fridriksson, T., Elders, W.A., Fridleifsson, G.O., 2009. Isotopic constraints on ice age fluids in active geothermal systems: Reykjanes, Iceland. Geochim. Cosmochim. Acta 73, 4468–4488.
Saemundsson, K., and Jóhannesson, H., 2004. Geothermal map of Iceland. Iceland GeoSurvey and National Energy Authority.
Schmidt, K., Koschinsky, A., Garbe-Schoenberg, D., de Carvalho, L.M., Seifert, R., 2007. Geochemistry of hydrothermal fluids from the ultramafic-hosted Logatchev hydrothermal field, 15oN on the Mid-Atlantic Ridge: Temporal and spatial investigation. Chem. Geol. 242, 1–21.
Scott, S.D., Barnes, H.L., 1971. Sphalerite geothermometry and geobarometry. Econ. Geol. 66, 653–669.
Seward, R.J., Reed, M.H., Grist, H.R., Fridriksson, T., Danielsen, P., Thorhallsson, S., Elders, W.A., Fridleifsson, G.O., 2011. The Iceland Deep Drilling Project (IDDP): Deep Fluid Sampling in Fractured Quartz, Reykjanes Geothermal System. Iceland, American Geophysical Union Annual Meeting, San Francisco, USA, pp. 1.
Seward, R.J., 2014. Geothermal fluid equilibrium modeling: Comparison of wellhead fluid samples to deep samples in the Reykjanes system, Iceland (M.Sc. Thesis). University of Oregon, Eugene, Oregon, USA, pp. 69.
Seward, T.M., Williams-Jones, A.E., Migdisov, A.A., 2014. The chemistry of metal transport and deposition by ore-forming hydrothermal fluids. In: Scott, S.D. (Ed.), Treatise on Geochemistry, second ed. Elsevier, pp. 29–57 13.
Sigurdsson, O., 2010. The Reykjanes Seawater Geothermal System. Its Exploitation Under Regulatory Constrains. In: Proceedings World Geothermal Congress, pp. 1–7.
Sigurdsson, O., 2012. Reykjanes well history. HS Orka HF short report, 27 July 2012.
Simmons, S.F., Brown, K.L., Tutolo, B.M., 2016. Hydrothermal Transport of Ag, Au, Cu, Pb, Te, Zn, and Other Metals and Metalloids in New Zealand Geothermal Systems: Spatial Patterns, Fluid-Mineral Equilibria, and Implications for Epithermal Mineralization. Econ. Geol. 111, 589–618.
Springsklee, C., 2016. Schwefelisotope und Mineralzusammensetzung sulfidischer Präzipitate des Reykjanes Geothermalfeldes (B.Sc. Thesis). Westfälischen Wilhelms-Universität, Munster, Germany, pp. 121.
Stefansson, A., Seward, T.M., 2003. Experimental determination of the stability and stoichiometry of sulphide complexes of silver(I) in hydrothermal solutions to 400°C. Geochim. Cosmochim. Acta 67, 1395–1413.
Sternbergh, S., 2016. Reykjanes Grey Lagoon: Precipitate chemistry and implications for metal rich scale precipitation, submarine hydrothermal vents, and environmental impact. Thesis, Reykjavik University, Reykjavik, Iceland, M.Sc, pp. 63.
Suleimenov, O.M., Seward, T.M., 2000. Spectrophotometic measurements of metal complex formation at high temperatures: the stability of Mn(II) chloride species. Chem. Geol. 167, 177–192.
Susak, N.J., Crerar, D.A., 1985. Spectra and coordination changes of transition metals in hydrothermal solutions: Implications for ore genesis. Geochim. Cosmochim. Acta 49, 555–564.
Sveinbjornsdottir, A.E., Coleman, M.L., Yardley, B.W.D., 1986. Origin and history of hydrothermal fluids of the Reykjanes and Krafla geothermal fields, Iceland. Contrib. Miner. Petrol. 94, 99–109.
Testemale, D., Brugger, J., Liu, W., Etschmann, B., Hazemann, J.-L., 2009. In-situ X-ray absorption study of Iron(II) speciation in brines up to supercritical conditions. Chem. Geol. 264, 295–310.
Tivey, M.K., Humphris, S.E., Thompson, G., Hannington, M.D., Rona, P.A., 1995. Deducing patterns of fluid flow and mixing within the TAG active hydrothermal mound using mineralogical and geochemical data. J. Geophys. Res. 100 (B7), 12527–12555.
Tivey, M.K., Stakes, D.S., Cook, T.L., Hannington, M.D., Petersen, S., 1999. A model for growth of steep-sided vent structures on the Endeavour Segment of the Juan de Fuca Ridge: Results of a petrologic and geochemical study. J. Geophys. Res. Solid Earth 104, 22859–22883.
Tooth, B., Etschmann, B., Pokrovski, G.S., Testemale, D., Hazemann, J.L., Grundler, P.V., Brugger, J., 2013. Bismuth speciation in hydrothermal fluids: An X-ray absorption spectroscopy and solubility study. Geochim. Cosmochim. Acta 101, 156–172.
USDoE, 2018. Critical Materials Strategy. United States Department of Energy, Washington. Available from: https://energy.gov. [Accessed September 2018].
Vaughan, D.J., Rosso, K.M., 2006. Chemical bonding in sulfide minerals. Rev. Mineral. Geochem. 61, 231–264.
Von Damm, K.L., Edmond, J.M., Grant, B., Measures, C.I., Walden, B., Weiss, R.F., 1985a. Chemistry of submarine hydrothermal solutions at 21°N, East Pacific Rise. Geochim. Cosmochim. Acta 49, 2197–2220.
Von Damm, K.L., Edmond, J.M., Measures, C.I., Grant, B., 1985b. Chemistry of submarine hydrothermal solutions at Guaymas Basin, Gulf of California. Geochim. Cosmochim. Acta 49, 2221–2237.
Von Damm, K.L., 1990. Seafloor hydrothermal activity: black smoker chemistry and chimneys. Ann. Rev. Earth and Planet Sci. 18, 173–204.
Williams-Jones, A.E., Heinrich, C.A., 2005. Vapor Transport of Metals and the Formation of Magmatic-Hydrothermal-Ore. Econ. Geol. 100, 1287–1312.
Williams-Jones, A.E., Migdisov, A.A., 2014. Experimental constraints on the transport and deposition of metals in ore-forming hydrothermal systems. Economic Geology Special Publication 18, 77–95.
Wood, S.A., Samson, I.M., 2006. The aqueous geochemistry of gallium, germanium, indium and scandium. Ore Geol. Rev. 28, 57–102.
Zierenberg, R.A., Fouquet, Y., Miller, D.J., Bahr, J.M., Baker, P.A., Bjerkgard, T., Brunner, C.A., Duckworth, R.C., Gable, R., Gieskes, J.M., Goodfellow, W.D., Groeschel-Becker, H.M., Guerin, G., Ishibashi, J., Iturrino, L.L., Nehlig, P., Peter, J.M., Rigsby, C.A., Schultheiss, P., Shanks III, W.C., Simoneit, B.R.T., Summit, M., Teagle, D.A.H., Urbat, M., Zuffa, G.G., 1998. The deep structure of a sea-floor hydrothermal deposit. Nature 392, 485–488.